UC Santa Barbara

UC Santa Barbara Electronic Theses and Dissertations

Title

Excitation of Seismic Waves by the Atmosphere: Monitoring Severe Weather with Modern Digital Seismic Data

Permalink

https://escholarship.org/uc/item/0255g0kf

Author

Lamontagne, Anne

Publication Date

2018

Peer reviewed|Thesis/dissertation

UNIVERSITY OF CALIFORNIA

Santa Barbara

Excitation of Seismic Waves by the Atmosphere: Monitoring Severe Weather with Modern

Digital Seismic Data

A dissertation submitted in partial satisfaction of the requirements for the degree Doctor of Philosophy in Geological Sciences

by

Anne M. Lamontagne

Committee in charge:

Professor Toshiro Tanimoto, Chair

Professor Chen Ji

Professor Robin Matoza

September 2018

Chen Ji			
Robin Matoza			

The dissertation of Anne M. Lamontagne is approved.

September 2018

Excitation of Seismic Waves by the Atmosphere: Monitoring Severe Weather with Modern
Digital Seismic Data
Copyright © 2018
by
Anne M. Lamontagne

ACKNOWLEDGEMENTS

I want to start by thanking my advisor, Professor Toshiro Tanimoto for his support and guidance through my PhD. He gave me the chance to jump into the exciting and novel research that became my thesis and I'm extremely grateful for the opportunities it has provided me. He has taught me to think critically and independently and I would not have gotten here without his thoughtful guidance and pushing me to do my best. I would also like to thank my committee members, Professor Chen Ji and Professor Robin Matoza for their advice and insightful comments on my thesis.

Next, I was to thank my group members and collaborators, Aaron Anderson and Jiong Wang. The research was a little bit lonely until they arrived, and the ability to discuss projects, bounce ideas and receive coding advice has been invaluable.

Finally, I want to thank all my friends and family that have supported me throughout the years. My parents especially, who have always unconditionally supported my endeavors. Special thanks of course goes to Mareike Adams, the other half of the geophysics twins. My time here at graduate school with have been far harder without her friendship and I'm grateful to have shared an office with her for these years.

VITA OF ANNE M. LAMONTAGNE July 2018

EDUCATION

Doctor of Philosophy in Geological Sciences (expected)

July 2018

University of California, Santa Barbara Advisor: Professor Toshiro Tanimoto

Dissertation: "Excitation of Seismic Waves by the Atmosphere: Monitoring Severe Weather with Modern Digital Seismic Data"

Bachelor of Science, Physics

May 2013

University of New Hampshire, Durham, NH Advisor: Professor Lynn Kistler and Mark Popecki

PROFESSIONAL EMPLOYMENT

Graduate Student Researcher, Dept. of Earth Science, UCSB
Teaching Associate, Dept. of Earth Science, UCSB
Teaching Assistant, Dept. of Earth Science, UCSB
Undergraduate Researcher, Space Science Center, UNH

PUBLICATIONS

Lamontagne, A., Anderson, A and Tanimoto, T. (in prep) Backprojection of tropical cyclones in the Atlantic

Valovcin, A., & Tanimoto, T. (2017). Modeling the excitation of seismic waves by the Joplin tornado. *Geophysical Research Letters*, 44, 10,256-10,261.

Tanimoto, T., & Valovcin, A. (2016). Existence of the threshold pressure for seismic excitation by atmospheric disturbances. *Geophysical Research Letters*, 43(21).

Tanimoto, T., & **Valovcin**, **A**. (2015). Stochastic excitation of seismic waves by a hurricane. *Journal of Geophysical Research: Solid Earth*, 120(11), 7713-7728.

Tanimoto, T., & Lamontagne, A. (2014). Temporal and spatial evolution of an on-land hurricane observed by seismic data. Geophysical Research Letters, 41(21), 7532-7538.

AWARDS

- Seismological Society of America Student Presentation Award (2018)
- Archuleta Family Fellowship in Earth Science, UCSB (2018)
- Alumni Graduate Award for Research Excellence, UCSB (2016)
- Earth Research Institute Summer Fellowship, UCSB (2015)
- Departmental Geophysics Award, UCSB (2015)
- Imperial Barrel Award Participant (2014)
- Richard St. Onge Scholarship, UNH (2011)
- Presidential Scholarship, UNH (2009)

FIELDS OF STUDY

Major Field: Seismology

Studies in Environmental Seismology and Land-Atmosphere Interactions

ABSTRACT

Excitation of Seismic Waves by the Atmosphere: Monitoring Severe Weather with Modern

Digital Seismic Data

by

Anne M. Lamontagne

When sufficiently strong, hurricanes and tornadoes generate significant observable ground motions through pressure changes at the surface. Under the proper circumstances, these signals are recorded by seismometers and can provide insight into the storm events, which we examine in this thesis. First, we used two dense seismic arrays, Earthscope's Transportable Array (TA) and the Southern California Seismic Network (SCSN) to examine the case of landfallen hurricanes through the TA. Through the study of Hurricane Isaac, which made landfall through the TA in 2012, we can observe its decay as it weakened and dissipated over time in the seismic data within the frequency range of 0.01-0.02 Hz. With this data, we develop a stochastic theory for the generation of seismic waves by a hurricane.

In further examining the seismic and barometric signals generated by Hurricane Isaac and Tropical Storm Lee (2011), we also identify the existence of a threshold pressure. Above a certain level of atmospheric surface pressure, there is dependence in the seismic wave generation. While this and the theory of seismic wave generation are novel results,

these observations do not hold many practical applications towards hurricane monitoring, which we go into further detail in the final potion of this thesis.

In regards to tornadoes, we identified seismic signals corresponding to an EF5 tornado that occurred on May 22, 2011 in Joplin, Missouri. This signal was recorded by the TA station that was closest to the tornado track. We modeled this seismic signal at low frequencies (below 0.1 Hz) by assuming an equivalent vertical force and found that the amplitude of the seismic signal corresponds to the reported intensity of the storm. Further analysis of tornadoes in this way could provide a quantitative method of measuring tornado strength using seismic data.

Finally, using the SCSN, we performed a backprojection of 0.2 Hz P-waves of hurricanes over the ocean between 2011-2017, in order to test the possibility of tracking them using seismic data. We find that for many strong hurricanes, the backprojection results in a P-wave amplitude peak that can be associated with the storm. There is, however, a dependence on the size of the storm, as backprojection tracking performs best on the largest hurricanes that were examined in this study.

TABLE OF CONTENTS

1.	Introduction
	1.1. References
2.	Stochastic excitation of seismic waves by a hurricane
	2.1. Introduction
	2.2. Hurricane Isaac
	2.3. Amplitude-Distance Plots from Hurricane center
	2.3.1. Examples of seismic and barometric data
	2.3.2. Amplitude-distance plots
	2.3.3. Seismic PSD vs. Pressure PSD at same stations19
	2.3.4. Seismic and Pressure data from other cyclones20
	2.3.5. Averaging for seismic PSD and pressure PSD20
	2.3.6. Coherence in the atmospheric pressure field22
	2.4. Theory of Stochastic Excitation of Seismic Ground Motion23
	2.5. Solving for the correlation length
	2.6. The cubic model
	2.7. Discussion
	2.7.1. Alternative mechanisms
	2.7.2. Effects of pressure waves and strong winds on barometer data32
	2.8. Conclusion
	2.9. Appendix53
	2.10. References

3.	Existence of the Threshold Pressure for Seismic Excitation by Ati	mospheric
Disturban	ices	71
	3.1. Introduction	72
	3.2. Data and Approach	73
	3.3. Pressure PSD vs. Ground Velocity PSD	75
	3.4. Discussion and Summary	78
	3.5. Appendix	86
	3.6. References	86
4.	Modeling the excitation of seismic waves by the Joplin tornado	90
	4.1. Introduction	91
	4.2. The Joplin Tornado	92
	4.3. Methods	93
	4.4. Results	97
	4.5. Discussion	97
	4.6. References	104
5.	Backprojection of Tropical Cyclones in the Atlantic	107
	5.1. Introduction	108
	5.2. Data and Methods	109
	5.3. Results	111
	5.3.1. Backprojection of Tropical Cyclones	111
	5.3.2. Comparing Hurricane Size	113
	5.4. Discussion	
	5.5. Conclusions	

5.6.	Appendix	128
5.7.	References	182

1. Introduction

The application of seismic techniques to study processes on Earth's surface is a relatively new and growing field. Seismic instruments and arrays around the world are being used to study a wide range of phenomena, such as landslides, rivers, glaciers, wind and weather (e.g. Roth *et al.*, 2014; Mordret *et al.*, 2016; Lott *et al.*, 2017; Gualtieri *et al.*, 2018; Lai *et al.*, 2018). This growing field falls under the recently coined name of "Environmental Seismology" and much of the signals examine fall within the Earth's ambient seismic noise (Larose *et al.*, 2015). While the field is broad and there are many applications for new seismic methods, we will be focusing on one aspect in particular: the interaction between the atmosphere and the solid Earth and oceans.

The recent proliferation of environmental seismology has benefited greatly from an increase in seismic array networks around the world. Seismic data from networks like the Earthscope Transportable array (TA), whose initial purpose was to study Earth's structure, can provide unique data sets for studies outside of the original scope of the project (http://www.earthscope.org/science/observatories/usarray). The TA has been especially useful for the research presented here, for after 2010 barometers and infrasound sensors were added to the network, providing a unique data set of co-located seismic and barometric data. With the TA and another dense network, the Southern California Seismic Network, we present here the studies focusing on two types of severe weather events- hurricanes and tornadoes- and how they interact with Earth.

Hurricanes and tornadoes generate seismic waves in varying ways. For hurricanes, this excitation differs on land and over the ocean. On land, these storms create pressure changes at the surface which in turn excite seismic waves in the solid Earth (Figure 1.1). Over the ocean, hurricanes are generating seismic waves through ocean wave-wave interactions that occur on the ocean's surface. This process has been observed and described in previous studies (e.g. Ardhuin *et al.*, 2011). For tornadoes, it has been found that they excite seismic waves when they touch down. Some of the energy transferred into the ground when the storm touches down is converted into seismic energy, which then propagates outward from the storm (Figure 1.2). This process in described in detail in Tatom and Vitton (2001).

There are four chapters in this thesis relating to interactions between hurricanes and tornadoes and the solid Earth. The first chapter focuses on the seismic and barometric signals generated by Hurricane Isaac, a Category 1 hurricane that made landfall in Louisiana in 2012 and develops a stochastic excitation theory for the generation of seismic waves. The second chapter continues using Hurricane Isaac, as well as Tropical Storm Lee (2011) to identify the existence of a threshold pressure, above which there is a dependence on atmospheric pressure in the seismic data. The third chapter takes a different direction, and goes through the process of modeling the seismic waves generated by the Joplin tornado. The final chapter takes the study back to hurricanes, developing a backprojection method for tracking hurricanes over the ocean.

In Chapter 1, we examine how a hurricane (Hurricane Isaac, 2012) generated seismic ground motions, using a combination of seismic and barometric data from the TA. In the past, studies have used seismic data to examine the signals from hurricanes remotely (e.g. Orville and Gutenberg, 1946; Gilmore and Hubert, 1948; Gerstoft, Fehler and Sabra, 2006; Zhang, Gerstoft and Bromirski, 2010), however the signal generated when a hurricane makes landfall through a dense seismic array had not yet been observed. At low frequencies (0.01-0.02 Hz) we find that seismic and pressure PSD amplitudes show a decreasing trend with distance from the center of the hurricane, although the rates at which the two signals decrease are not the same. We connect these two data sets and develop a stochastic theory of seismic-wave excitation by surface pressure where the surface pressure is the excitation source and the seismic data are the resulting seismic-wave field. The results suggest that there is a centralized source for the seismic-wave excitation, which explains why the seismic data decreases with distance more quickly than the barometric data.

In Chapter 2, we continue our analysis of the seismic waves generated by a landfallen hurricane, further examining the relationship between the atmospheric pressure PSDs and the excited seismic ground velocity PSDs. In the same frequency range of 0.01-0.02 Hz, there exists a threshold pressure in the surface pressure PSD, above which the vertical seismic ground motion is affected by changes in surface pressure. Below this value, there are no changes in the seismic ground velocity as a result of pressure. We focus on the vertical ground motions, as the horizontal ground velocity PSDs are about two orders of magnitude larger than vertical PSDs and change with pressure for the entire range. We

attribute this to being related to ground tilt. To further understand the interactions between the atmosphere and the solid Earth, we most focus on ranges in surface pressure above this threshold value. The studies presented in chapters 1 and 2 demonstrate the possibility of using co-located seismic and barometric data to learn more about how the atmosphere couples to the solid Earth. Other methods, however, are required if we are to use seismic data to monitor or further study tropical cyclones. One of these methods will be described in Chapter 4.

Aside from hurricanes, tornadoes are among the most common natural disasters in the United States. In addition to being extremely damaging if they travel through a populated area, they are fairly difficult to study up close. In Chapter 3, we go through the process of using the seismic ground motions generated by a tornado (the Joplin tornado, 2011) to model the seismic source of the storm. This analysis is made possible by a colocated pair of a seismometer and barometer in the TA, which the tornado passed within 2km of when it was touched down. When tornadoes touch down, they transfer energy into the ground, and some of that energy is converted into seismic energy, which can be picked up on nearby seismometers (Tatom, Knupp and Vitton, 1995; Tatom and Vitton, 2001; Ingel, 2004).

By isolating the tornado-generated seismic signal and approximating it as a moving seismic source, we are able to model the vertical seismic data. The results show that the amplitude of the source changes over time. Tornadoes are currently rated on the Enhanced Fujita Scale, an intensity scale that estimates the winds speeds and rates the tornado based

on the amount of damage done during the storm (McDonald and Mehta, 2006). It is not, however, a quantitative measure for the tornado's size, without a way to directly measure the wind speeds or its energy, such a scale is not possible. In comparing the amplitude of the inverted source from our results to the reported EF intensity of the storm, we find that the source amplitude is largest when the tornado is reported to be strongest and smallest when the tornado is weakest. From this, there holds potential to develop a method of measuring tornado size using seismic data.

Finally, in chapter 4, we demonstrate a method of backprojection for the seismic signals generated by hurricanes over the ocean and discuss the size requirements of the storm for the method to be viable. The study of the origins of microseismic noise has a long history; the different peak frequencies can be attributed to two generation mechanisms: (1) the primary microseisms, with periods from 10-20s, which are produced by coupling between ocean waves and the solid Earth in shallow environments (Hasselmann, 1963; Ardhuin *et al.*, 2011; Gualtieri *et al.*, 2018) and (2) the secondary microseisms, with periods less than 10s, which are produced by wave-wave interactions that occur near the ocean surface (Longuet-Higgins, 1950; Hasselmann, 1963). Hurricanes are also thought to produce microseisms in the secondary frequency range while they are over the ocean (Zhang, Gerstoft and Bromirski, 2010; Ardhuin *et al.*, 2011; Farra *et al.*, 2016; Gualtieri *et al.*, 2018).

We examined 27 Atlantic hurricanes from 2011 to 2017. We perform a backprojection of 0.2 Hz P waves recorded at the Southern California Seismic Network for the durations of the hurricanes. For many of the hurricanes in this time span, the peak

amplitudes of the 0.2 Hz waves occur near the reported locations of the storms and track them through time, although the peak is off-set from the center of the hurricane. The off-set is likely a result of wave interaction between ocean waves and waves excited by the hurricane winds. The overall strength of the hurricane also contributes to whether or not a peak is observed, as the likelihood of resolving a backprojected peak that we are able to associate with the storm appears to be related to its wind speeds and overall area.

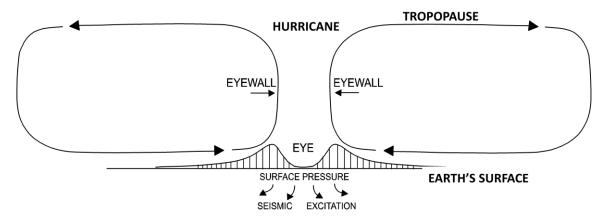


Figure 1.1: Diagram of seismic wave generation by a hurricane. As the winds of the hurricane travel horizontally across Earth's surface and turn vertically in the eyewall, there are atmospheric surface pressure fluctuations that occur. These changes in surface pressure couple to the solid Earth and excite seismic waves.

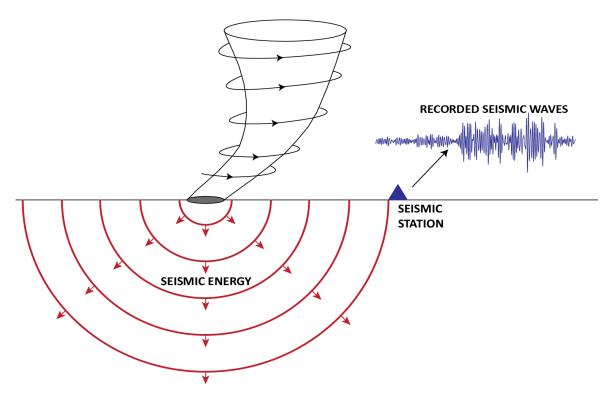


Figure 1.2: Seismic wave generation and propagation by a tornado. When a tornado touches down, it transmits energy into the ground, some of which is converted into seismic energy (Tatom and Vitton, 2001).

1.1. References

- Ardhuin, F. et al. (2011) 'Ocean wave sources of seismic noise', Journal of Geophysical Research. Wiley-Blackwell, 116(C9), p. C09004. doi: 10.1029/2011JC006952.
- es, 54(8), pp. 1014–1026. doi: 10.1175/1520-0469(1997)054<1014:SAOHIC>2.0.CO;2.
- Farra, V. *et al.* (2016) 'Ray-theoretical modeling of secondary microseism *P* waves', *Geophysical Journal International.* Oxford University Press, 206(3), pp. 1730–1739.

 doi: 10.1093/gji/ggw242.
- Gerstoft, P., Fehler, M. C. and Sabra, K. G. (2006) 'When Katrina hit California', Geophysical Research Letters, 33(17), pp. 2–7. doi: 10.1029/2006GL027270.
- Gilmore, M. and Hubert, W. (1948) 'Microseisms and Pacific Typhoons', *Bulletin of the Seismological Society of America*, 178(1940).
- Gualtieri, L. *et al.* (2018) 'The persistent signature of tropical cyclones in ambient seismic noise', *Earth and Planetary Science Letters*. Elsevier B.V., 484, pp. 287–294. doi: 10.1016/j.epsl.2017.12.026.
- Hasselmann, K. (1963) 'A statistical analysis of the generation of microseisms', *Rev. of Geophys.*, 1(2), pp. 177–210.
- Ingel, L. K. (2004) 'An Effective Mechanism of Seismic Signal Generation during the Interaction of Tornadoes with the Earth' s Surface', 395(2), pp. 292–295.
- Kobayashi, N. and Nishida, K. (1998) 'Continuous excitation of planetary free oscillations by atmospheric disturbances', *Nature*, 395(6700), pp. 357–360. doi: 10.1038/26427.
- Lai, V. H. et al. (2018) 'The Seismic Signature of Debris Flows: Flow Mechanics and Early

- Warning at Montecito, California', *Geophysical Research Letters*. Wiley-Blackwell. doi: 10.1029/2018GL077683.
- Larose, E. *et al.* (2015) 'Environmental seismology: What can we learn on earth surface processes with ambient noise?', *Journal of Applied Geophysics*. Elsevier, 116, pp. 62–74. doi: 10.1016/J.JAPPGEO.2015.02.001.
- Longuet-Higgins, M. S. (1950) 'A Theory of the Origin of Microseisms', *Philosophical Transactions of the Royal Society A: Mathematical, Physical and Engineering Sciences*, 243(857), pp. 1–35. doi: 10.1098/rsta.1950.0012.
- Lott, F. F. *et al.* (2017) 'On the Analysis of Wind-Induced Noise in Seismological Recordings', *Pure and Applied Geophysics*. Springer International Publishing, 174(3), pp. 1453–1470. doi: 10.1007/s00024-017-1477-2.
- McDonald, J. R. and Mehta, K. C. (2006) 'A Recommendation for an Enhanced Fujita Scale (EF-Scale)'. Wind Science and Engineering Center, Texas Tech University.
- Mordret, A. *et al.* (2016) 'Monitoring southwest Greenlands ice sheet melt with ambient seismic noise', *Science Advances*. American Association for the Advancement of Science, 2(5), pp. e1501538–e1501538. doi: 10.1126/sciadv.1501538.
- Orville, H. T. and Gutenberg, B. (1946) 'The use of microseisms in hurricane detection', *Eos, Transactions American Geophysical Union*, 27(1), pp. 111–117. doi: 10.1029/TR027i001p00111.
- Roth, D. L. *et al.* (2014) 'Migration of a coarse fluvial sediment pulse detected by hysteresis in bedload generated seismic waves', *Earth and Planetary Science Letters*.

- Tatom, F. B., Knupp, K. R. and Vitton, S. J. (1995) 'Tornado Detection Based on Seismic Signal', *Journal of Applied Meteorology*, 34.
- Tatom, F. and Vitton, S. (2001) 'The Transfer of Energy from a Tornado into the Ground', Seismological Research Letters, 72(1), pp. 12–21. Available at: http://171.66.125.217/content/72/1/12.short.
- Zhang, J., Gerstoft, P. and Bromirski, P. D. (2010) 'Pelagic and coastal sources of P-wave microseisms: Generation under tropical cyclones', *Geophysical Research Letters*, 37(15), pp. 1–6. doi: 10.1029/2010GL044288.

2. Stochastic excitation of seismic waves by a hurricane

Except for the addition of section 2.3.4, this chapter appeared essentially in this form in:

Tanimoto, T., and A. Valovcin (2015), Stochastic excitation of seismic waves by a hurricane, J. Geophys. Res. Solid Earth, 120, 7713–7728, doi:10.1002/2015JB012177.

2.1. Introduction

The idea of monitoring hurricanes (tropical cyclones) by seismic data has a long history (e.g. Gilmore and Hubert, 1948). The main purpose then was to detect hurricanes from the use of microseisms (Orville and Gutenberg, 1946) but such a seismic approach was soon replaced by satellite observations from space. With the appearance of broadband seismometers and their arrays in the last 20 years, the number of seismic studies on hurricanes has increased again. This was motivated by an interest that global warming and increased hurricane power may be related, and seismic data may have an answer (Bromirski and Kossin, 2008; Ebeling and Stein, 2011).

The aim of this study is to understand how an on-land hurricane excites seismic ground motions. Many recent seismic studies on hurricanes examined data while hurricanes were still in the ocean (e.g. Chi *et al.*, 2010; Zhang, Gerstoft and Bromirski, 2010; Lee *et al.*, 2012) which makes our study quite different from them. We take full advantage of the Earthscope network (www.earthscope.org), which consists of permanent stations, and the Transportable Array (TA hereafter), which has a dense distribution of barometers and seismometers. This network has recorded unique data for hurricanes in the last 5-6 years as some hurricanes passed directly through this network. This is an ideal situation to study onland hurricanes as barometer data provide information on the excitation source of seismic waves and seismic data provide the resultant seismic wave fields.

In this study, we focus on Hurricane Isaac in 2012. We conducted a preliminary study on it (Tanimoto and Lamontagne, 2014, hereafter TL14) using seismic data only. By inverting seismic data for surface pressure, TL14 led to a solution that indicated large pressure changes under the eyewall of the hurricane. Time evolution (decay) of this surface pressure solution suggested a particular manner that this eyewall system decayed. We discussed that this time evolution must be related to the changes in the ascending flow in the eyewall that deteriorated over a few days after the landfall (Riehl, 1950; Jorgensen, 1984; Jorgensen *et al.*, 1985; Emanuel, 1986, 1991, 1997, 2003).

In order to connect and understand seismic and barometric data, we develop a stochastic excitation theory which extends the normal-mode excitation theory (e.g. Gilbert, 1970; Dahlen and Tromp, 1998). Stochastic excitation theories based on the normal-mode approach were developed previously for various problems, such as for the Sun's oscillations (Goldreich and Keeley, 1977) and for long-period seismic noise, often referred to as the hum (Kobayashi and Nishida, 1998; Tanimoto, 1999, 2005, 2013; Tanimoto and Um, 1999; Fukao *et al.*, 2002; Webb, 2007, 2008; Gualtieri *et al.*, 2013). The approach in this paper is closest to Fukao *et al.* (2002). However, Fukao *et al.* (2002) worked on a global-scale problem while a hurricane problem is a regional one (horizontal scale ~1000km), which requires a different approximation at the last step.

Our main approach is to examine the amplitude-distance variations of seismic and pressure data from the hurricane center and monitor their time evolution where we discovered the amplitude decay rate with distance is faster for seismic data than for pressure

data. This study centers on this observation and attempts to answer this difference through data analysis. In particular, we propose a mechanism in which the correlation length in the pressure field becomes larger near the center of a hurricane; in general, a longer correlation length in the (random) pressure field increases the efficiency of seismic-wave excitation. Longer correlation length near the center essentially leads to a more centrally focused source than the original pressure field and can explain the differences in decay rates with distance.

In essence, we invoke higher spatial coherence in the surface-pressure field near the hurricane center to explain the observation. A centrally focused source may arise by different mechanisms, however; for example, due to strong turbulence near the center, transient bursts of pressure may occur. A higher temporal coherence may also result. Both mechanisms may lead to a similar centralized source. We briefly discuss such alternative mechanisms in the discussion, although detailed analyses of these mechanisms are beyond the scope of this paper.

We will describe the basic information on Hurricane Isaac in section 2, some key features in seismic and barometric data in section 3, and present our stochastic excitation theory in section 4. In section 5, we show our attempts to fit seismic and barometric data **to** this theory and how the correlation length in this stochastic excitation theory is estimated from data. In section 6, we present a scaling analysis from the derived solutions in section 5 and show the excitation source effectively becomes proportional to the third power of pressure near the center. We will briefly discuss the alternative mechanisms in section 7 and summarize our conclusions in section 8.

2.2. Hurricane Isaac

Figure 2.1 shows the track of Hurricane Isaac based on satellite data (Berg, 2013). This information is critical for our analysis as we use these locations for constructing the amplitude-distance plots for each time interval.

Hurricane Isaac in 2012 was a tropical storm for most of its life but it intensified to become a hurricane at about 12:00 UTC August 28, twelve hours before its first landfall at the mouth of the Mississippi river, and remained a hurricane until about 18:00 August 29. Its hurricane stage (category 1) is indicated by red circles in Figure 2.1. Its first landfall occurred at 00:00 UTC August 29. The eye crossed back over the nearby ocean but stayed very close to the coast. The second landfall occurred at 08:00 UTC August 29, just west of Port Fourchon, Louisiana. After the second landfall, it moved northward in an area dense with seismometers and barometers from the Earthscope project. Hereafter, when we refer to the landfall, we refer to the second landfall at 08:00 UTC on August 29.

2.3. Amplitude-Distance Plots from Hurricane center

2.3.1. Examples of seismic and barometric data

We pointed out in TL14 that one of the difficulties in studying the strength of a hurricane by seismic waves is that not all seismic waves come directly from the center of a hurricane. For some frequency bands, ocean waves which are excited by the same hurricane become secondary sources of seismic-wave excitation (Longuet-Higgins, 1950; Hasselmann, 1963). Evidence was shown in TL14 that this was indeed the case for seismic

waves for frequencies about 0.1-0.3 Hz (Figure 2.2). This is unfortunate because this band is the most energetic frequency band of seismic waves, but in order to study the processes near the hurricane center, we must focus on other frequency bands.

In TL14, we also showed that processes near the hurricane eye are the dominant source of low-frequency seismic waves of about 0.01-0.02 Hz. Figure 2.3 shows seismic and barometric data for Hurricane Isaac at 00:00 UTC on August 30. We computed the power spectral density (PSD) by using the formula $|F(\omega)|^2/T$ where $|F(\omega)|$ is the Fourier spectra of seismograms (ground velocity) and T is the length of time series. For this study, we used T=1 hour for all computation of PSDs.

In this paper, we only analyze vertical-component seismograms (as in TL14) and barograms. Horizontal-component seismograms have large amplitudes but also contain large scatter and we feel we are not at a stage to understand the behaviors of horizontal-component data. Vertical components show much more systematic amplitude variations with smaller scatter and we believe that an understanding between barometer data and vertical component seismograms is possible.

The left panels in Figure 2.3 show seismic amplitudes (PSD) on a map (top) and the amplitude-distance plot from the hurricane center (bottom). The hurricane center is shown by the red triangle in the top panel. The two right panels show similar plots for surface pressure. The concentric circles from the center are drawn at every 100 km (top) and the same color scales are used for the top and the bottom panels.

In both seismic and pressure data, we note that high-amplitude stations (red) tend to surround the hurricane center (top panels). This indicates that the exciting sources of these waves are near the center of this hurricane. They approximately show axisymmetric patterns, although some deviations may be recognized. Because of these observed features, we adopt an axisymmetric assumption in the theory and also in the data analysis.

In the two bottom panels, both spanning 0-1000 km from the center, show an important difference between seismic and pressure data. That is, the differences in the rates of amplitude decay with distance from the center. Seismic data merge with the background noise at about 500-600 km beyond which amplitudes flatten out (Figure 2.3, bottom-left). A black dashed line is shown in the figure in order to indicate the background noise level. Pressure data merge with the background noise at about 800-1000 km (Figure 2.3, bottom-right). The amplitude-distance decay rate is clearly higher for seismic data than that for barometric data. This is one of the most important features that we seek to explain by our analysis.

2.3.2. Amplitude-distance plots

In Figure 2.4 (a-h), we show how seismic amplitudes (PSD) in the frequency band 0.01-0.02 Hz varied with distance from the center of Hurricane Isaac. These plots are the snapshots of the amplitude-distance plots after the landfall. With respect to the second landfall (UTC 08:00 Aug. 29), they start from -2 hours (2 hours before landfall) to 40 hours after landfall plotted at 6 hour intervals from Figure 2.4a to Figure 2.4h.

In the first two panels (Figure 2.4a and 4b), the seismic amplitude peak is sharp and is located at a distance about 70-80 km from the center. A vertical dash line is given in each panel to indicate the distance of 75 km. At the 10th hour (Figure 2.4c), the peak value had decreased by a factor of two and the width of the peak became slightly broader but the peak location stayed at about the same distance from the hurricane center. At the 16th hour (Figure 2.4d) the peak still stayed close to 70-80 km but the width of the peak had clearly increased. At the 22nd hour (Figure 2.4e) and the 28th hour (Figure 2.4f) the widths of the peak became much wider with increased scatter in seismic amplitudes and at the same time the peak distance from the center increased. At the 34th hour (Figure 2.4g), a broad peak at a distance of about 300 km can be recognized but the scatter is now quite large. Scatter in amplitudes become even larger at the 40th hour (Figure 2.4h).

Figure 2.5a-5h show the surface pressure PSD vs. distance from the hurricane center. Each panel is at the same time interval with Figure 2.4a-4h. In general, pressure data contain larger scatter than seismic data. They also show a smaller decay rate with distance, as we noted in Figure 2.3. Note that these hurricane-related signals merge with the background pressure (PSD) noise level at about 800-900 km from the center and this merging occurs at about the same distance for all time intervals in Figure 2.5a-5h.

We note that the background noise level became higher in Figure 2.5c and Figure 2.5g in comparison to other cases, but even in these data a merging distance with the background seems to occur at about the same distance. An increased level of seismic background noise is seen in Figure 2.4f and also in Figure 2.4g but we believe that they were

caused by M~7 earthquake that occurred elsewhere at about this time (near the Jan Mayen Is.). Large teleseismic earthquakes can raise the background seismic noise level for the frequency range 0.01-0.02 Hz because of long-period surface waves that circle around the Earth. However, there is no reason for barometer data to be affected by teleseismic events. We speculate that there were atmospheric conditions that led to higher pressure PSDs for these time intervals but strictly speaking, we do not know why they occurred in Figure 2.5c and 5g. However, in our analysis, we will focus on the distance range 0-400 km where signals in both data sets are clearly controlled by the hurricane. We believe these differences in background noise levels will not affect our conclusions.

2.3.3. Seismic PSD vs. Pressure PSD at same stations

In Figure 2.6, we show a plot of seismic PSD vs. pressure PSD from the same stations. Stations within 500 km of the hurricane center are plotted at three different time intervals (6:00, 12:00, 18:00 on August 29). For reference, two lines with the power of 1.5 (dash) and 2 (blue) are shown.

Figure 2.6 emphasizes that the relationship between seismic PSD and pressure PSD are not linear. For propagating waves from the 2003 Tokachi-Oki earthquake, Watada *et al.* (2006) showed that seismic amplitude and pressure amplitude were related by a transfer function, which is an example of a linear relation. This was because both pressure and seismic waves were properties of propagating waves. For our hurricane problem, the relationship is clearly more complex as pressure is the excitation source and seismic waves are the resulting field.

2.3.4. Seismic and Pressure data from other cyclones

While Hurricane Isaac is the strongest tropical cyclone that also made landfall most directly through the TA, there are other cyclones that came close and showed similar results in the seismic and pressure PSDs. Examples of three such storms, Hurricane Arthur (Figure 2.7), Tropical Storm Beryl (Figure 2.8) and Tropical Storm Lee (Figure 2.9) are shown here. In each case, the cyclones went through or came near stations in the TA and we can see that the seismic ground velocity PSDs and pressure PSDs follow the same pattern as for Hurricane Isaac. There is a peak in both PSDs near the center of each storm and smaller amplitudes further out towards the edges This confirms that we are seeing a signal from the cyclone itself in the Hurricane Isaac data, and that this is a signal that is consistent with data from other storms. Location information for each storm obtained from NOAA Tropical Cyclones Reports (Brown, 2011; Beven II, 2012; Berg, 2015).

2.3.5. Averaging for seismic PSD and pressure PSD

For later analysis, instead of working with the raw data in Figure 2.4 and Figure 2.5, we took the average PSDs for both data sets. The averaging was done in the following way; first we take a 50-km interval and identify the raw data within this interval. Let us denote raw data within this distance range by x_i (distance) and y_i (PSD) with i=1,2,...,n. We took the average of them and treating it as the data point for this 50-km range. We shifted the 50-km window by every 10 km and applied the same procedure. Near the center (smaller distance range), data are relatively sparse and this procedure sometimes yielded the same

values for adjacent spatial windows. We removed such redundancy in the averaged data and linearly interpolated the averaged data for every 5 km.

This averaging was done in linear numbers rather than in logarithms. Our later analyses are done for these linearly averaged numbers. Therefore, some of the features in small numbers seen in the logarithm plots, that show 3-4 orders of magnitude variations (Figure 2.4 and Figure 2.5), may not be represented well in these averages. We believe that the most important features of a hurricane are in large-amplitude signals and we attempt to understand them, typically closer to the center of a hurricane.

Figure 2.10 shows an example of the averaging process at 00:00 UTC on August 30. The original data, from Figure 2.4d (seismic data, top) and Figure 2.5d (pressure data, bottom) are shown in black. The averaged data is shown in blue and the interpolated data is shown in red. When a blue circle and a black circle overlaps, it is shown by blue in these figures. The averaged PSDs seem to capture most of the long wavelength features in the original data which we seek to understand in this paper.

We added the points at distance 0 km with zero amplitudes in these analyses. This addition is justified for the pressure data as pressure is very low at the center of a hurricane. For seismic data, amplitudes may not necessarily go to zero, although it should also be smaller than those outside the eyewall because the center of a hurricane is a calm region. In the following analysis, we only use data for distances larger than 50 km (up to 400 km) and these added points at distance zero do not affect our results very much.

Figure 2.11 shows the summary of averaged PSDs where the top panel shows seismic PSDs for eight time intervals and the bottom panel shows pressure PSDs for the same time intervals. Here, as observed in Figure 2.4 and Figure 2.5, higher decay rates with distance for seismic data than those for pressure data can be confirmed in those averaged PSDs.

2.3.6. Coherence in the atmospheric pressure field

For the excitation of seismic waves by atmospheric pressure, the source is almost like a random force, distributed over an area, and the correlation length in the pressure field becomes a key parameter for the efficiency of excitation. The correlation length is generally considered to be short and is less than 1 km (Herron, Tolstoy and Kraft, 1969; McDonald, Douze and Herrin, 1971; Nishida *et al.*, 2005) but it may vary with frequency. Since the short coherence length is the critical assumption in the derivation of theoretical formulae, we examined it for our barometric data.

Figure 2.12 shows the coherence for pairs of barometric stations in the TA, plotted against distance between stations. The top figure was computed for a two-hour time interval centered at 12:00 on August 29, only four hours after the landfall and while the hurricane was still quite strong. The coherence between two stations, whose spectra are $X(\omega)$ and $Y(\omega)$, was computed by $E[X^*(\omega)Y(\omega)/\sqrt{E[X^*(\omega)X(\omega)E[Y^*(\omega)Y(\omega)]}]$, where the stars denote complex conjugation. The ensemble averages $E[\]$ were taken by using different overlapping time windows with 30-minute length. Figure 2.12 shows the case when 18 time windows, each shifted by five minutes, were used (over a span of two hours). We then

averaged these coherence values between 0.01 and 0.02 Hz. Results at 18:00 on August 29 are also shown in the bottom panel.

The results in Figure 2.12 indicate that there is no meaningful coherence among barometric data; this is not surprising since a typical distance between adjacent stations in the Transportable Array is 70 km. This does not prove that the correlation length is about 1 km or less but it confirms that the data are consistent with short correlation lengths in the atmospheric pressure field.

2.4. Theory of Stochastic Excitation of Seismic Ground Motion

In this section, we derive a formula that relates the seismic PSD to the pressure PSD. First we state the final formula; it can be written in the form

$$S_{\nu}(x,\omega) = \int K(x,x_{s},\omega)S_{\nu}(x_{s},\omega)dx_{s} \tag{1}$$

where $S_v(x,\omega)$ is the PSD of observed seismic ground velocity at distance x from the center of a hurricane (angular frequency ω), $S_p(x_s,\omega)$ is the surface pressure PSD at x_s , and $K(x,x_s,\omega)$ is the kernel that we can compute for a given Earth model. The integration variable x_s is the source distance measured from the center of a hurricane. The integration arises because the pressure source is distributed over a large area.

The main steps for the derivation of equation (1) proceed as follows. Let us denote the excitation source (that is surface pressure) by $\delta p(\theta_s, \phi_s, t')$. This pressure is distributed over a broad area on the surface of the Earth. The source has also acted continuously over

time. Multiplied by the surface area, this pressure becomes a surface vertical force. Vertical seismic ground velocity by such a vertical force can be written by

$$v_z(\theta,\phi,t) = \int d\theta_s \int d\phi_s \sin\theta_s R^2 \sum_{n,l,m} U_n^2(R) Y_l^m(\theta,\phi) Y_l^{m^*}(\theta_s,\phi_s)$$

$$\times \int_{-\infty}^{t} dt' \, e^{-\frac{\omega_i(t-t')}{2Q_i}} \cos\omega_t(t-t') \delta p(\theta_s, \phi_s, t') \tag{2}$$

where we use the normal mode theory for a layered spherical earth (Gilbert, 1970; Dahlen and Tromp, 1998). The integrations over the colatitudes θ_s and the longitude ϕ_s are carried out for the Earth's surface (that is the extent of the pressure source). The integration with respect to time (t') indicates that this pressure source has acted from $t' = -\infty$ to t. R is the radius of the Earth, $Y_l^m(\theta,\phi)$ is the spherical harmonics (e.g. Edmonds, 1996), $U_n(R)$ is the surface value of the vertical eigenfunction for a spheroidal mode with a mode number i=(n,l,m) which is normalized by $I=\int_0^R \rho \{U^2+l(l+1)V^2\}r^2dr$. The overtone number is n, the angular degree and order of a spherical harmonics are l and m, and m and m and m are the eigenfrequency and the attenuation parameter of this mode. We use m as a shorthand notation for a mode with m, m. The formula contains $U_n^2(R)$ because both the excitation source and a seismograph are at the Earth's surface.

From (2), we form the auto-correlation function of ground velocity

$$C_{v}(\theta,\phi,\tau) = \frac{1}{T} \int_{-T/2}^{T/2} v \ (\theta,\phi,t) v_{z}(\theta,\phi,t+\tau) dt \tag{3}$$

Using the relation that Fourier transformation of an auto-correlation is its power spectral density (PSD), we have

$$S_{v}(\theta,\phi,\omega) = \int_{-\infty}^{\infty} C_{v}(\theta,\phi,\tau)e^{-i\omega\tau}d\tau \tag{4}$$

We substitute (2) in (3) and then (3) in (4). When we do this, the cross-correlation function of surface pressure between $(\theta_{S'}, \phi_{S'})$ and $(\theta_{S''}, \phi_{S''})$ emerges:

$$C_{p}(\theta_{s'}, \phi_{s'}, \theta_{s''}, \phi_{s''}, \tau) = \frac{1}{T} \int_{-T/2}^{T/2} \delta p(\theta_{s'}, \phi_{s'}, t) \delta p(\theta_{s''}, \phi_{s''}, t + \tau) dt$$
 (5)

By defining the cross power spectral density of pressure by its Fourier transformation

$$S_p(\theta_{s'}, \phi_{s'}, \theta_{s''}, \phi_{s''}, \omega) = \int_{-\infty}^{\infty} C_p(\theta_{s'}, \phi_{s'}, \theta_{s''}, \phi_{s''}, \tau) e^{-i\omega\tau} d\tau$$
(6)

we obtain the following expression,

$$S_{v}(\theta,\phi,\omega) = \int d\theta_{s'} \int d\phi_{s'} \int d\phi_{s''} \int d\phi_{s''} \sin \theta_{s'} \sin \theta_{s''} R^{4}$$

$$\sum_{l'} \sum_{l''} \frac{2l'+1}{4\pi} \frac{2l''+1}{4\pi} U_{l'}^2 U_{l''}^2 \gamma_{l'} \gamma_{l''}^* P_{l'} \cos\Delta' P_{l''} \cos\Delta'' S_p(\theta_{s'}, \phi_{s'}, \theta_{s''}, \phi_{s''}, \omega)$$
 (7)

where

$$\gamma_{l'} = \frac{\left(\frac{\omega_{l'}}{2Q_{l'}} - i\omega\right)}{\left(\frac{\omega_{l'}}{2Q_{l'}} - i\omega\right)^2 + \omega_{l'}^2} \tag{8}$$

for l'. Substitution of l'' in l' gives the expression for $\gamma_{l''}$. The star in (7) denotes the complex conjugation. Δ' is the distance between the observation point (θ, ϕ) and a source $(\theta_{s'}, \phi_{s'})$ and Δ'' is the distance between the observation point (θ, ϕ) and a source $(\theta_{s''}, \phi_{s''})$. Here we restricted to the fundamental modes only as the overtones are not excited very well by surface forces.

Under the assumption that the correlation length in the surface pressure field is much smaller than the wavelength of seismic waves, we can simplify equation (7) further. This condition is satisfied in our problem because the wavelengths of seismic waves are over 100 km for the frequency range 0.01-0.02 Hz whereas the correlation lengths of pressure are of the order of 1 km or smaller for this frequency range (Herron, Tolstoy and Kraft, 1969; McDonald, Douze and Herrin, 1971; Nishida *et al.*, 2005). Figure 2.12 lends some support for this assumption. We can then approximate the double surface integrals in (7) by a single surface integral multiplied by πL^2 where L is the correlation length. This approximation means that if two points are within the distance L, the correlation in the pressure field is 1 but otherwise it is 0.

We also introduce the assumption of axisymmetry into this problem as we discussed with Figure 2.3. Equation (7) can then be approximated by

$$S_{\nu}(x,\omega) = \int K(x,x_s,\omega) S_{\nu}(x_s,\omega) dx_s \tag{9}$$

where the kernel is explicitly written by

$$K(x, x_s, \omega) = \frac{L^2}{4\pi} R \sin \theta_s' \sum_{l'} \sum_{l''} (l' + 1/2) (l + 1/2) U_{l'}^2 U_{l''}^2 \gamma_{l'} \gamma_{l''} \int P_{l'} \cos \Delta' P_{l'''} \cos \Delta'' d\phi_s$$
(10)

In this formula, x_s is the distance from the center of a hurricane and the integration with respect azimuth is now in the kernel. Under this assumption, the pressure PSD S_p has an axisymmetric form whose example is shown in Figure 2.13a. In (10), $x = R\theta$ is the

distance from the hurricane center to a seismograph on the surface of the Earth, $x_s = R\theta_s'$ is the distance from the hurricane center to a pressure source (which is distributed over the surface) and Δ' is the distance between the observation point (θ, ϕ) and a source (θ_{sr}, ϕ_{sr}) . Using the eigenfunctions and eigenfrequencies of PREM (Dziewonski and Anderson, 1981), we numerically evaluate the formula (10). Examples of kernels for sources at $x_s = 50$ -350 km are shown for every 50 km in Figure 2.13b. Note that the sources are on a concentric circle at each distance as the integrations with respect to azimuth were already performed. We used L=1 km for these computations.

2.5. Solving for the correlation length

From the Earthscope network, we have S_v and S_p in (1). In our analysis, we use the averaged PSDs in Figure 2.11 for these observed quantities. We quickly found out that the relation in (9) cannot fit the data well if the correlation length were constant. Therefore we sought spatially varying correlation length L^2 that can satisfy the two data.

In order to obtain L^2 , we formulated an inverse problem whose unknown parameter is this correlation length. This parameter is buried in the kernel in equation (10). We now rewrite the equation as

$$S_{\nu}(x) = \int \overline{K}(x, x_s) S_{\nu}(x_s) L^2(x_s) dx_s$$
 (11)

where \overline{K} is the same with (10) except that L^2 is taken out of the formula and is explicitly shown in the integrand. We used this equation to solve for the correlation length where $L^2(x_s)$ is a function of the distance from the center of the hurricane. Since the quantities S_v

and S_p were averaged between 0.01 and 0.02 Hz, we used the averaged kernel for the same frequency band and thus the resultant correlation length should also be interpreted as an averaged quantity.

In order to solve this problem, we discretized the integral in (11) at every 5 km from the distance 50 km to 400 km. The results of inversion for the first four time intervals are shown in Figure 2.14a-d. They are at UTC 0600 (14a), 1200 (14b), 1800 (14c) on August 29 and UTC 0000 (14d) on August 30. Each solution consists of three panels; the obtained correlation lengths with error bars are shown in the top panel, comparison of the observed (averaged) seismic PSDs (red) and the theoretical PSDs (dashed blue) are in the middle panel and the pressure PSDs are in the bottom panel. The solution was obtained by minimizing the differences between the two curves in the middle panel. The red lines in the middle panels and the pressure PSDs in the third panels are the same with those shown in Figure 2.10. Note that these plots are all in linear, not in log.

In Figure 2.14, the correlation lengths have large values for distances less than 200 km and become small beyond 200 km. The maximum correlation length is 1.5 km when the hurricane was mature and strong (Figure 2.14a) but became small over time as Hurricane Isaac lost its energy after the landfall. The fact that the correlation length becomes large near the center of the hurricane is the most characteristic features in these solutions.

This inversion problem required regularization. We used a simple diagonal damping parameter with first-derivative smoothing for adjacent (5-km) blocks. Examples of the trade-

offs between the solution norms and the variance (misfits) are shown in Figure 2.15. They are for the first two time intervals (Figure 2.14a and 14b) and the chosen damping parameters are indicated by the red circles. A different choice of damping parameter changes solutions to some extent but as long as a damping parameter is selected near the red circle, solutions are fairly stable.

We did not use the positivity constraint for solving this problem. If a selected damping parameter is too small, a solution often contained some negative regions. Selected damping parameters give basically zero solutions beyond certain distances (typically 250 km). Replacing those large-distance solutions by zeros does not significantly change the fit.

2.6. The cubic model

We searched for characteristic features in the solutions; one of the most interesting features is the existence of a correlation between L^2 and the pressure PSD S_p . In Figure 2.16, we show three different cases of inversion results with different damping parameters. Our chosen solution is the bottom one but in order to stress that the relation is a robust feature among our solutions, two other cases are shown. The damping parameter is 100 times smaller for the top panel and is 10 times smaller for the middle panel.

The data points in Figure 2.16 suggest existence of a systematic trend between L^2 and the pressure PSD S_p . We also show the least squares formula (log-log linear) that fit the data. In the formulas shown in these figures, x is $\ln(L^2)$ and y is $\ln(S_p)$. The numbers in the parentheses are the standard deviations (one sigma). We find that the coefficient of x stays

close to 0.5 for all three cases (0.516, 0.497, 0.536) despite the fact the damping parameter varied by a factor of 100.

What does a gradient of 0.5 mean in this least-squares solutions? Since x is $\ln(L^2)$ and y is $\ln(S_p)$, it obviously means that $L \propto S_p$. Let us introduce a proportionality constant α and write this relation by $L = \alpha S_p$. This relation means that, since the excitation is proportional to L^2S_p , the excitation source essentially becomes proportional to S_p^3 . If we rewrite equation (11) by using this relation, we get

$$S_{\nu}(x) = \alpha^2 \int \overline{K}(x, x_s) S_{\nu}^3(x_s) dx_s \tag{12}$$

The integrand shows that the excitation of seismic waves becomes proportional to the third power of the pressure. We refer to this as the cubic model.

We refitted the data (the bottom case in Figure 2.16) by the least-squares method by fixing the gradient at 0.5 and varying only the constant. The formula we obtained is

$$\ln(S_p) = 0.5 \ln(L^2) + 6.572 \tag{13}$$

and is also shown in the bottom panel of Figure 2.17. This formula essentially means that we have a relation

$$L = (1/714.8)S_p(x) \tag{14}$$

where the unit for L is m and the unit for S_p is m²/s. The constant 714.8 is equal to $e^{6.572}$. Using this relation, we computed theoretical values for this cubic model using (12). Comparison between theory and data is shown in Figure 2.17 (top). If our theory and

observations match, the points should lie on the dashed line in this figure. There are certainly some scatters in this plot but this cubic model seems to explain a major trend in data.

A caveat for this cubic model is that it is a better model for large pressure region or equivalently for small-distance range. Typically the fits are good for distances less than 250 km. The bottom panel of Figure 2.17 shows that the scatter of points from the least-squares line becomes large for small correlation lengths. But since the dominant signals are from the distance range 0-250 km, the cubic model seems to capture important characteristics of the excitation process.

2.7. Discussion

2.7.1. Alternative mechanisms

In this study, we identified one key observational feature, the difference in decreasing rates with distance between seismic and barometric data. We attributed these differences to variations in the correlation length in the pressure field as a function of distance from the center of the hurricane. However, there can be other possibilities that may explain the observational feature. We will discuss two possible mechanisms below.

One mechanism is the transient sources (pressure changes) close to the hurricane center. As strong winds blow into the small, central area of a hurricane, it seems natural to expect transient (intermittent) pressure changes because of strong turbulence. If they occurred frequently, we could have an effectively centralized source for seismic-wave

excitation. In order to examine this point, we created amplitude (PSD)-distance plot for every hour (Figure 2.18, Appendix) from 00:00, August 29 to the end of August 31. Hourly changes in these plots indicate that there exist some variations, suggesting some stochastic effects in pressure values. But we do not necessarily see a larger number of sudden changes closer to the center; stochasticity seems to be found regardless of distance from the center. But these data are limited, especially because we can only get a limited number of stations close to the center. Clearly a more careful analysis is required.

The second mechanism is the high temporal coherence close to the center. Instead of spatial coherence, temporal coherence may also increase when strong winds blow into a small, central area of a hurricane. If this happens, there will be a centralized source that can explain the observed feature. Although this mechanism is possible, the small number of barometric stations close to the center makes it hard to observe. Also a new theory needs to be developed as the theory in this paper does not take into account the temporal coherence.

2.7.2. Effects of pressure waves and strong winds on barometer data

The following are not alternative models but are points that need careful consideration. First is that the barometer data may contain laterally propagating pressure waves that may lead to an overestimation of pressure sources. Second is the effect of dynamic pressure originated by strong winds.

The reason we are concerned about propagating pressure waves is that if they propagate in the near-surface atmosphere, they should change surface pressure due to its

dynamical effects in the atmosphere but they may be a poor source of seismic-wave excitation. Simple transmission of pressure waves into the solid Earth is possible but these pressure waves do not excite seismic waves. If so, our use of barometer data may be an overestimation of pressure as we regard the entire barometer signals as the excitation source. This problem can be solved if we could identify pressure waves and remove them, but identifying pressure waves is not straightforward. This is because phase information is quite complicated due to a spatially extended source. Therefore, we examined amplitude (PSD) information, such as those in Figure 2.18 (Appendix). This figure shows amplitude (PSD)distance plots of pressure for every hour over three days. In going through the plots in Figure 2.18, we noticed some cases that hint towards waves which propagate outward from the center. However, these oscillatory-wave like features occur only in restricted azimuths. In other words, they are not coherent waves that propagate outward from the center. Therefore, these occasional high-amplitude data are not likely to be propagating waves. We believe they are more likely to be stochastic fluctuations in the pressure field. This does not prove that pressure waves in the near-surface atmosphere do not exist but clearly they cannot have much effects on our analysis.

Strong winds may be an important source for the excitation of seismic waves, especially for horizontal-component seismograms as they can apply shear forces directly on the ground. In this paper, we have avoided such a mechanism by analyzing only barometer data and vertical-component seismograms. Even so, strong winds may cause surface pressure changes through its dynamical effects. In order to explain our observation,

however, winds should be strong at distant locations from the center and also remain inefficient to excite seismic waves. This may occur but such a scenario appears quite ad hoc. In our next step, we intend to clarify this situation by testing such a mechanism by using wind data and horizontal—component seismograms.

2.8. Conclusion

Taking advantage of seismic and barometer data from the Earthscope network, we studied the data for Hurricane Isaac (2012) after its landfall. The key observation is that seismic amplitudes (PSD) decay much more quickly than pressure amplitudes (PSD) with distance from the center of this hurricane. In order to explain this observation, we developed a stochastic excitation theory for seismic-wave generation by surface atmospheric pressure changes. We have both the excitation-source information (barometers) and the resultant seismic wave fields (seismometers) from the Earthscope data.

We proposed a model that used the variations in the pressure correlation length to explain the key observational feature. The inverted solutions for the correlation length showed large correlation length close to the center (~ 1-1.5 km at a distance of 70-80 km) and small near-zero correlation length outside of 250 km from the center. The differences in decaying rate are explained by this model.

In our solutions, there is an interesting relation between the pressure and the derived correlation length. Our scaling analysis led to a model in which the excitation source power is proportional to the third power of pressure. This model means that the excitation source

becomes stronger near the center of a hurricane; the excitation power becomes more localized closer to the center. Such a centralized source can explain the key observation on the decaying-rate differences.

There may be other mechanisms, however, that can lead to an effectively centralized source. They include higher temporal coherence or frequent transient pressure changes near the center due to strong turbulence. Although we do not see strong evidence for such effects, the current data sets are quite limited due to sparsity near the center; these mechanisms need to be studied more carefully in the future.

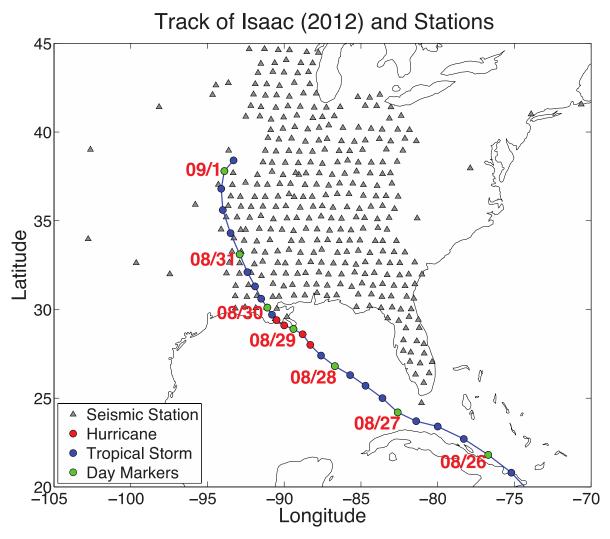


Figure 2.1: Track of Hurricane Isaac (August, 2012) and seismic stations from Earthscope (grey triangles). Blue circles indicate when Isaac was a tropical storm, red circles indicate its hurricane stage and green circles are the day markers (0000 UTC for each day).

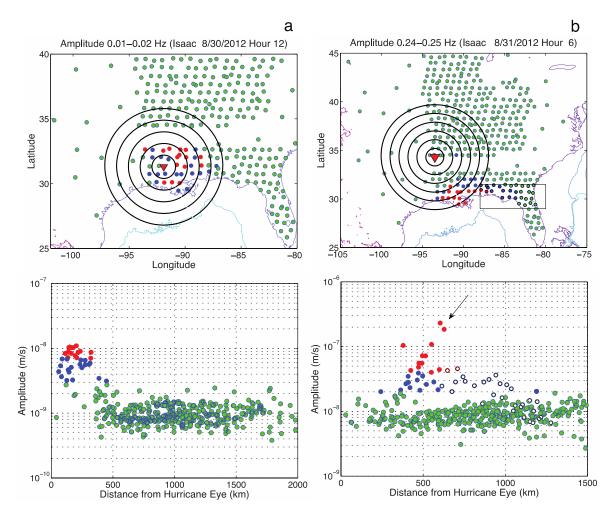


Figure 2.2: Seismic amplitudes and locations of Hurricane Isaac. Locations of the hurricane are indicated by red triangles. The top panels show seismic amplitudes on a map in three colors and the bottom panels show the amplitude-distance plot from the center of the hurricane (red triangle). Concentric circles are given for every 100 km from the center. (A) Most of seismic waves between 0.01 and 0.02 Hz (left two panels) emanate from the center of the hurricane as high-amplitude stations (red and blue) are found within the same concentric circles. Red circles indicate amplitudes higher than 7.0e-9 (m/s), blue circles are between 3.0e-9 and 7.0e-9 (m/s) and green circles are below 3.0e-9 (m/s). (B) The right two panels show that seismic waves between 0.24 and 0.25 Hz. The highest amplitudes are found near the coast (red) and the arrow in the bottom panel indicates that amplitudes decreased from the coast toward the center of the hurricane. Stations in northern Florida, within the rectangular box in the top panel, are shown by white circles in the bottom panel and indicate that these near-coastal stations also have anomalously high amplitudes.

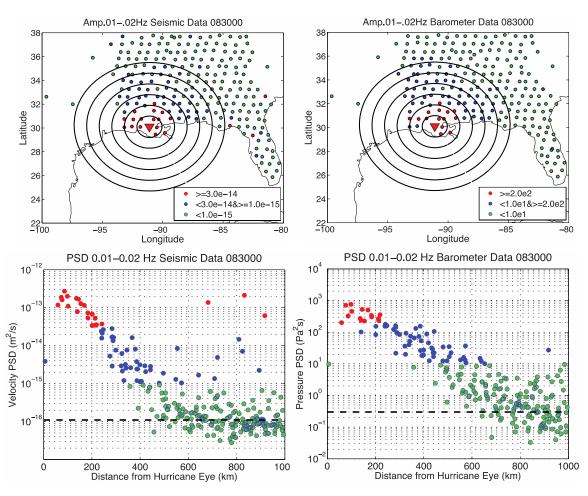


Figure 2.3: (Left-top) Seismic PSD on a map for the frequency range 0.01-0.02 Hz and the location of Hurricane Isaac (red triangle) at UTC 0000, Aug. 30. (Left-bottom) Same seismic data plotted against distance from the hurricane center. Same color scale is used for amplitudes. (Right-top) Surface-pressure PSDs from barometer data on a map for 0.01-0.02 Hz for the same time interval with seismic data. (Right-bottom) Pressure PSD plotted against distance from the hurricane center. Three colors are used to denote PSD amplitudes for the top and bottom panels.

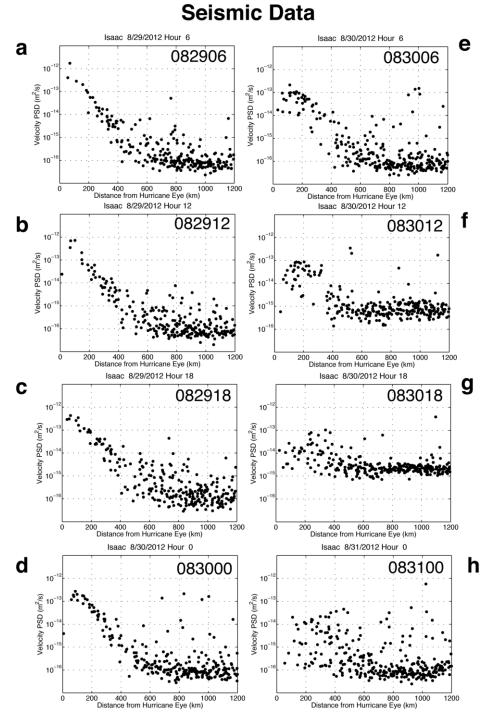


Figure 2.4: Seismic PSD vs. distance from the hurricane centers at each time interval. (a) is at UTC 0600, Aug. 29. Data at every six hours are shown in (a)-(g) until UTC 0000, Aug. 31.

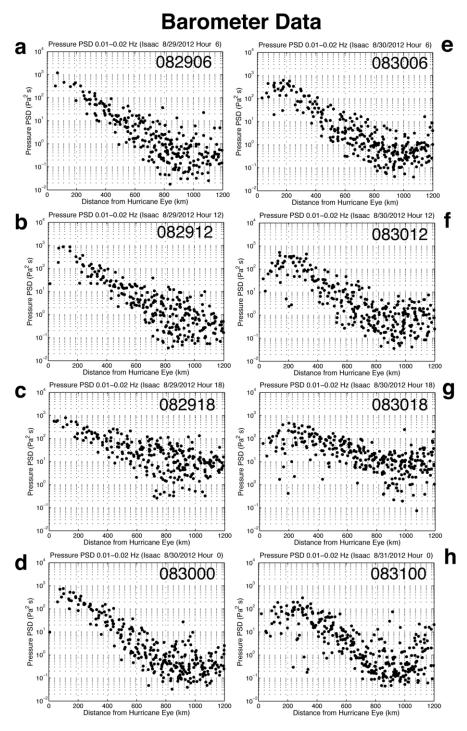


Figure 2.5: Pressure PSD vs. distance plots from barometer data. Same time intervals with Figure 2.4 are shown.

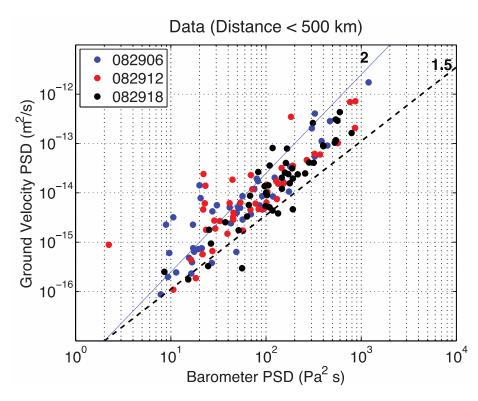


Figure 2.6: Stations within 500km from the hurricane center are plotted for three time intervals, 6:00, 12:00, and 18:00 on 29 August. For reference, two lines for the power of 1.5 (dash) and 2.0 (blue) are shown. Seismic PSD and pressure PSD are not linear.

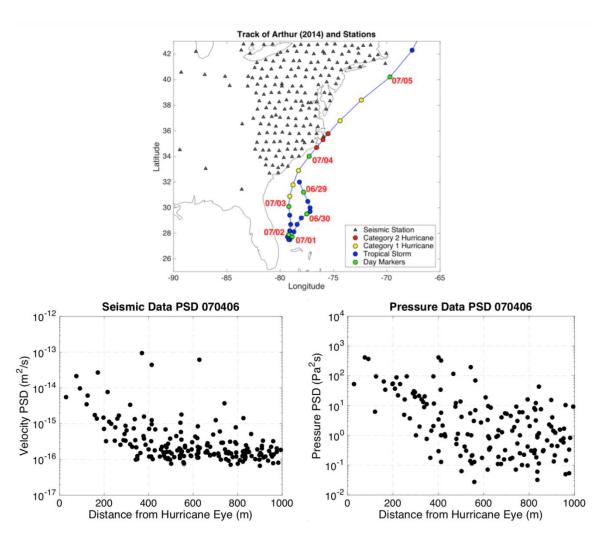


Figure 2.7: Map of track of Hurricane Arthur (top) and one hour of the seismic PSD (bottom, left) and pressure PSD (bottom, right) with distance.

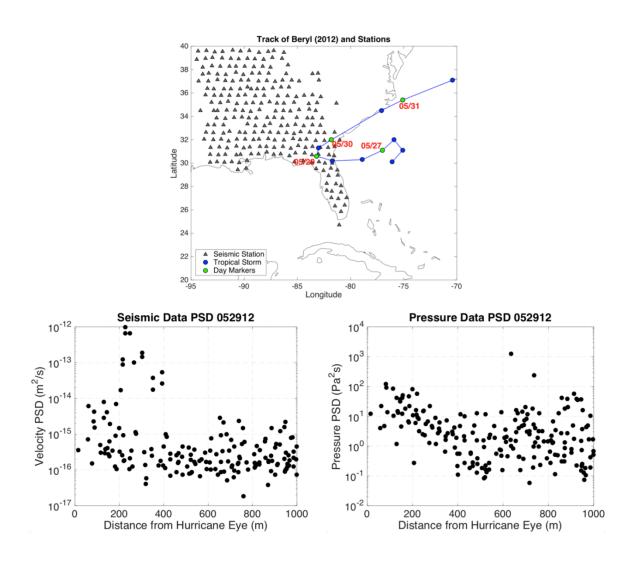


Figure 2.8: Map of track of Tropical Storm Beryl (top) and one hour of the seismic PSD (bottom, left) and pressure PSD (bottom, right) with distance.

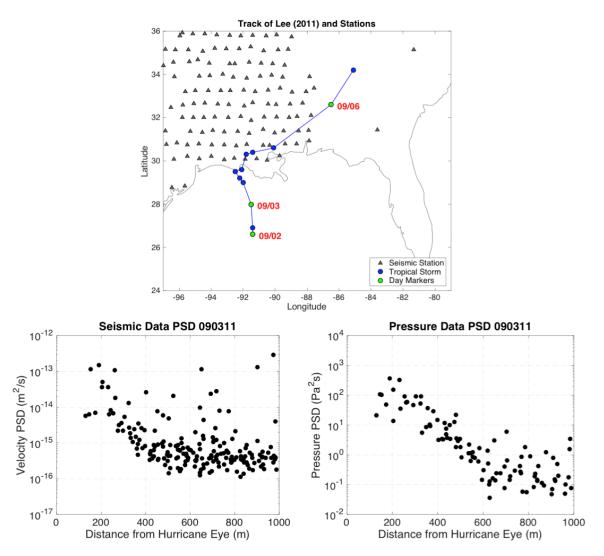


Figure 2.9: Map of track of Tropical Storm Lee (top) and one hour of the seismic PSD (bottom, left) and pressure PSD (bottom, right) with distance.

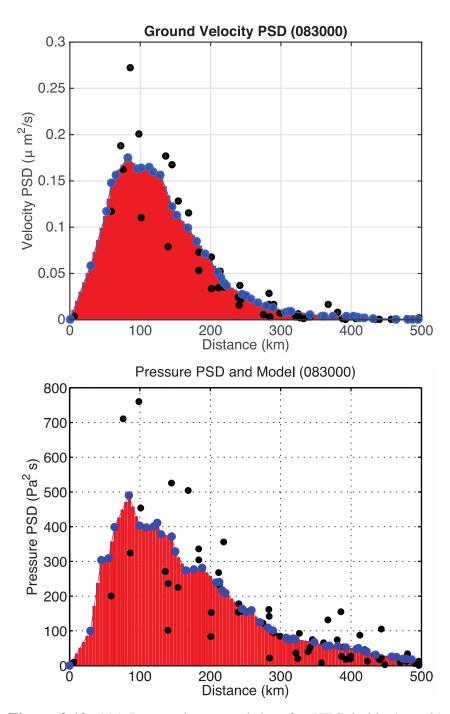


Figure 2.10: (5a) Raw and averaged data for UTC 0600, Aug. 29. Seismic data are at top and pressure data are at bottom. Black circles are raw data, blue are averaged data and the red region indicates the interpolated PSDs that we used for analysis. (5b) Same with 5a but for UTC 0000, Aug. 30.

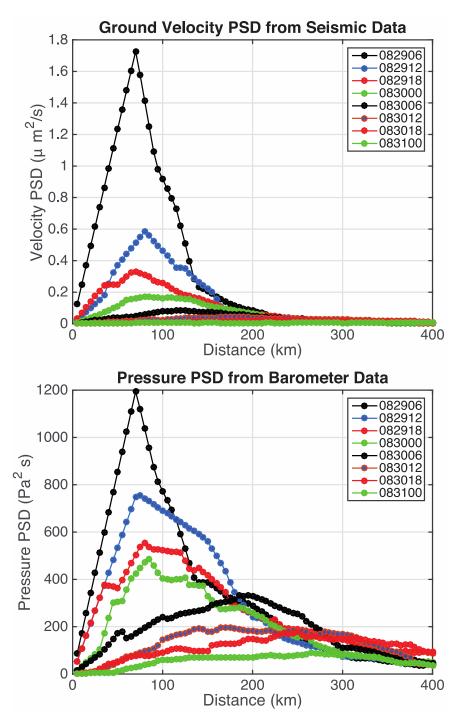


Figure 2.11: Summary of the averaged PSDs for seismic data (top) and pressure data (bottom). Results at eight time intervals are shown from UTC 0600, Aug. 29 to UTC 0000, Aug. 31 at every six hours

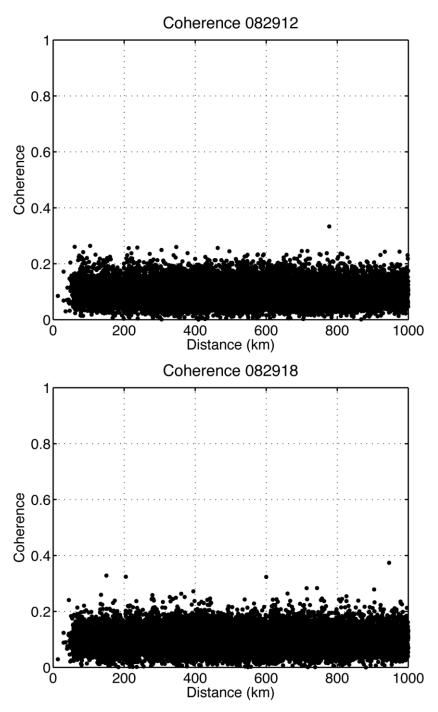


Figure 2.12: Coherence for all pairs of barometric stations within the distance of 1000 km from the hurricane center. Two hour time intervals were used to compute those results. The correlation length in the atmospheric pressure field is much smaller than the distance scale shown here.

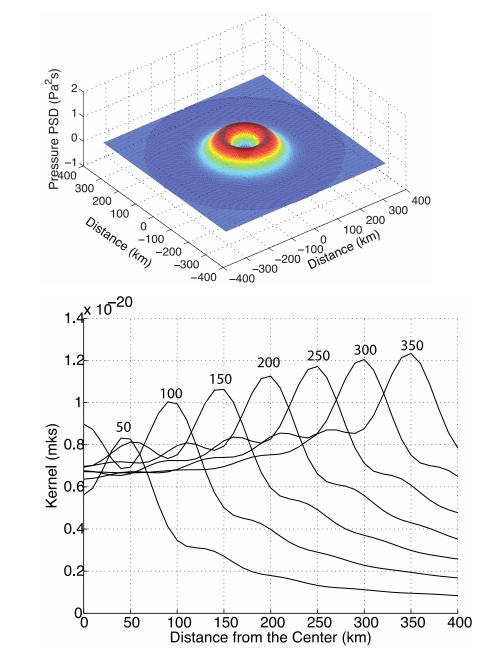


Figure 2.13: a) An example of pressure PSD under the assumption of axisymmetry. For Hurricane Issac, the peak is at about 70-80 km from the center. b) Some examples of kernels $K(x, x_s, \omega)$. Seven curves for $x_s = 50-350$ km at every 50 km are shown. These kernels are averaged between 0.01 and 0.02 Hz

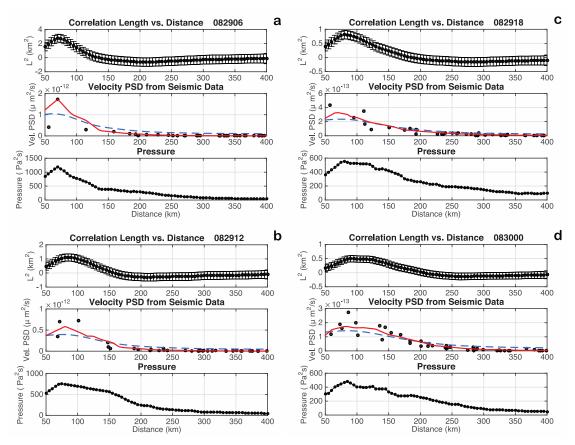


Figure 2.14: (a) Results of inversion for the correlation length. Correlation length is in the top panel with error bars, seismic PSD are in the second panel, and pressure PSD is in the bottom panel. Fitting is done for seismic PSD where the data are red and theoretical fit is in dashed blue (middle panel). This is at 0600, Aug. 29. (b) Same with (a) except that these are at UTC 1200, Aug. 29. (c) Same with (a) except that they are at UTC 1800, Aug. 29. (d) Same with (a) except that they are at UTC 0000, Aug. 30.

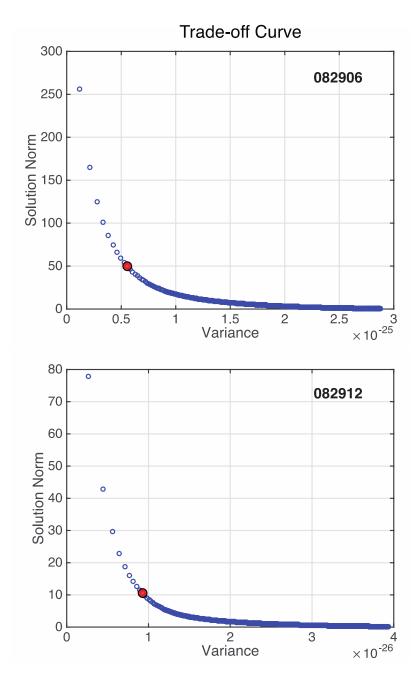


Figure 2.15: Examples of the trade-off curves for the inversions in Figure 2.12. The top panel is for UTC 0600 Aug. 29 and the bottom is for UTC 1200, Aug. 29. The solution norms are plotted against the misfit in seismic PSD data. The red circles are the selected values.

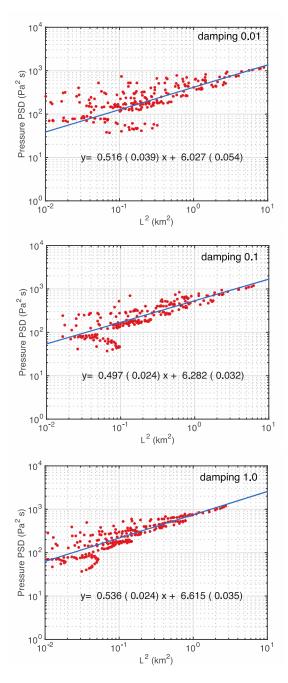


Figure 2.16: Plot of the correlation lengths vs. the pressure PSD for three different cases of damping parameters. From top to bottom, the damping parameter varied by a factor of 100 (0.01-0.1-1.0). Lines are the least squares fit to data. The main point of this figure is the relatively stable coefficient of about 0.5 in the least squares formula. In this formula, y is the logarithm of pressure and x is the logarithm of L^2 .

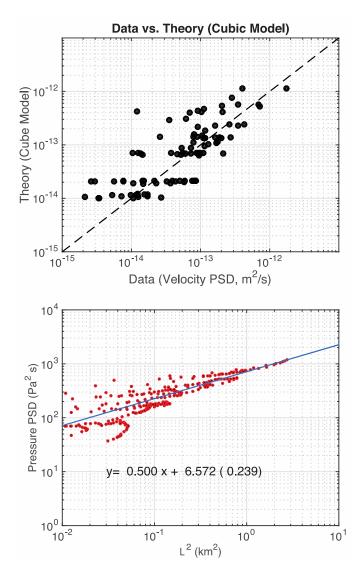
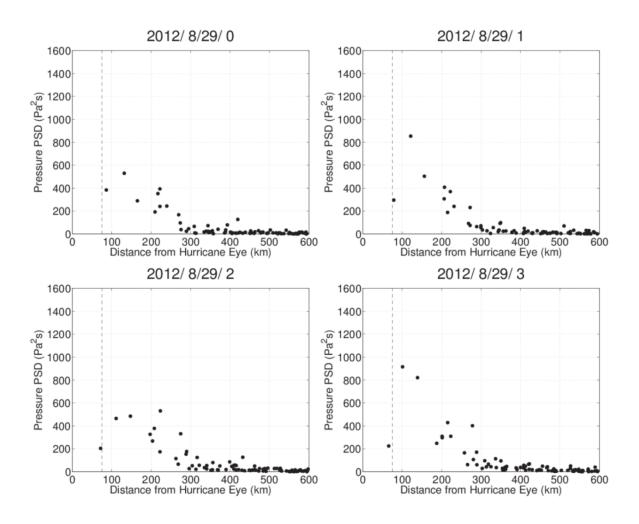
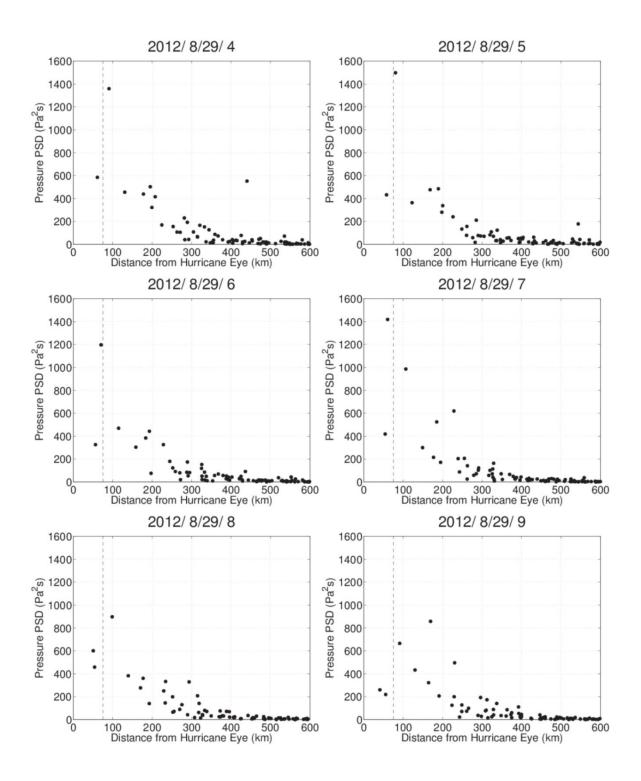


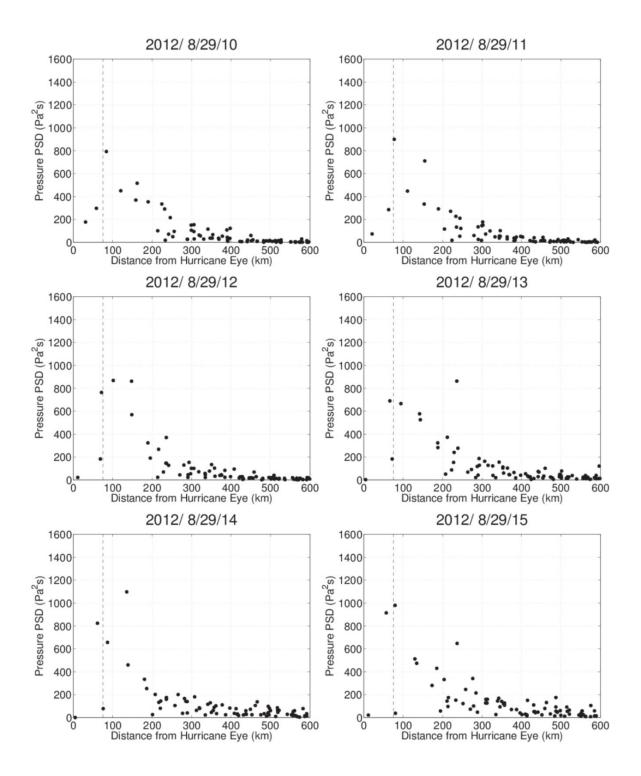
Figure 2.17: (a) Comparison of theory and data for the cubic model. There are some scatters but the cubic model seems to explain the overall trend in data. (b) The cubic model was derived by fitting the data (same data with the bottom panel in Figure 2.16) by fixing the gradient as 0.5. This means that there is a relation between the correlation length and pressure PSD as $L = (1/714.8)S_p(x)$ (see text).

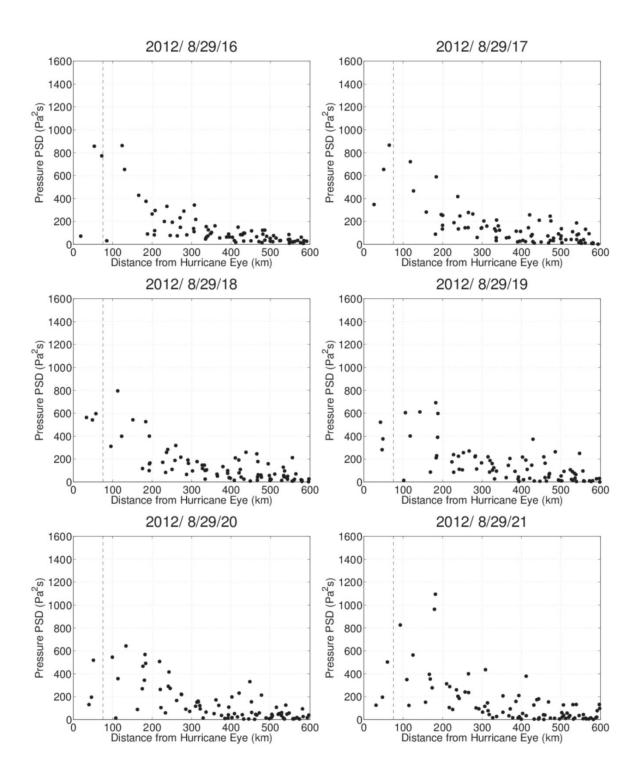
2.9. Appendix

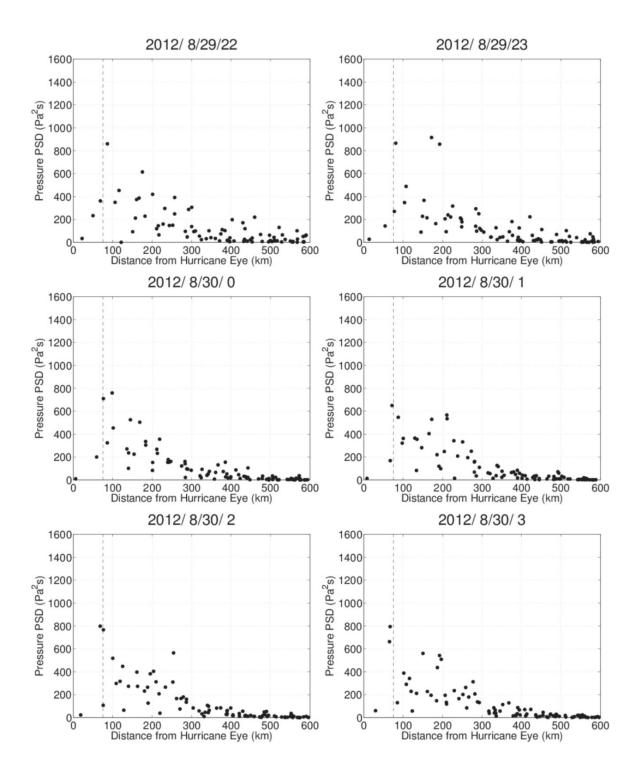
Figure 2.18: Amplitude (PSD) vs. distance plot of surface-pressure data from the center of Hurricane Isaac. Plots at every hour from UTC 00:00, August 29, to UTC 00:00, September 1, are shown. It consists of 73 figures over three days.

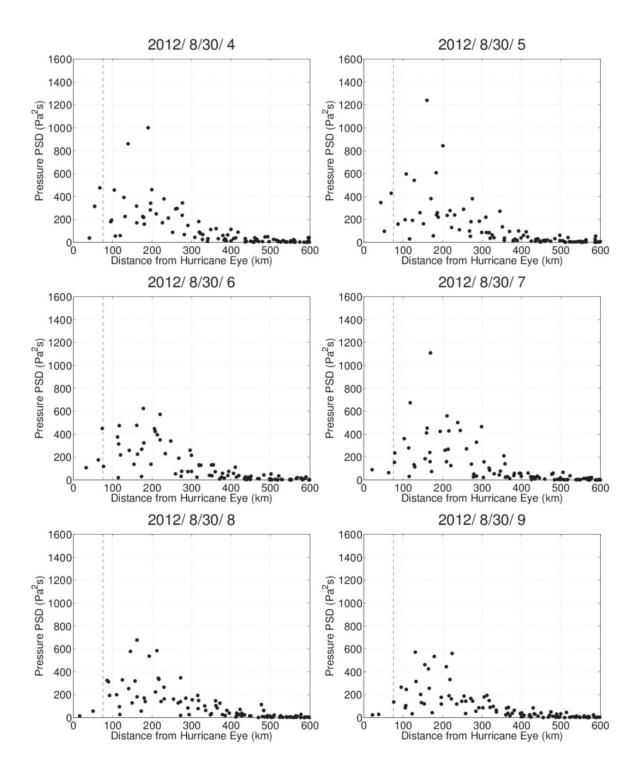


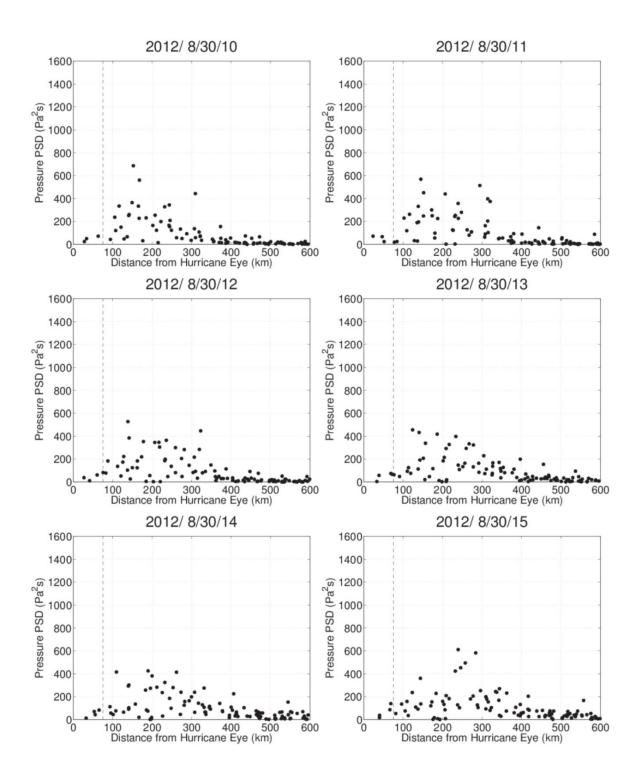


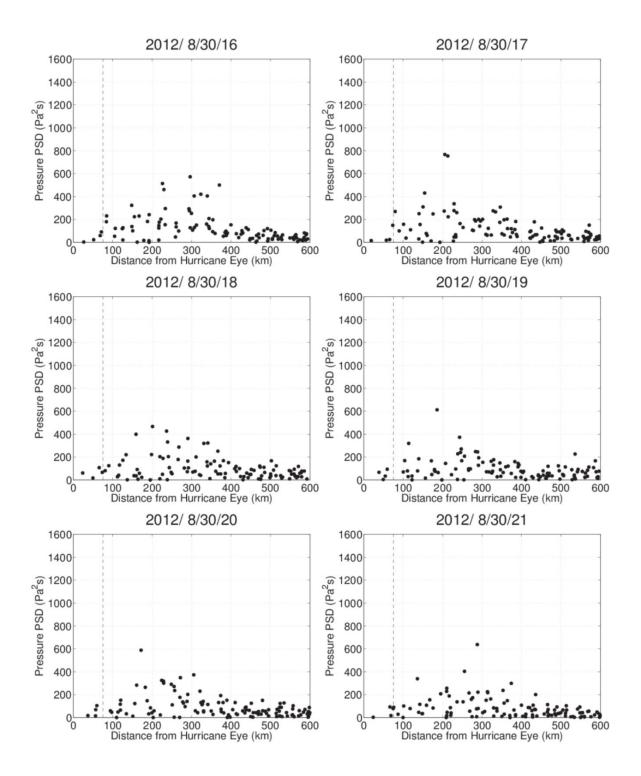


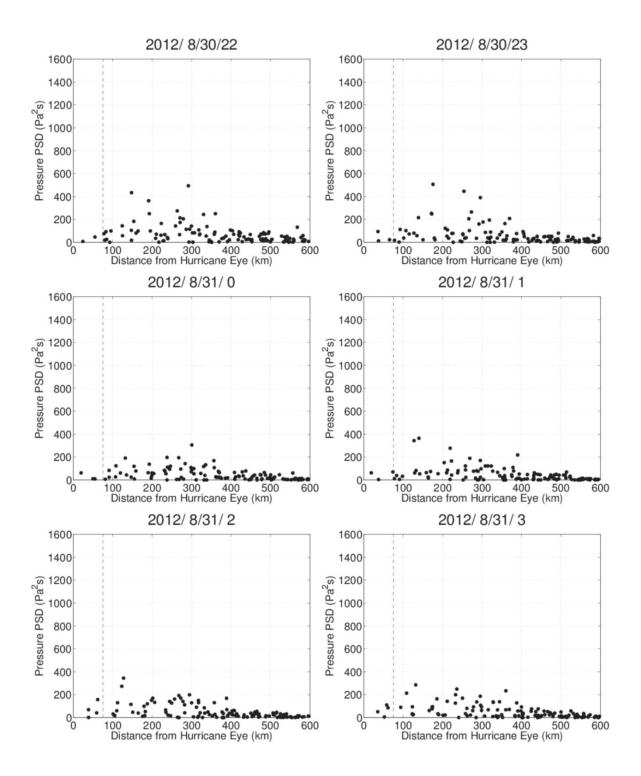


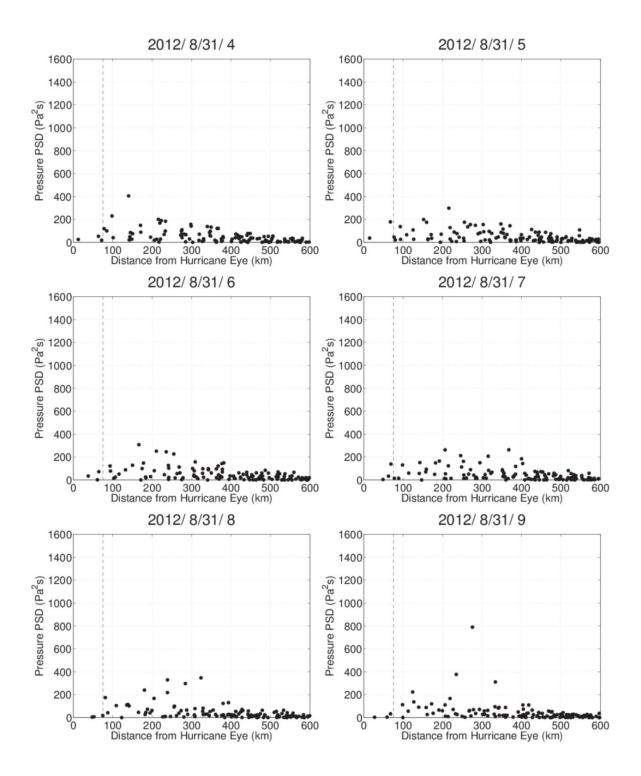


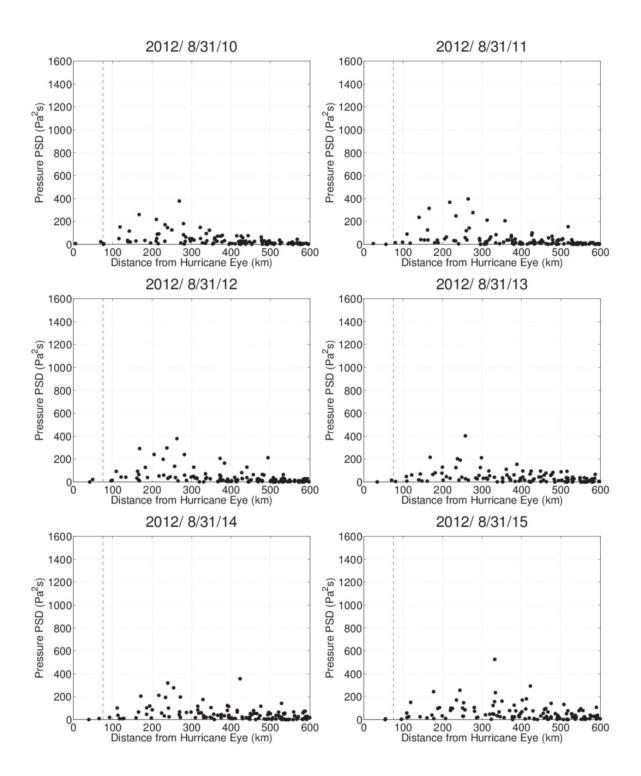


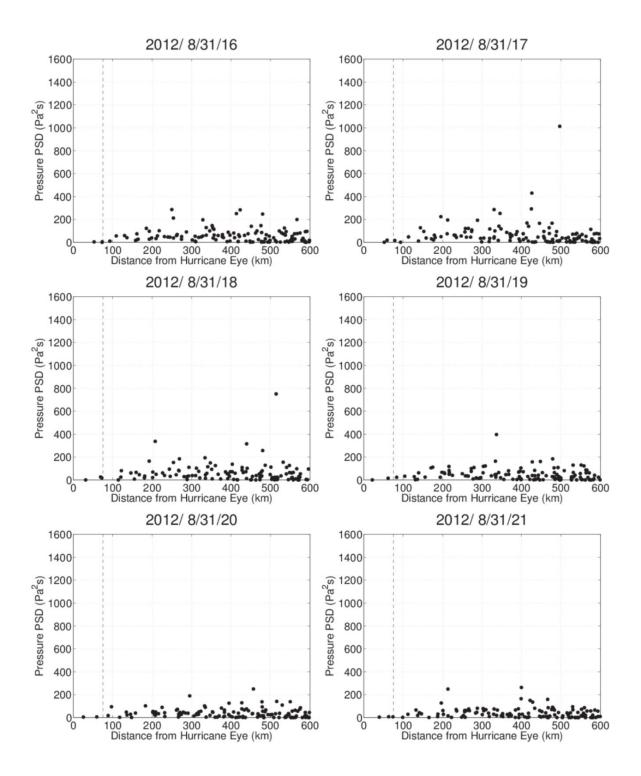


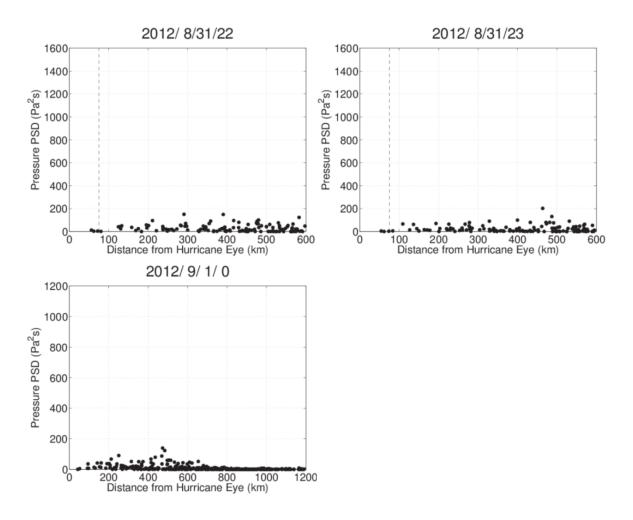












2.10. References

Berg, R. (2013) 'Tropical Cyclone Report: Hurricane Isaac (AL092012) 21 August - 1 September 2012'. Miami, FL: NOAA/National Weather Service.

Berg, R. (2015) 'Tropical Cyclone Report, Hurricane Arthur (AL012014) 1-5 July 2014.'
Miami, FL: NOAA/National Weather Service.

Beven II, J. L. (2012) 'Tropical Cyclone Report: Tropical Storm Beryl (AL022012) 26-30 May 2'. Miami, FL: NOAA/National Weather Service.

Bromirski, P. D. and Kossin, J. P. (2008) 'Increasing hurricane wave power along the U.S.

- Atlantic and Gulf coasts', *Journal of Geophysical Research: Oceans*, 113(7), pp. 1–10. doi: 10.1029/2007JC004706.
- Brown, D. P. (2011) 'Tropical Cyclone Report: Tropical Storm Lee (AL132011) 2-5 September 2011'. Miami, FL: NOAA/National Weather Service.
- Chi, W. C. et al. (2010) 'Seismic monitoring of western Pacific typhoons', Marine Geophysical Research, 31(4), pp. 239–251. doi: 10.1007/s11001-010-9105-x.
- Dahlen, F. A. and Tromp, J. (1998) *Theoretical global seismology*. Princeton University Press.
- Dziewonski, A. M. and Anderson, D. L. (1981) 'Preliminary reference Earth model',

 Physics of the Earth and Planetary Interiors, 25(4), pp. 297–356. doi: 10.1016/0031-9201(81)90046-7.
- Ebeling, C. W. and Stein, S. (2011) 'Seismological identification and characterization of a large hurricane', *Bulletin of the Seismological Society of America*, 101(1), pp. 399–403. doi: 10.1785/0120100175.
- Edmonds, A. R. (1996) *Angular momentum in quantum mechanics*. Princeton University Press. Available at: http://www.jstor.org/stable/j.ctt1cx3v9p (Accessed: 3 May 2018).
- Emanuel, K. (1991) 'The Theory Of Hurricanes', *Annual Review of Fluid Mechanics*, 23(1), pp. 179–196. doi: 10.1146/annurev.fluid.23.1.179.
- Emanuel, K. (2003) 'Tropical Cyclones', *Annual Review of Earth and Planetary Sciences*, 31(1), pp. 75–104. doi: 10.1146/annurev.earth.31.100901.141259.

- Emanuel, K. A. (1986) 'An Air-Sea Interaction Theory for Tropical Cyclones. Part I: Steady-State Maintenance', *Journal of the Atmospheric Sciences*, 43(6), pp. 585–605. doi: 10.1175/1520-0469(1986)043<0585:AASITF>2.0.CO;2.
- Emanuel, K. A. (1997) 'Some Aspects of Hurricane Inner-Core Dynamics and Energetics', *Journal of the Atmospheric Sciences*, 54(8), pp. 1014–1026. doi: 10.1175/1520-0469(1997)054<1014:SAOHIC>2.0.CO;2.
- Farra, V. *et al.* (2016) 'Ray-theoretical modeling of secondary microseism *P* waves', *Geophysical Journal International.* Oxford University Press, 206(3), pp. 1730–1739.

 doi: 10.1093/gji/ggw242.
- Fukao, Y. et al. (2002) 'A theory of the Earth's background free oscillations', Journal of Geophysical Research: Solid Earth, 107(B9), p. ESE 11-1-ESE 11-10. doi: 10.1029/2001JB000153.
- Gilbert, F. (1970) 'Excitation of the Normal Modes of the Earth by Earthquake Sources', Geophysical Journal of the Royal Astronomical Society, 22, pp. 223–226. doi: 10.1111/j.1365-246X.1971.tb03593.x.
- Goldreich, P. and Keeley, D. A. (1977) 'Solar seismology. II The stochastic excitation of the solar p-modes by turbulent convection', *The Astrophysical Journal*, 212, p. 243. doi: 10.1086/155043.
- Gualtieri, L. *et al.* (2013) 'Modelling secondary microseismic noise by normal mode summation', *Geophysical Journal International*, 193(3), pp. 1732–1745. doi: 10.1093/gji/ggt090.

- Hasselmann, K. (1963) 'A statistical analysis of the generation of microseisms', *Rev. of Geophys.*, 1(2), pp. 177–210.
- Herron, T. J., Tolstoy, I. and Kraft, D. W. (1969) 'Atmospheric pressure background fluctuations in the mesoscale range', *Journal of Geophysical Research*. Wiley-Blackwell, 74(6), pp. 1321–1329. doi: 10.1029/JB074i006p01321.
- Jorgensen, D. F. (1984) 'Mesoscale and Convective-Scale Characteristics of Mature

 Hurricanes. Part I: General Observations by Research Aircraft', *Journal of the Atmospheric Sciences*, pp. 1268–1286. doi: 10.1175/15200469(1984)041<1268:MACSCO>2.0.CO;2.
- Jorgensen, D. P. *et al.* (1985) 'Vertical Motions in Intense Hurricanes', *Journal of the Atmospheric Sciences*, pp. 839–856. doi: 10.1175/1520-0469(1985)042<0839:VMIIH>2.0.CO;2.
- Kobayashi, N. and Nishida, K. (1998) 'Continuous excitation of planetary free oscillations by atmospheric disturbances', *Nature*, 395(6700), pp. 357–360. doi: 10.1038/26427.
- Lee, W. D. *et al.* (2012) 'Typhoon-generated microseisms observed from the short-period KSRS array', *Geosciences Journal*, 16(4), pp. 447–454. doi: 10.1007/s12303-012-0039-y.
- Longuet-Higgins, M. S. (1950) 'A Theory of the Origin of Microseisms', *Philosophical Transactions of the Royal Society A: Mathematical, Physical and Engineering Sciences*, 243(857), pp. 1–35. doi: 10.1098/rsta.1950.0012.
- McDonald, J. A., Douze, E. J. and Herrin, E. (1971) 'The Structure of Atmospheric

- Turbulence and its Application to the Design of Pipe Arrays', *Geophysical Journal of the Royal Astronomical Society*, 26(1–4), pp. 99–109. doi: 10.1111/j.1365-246X.1971.tb03385.x.
- Nishida, K. *et al.* (2005) 'Array observation of background atmospheric waves in the seismic band from 1 mHz to 0.5 Hz', *Geophysical Journal International*, 162(3), pp. 824–840. doi: 10.1111/j.1365-246X.2005.02677.x.
- Orville, H. T. and Gutenberg, B. (1946) 'The use of microseisms in hurricane detection', *Eos, Transactions American Geophysical Union*, 27(1), pp. 111–117. doi: 10.1029/TR027i001p00111.
- Riehl, H. (1950) 'A model of hurricane formation', *Journal of Applied Physics*, 21(9), pp. 917–925. doi: 10.1063/1.1699784.
- Tanimoto, T. (1999) 'Excitation of normal modes by atmospheric turbulence: Source of long period seismic noise', *Geophys. J. Int.*, 136, pp. 395–402. doi: 10.1046/j.1365-246X.1999.00763.x.
- Tanimoto, T. (2005) 'The oceanic excitation hypothesis for the continuous oscillations of the Earth', *Geophysical Journal International*, 160(1), pp. 276–288. doi: 10.1111/j.1365-246X.2004.02484.x.
- Tanimoto, T. (2013) 'Excitation of microseisms: Views from the normal-mode approach', Geophysical Journal International, 194(3), pp. 1755–1759. doi: 10.1093/gji/ggt185.
- Tanimoto, T. and Lamontagne, A. (2014) 'Temporal and spatial evolution of an on-land hurricane observed by seismic data', *Geophysical Research Letters*. Wiley-

- Blackwell, 41(21), pp. 7532–7538. doi: 10.1002/2014GL061934.
- Tanimoto, T. and Um, J. (1999) 'Cause of continuous oscillations of the Earth', *Journal of Geophysical Research: Solid Earth*. Wiley-Blackwell, 104(B12), pp. 28723–28739. doi: 10.1029/1999JB900252.
- Watada, S. *et al.* (2006) 'Atmospheric pressure change associated with the 2003 Tokachi-Oki earthquake', *Geophysical Research Letters*, 33(24), pp. 1–5. doi: 10.1029/2006GL027967.
- Webb, S. C. (2007) 'The Earth's "hum" is driven by ocean waves over the continental shelves', *Nature*, 445(7129), pp. 754–756. doi: 10.1038/nature05536.
- Webb, S. C. (2008) 'The earth's hum: The excitation of earth normal modes by ocean waves', *Geophysical Journal International*, 174(2), pp. 542–566. doi: 10.1111/j.1365-246X.2008.03801.x.
- Zhang, J., Gerstoft, P. and Bromirski, P. D. (2010) 'Pelagic and coastal sources of P-wave microseisms: Generation under tropical cyclones', *Geophysical Research Letters*, 37(15), pp. 1–6. doi: 10.1029/2010GL044288.

3. Existence of the Threshold Pressure for Seismic Excitation by

Atmospheric Disturbances

Except for minor changes, this chapter appeared essentially in this form in:

Tanimoto, T., and A. Valovcin (2016), Existence of the threshold pressure for seismic excitation by atmospheric disturbances, Geophys. Res. Lett., 43, doi:10.1002/2016GL070858

3.1. Introduction

How seismic signals are generated by the land-atmosphere interaction is an old question (Tanimoto, Heki and Artru-Lambin, 2015). It is a difficult question, mainly because of a lack of good, critical data sets. Good data in this case means a dense network of seismometers and barometers. We have noted that the Earthscope Transportable Array (TA hereafter) could provide unique data sets to address this question, although the principal purpose of TA was to improve our understanding of structure in the solid Earth. TA data became useful for the land-atmosphere interaction study after 2010, because high-quality barometers (SEED channel LDO) and infrasound sensors (SEED channel LDF) were added to this network (http://www.earthscope.org/science/observatories/usarray). We use the barometer data in this paper. Consistent results were obtained with the infrasound sensor data. Comparison between barometer and infrasound sensors is shown in Figure 3.7 (Appendix) to support this point. Another pressure sensor, the MEMS pressure sensor (channel LDM), turned out to be inadequate for the frequency range (0.01-0.02 Hz) of this study.

In this paper, we focus on data for two tropical cyclones, Hurricane Isaac (2012) and Tropical Storm Lee (2011) that moved through the TA after their landfalls. Seismic and barometric data from these cyclones provide us unusual opportunities to observe the response of solid Earth generated by surface atmospheric pressure. Seismic ground motions and surface pressures varied 4-5 orders of magnitude in PSD as these hurricanes passed by.

We performed some analyses on Hurricane Isaac (Tanimoto and Lamontagne, 2014; Tanimoto and Valovcin, 2015) but in this paper we apply a different approach in order to understand some basic characteristics in the land-atmosphere interactions. In this paper, we only examine the co-located barometer and seismometer data and monitor how they change. The underlying idea is that the largest effects of atmospheric pressure should show up most clearly in the co-located seismic sensors. Despite the simplicity in this approach, we find quite interesting features in the relationships between surface pressure and ground motions. The most important point is the identification of the critical, threshold pressure; below this pressure, vertical ground motions are constant which means that seismic amplitudes are independent of changes in local atmospheric pressure. Above this pressure, ground motions increase with pressure. It shows that there exists a threshold atmospheric pressure, above which atmospheric pressure overwhelms other sources of seismic noise.

We will describe the data and our approach in section 2, three main characteristics in data in section 3 and our interpretations in section 4.

3.2. Data and Approach

Figure 3.1 shows the tracks of Hurricane Isaac and Tropical Storm Lee in the top panels. Red circles in top panels show the locations of stations (TA and some permanent stations) that had both seismometer and barometer data. Blue circles are stations with seismometers only. Since barometers were installed starting in mid-2010, only the eastern half had barometers at the time of Lee (Figure 3.1, top-right).

Although the tracks of both tropical cyclones are near the edge of the TA, we could confirm that seismic amplitudes and pressure variations are consistent with (approximate) cylindrical symmetry, at least for available azimuths, and they decreased with distance from the centers. The bottom panels show examples for selected time intervals; we chose UTC 0800, August 29, 2012 for Isaac (Figure 3.1 bottom, left) and UTC 1000, September 3, 2011 for Lee (Figure 3.1 bottom, right). Each circle is an average PSD for frequencies between 0.01 and 0.02 Hz. Seismic velocity PSDs are shown in blue with scale on the left and pressure PSDs are shown in red with scale on the right.

Figure 3.1 shows only vertical-component seismic data (bottom panels). For comparison, we show Figure 3.2 that shows amplitude-distance variations of three component seismic data (0.01-0.02 Hz) at UTC 1200, August 29, 2012, for Isaac. Similar amplitude decay trends are seen for all components but horizontal data contain much larger scatter.

Two bottom panels in Figure 3.1 show that the influence zone of hurricanes is mostly within 1000 km from their centers, with particularly large effects confined to the innermost 500 km. Some deviations to this statement can be recognized outside 1000 km as there is a secondary peak of pressure about 1500 km (Figure 3.1, bottom panels). Associated seismic amplitudes to these pressure variations are quite small and remain within the scatter of short-distance (<1000 km) data (Figure 3.3). We believe these secondary peaks around 1500 km were caused by spiral winds and rain bands that extend outward from the central region. But

since they do not bring much information on the land-atmosphere interaction, as evidenced in Figure 3.3, we focus our analysis on data within 1000 km from the cyclone centers.

3.3. Pressure PSD vs. Ground Velocity PSD

Figure 3.4 shows plots of surface pressure PSD (horizontal axis) vs. ground velocity PSD (vertical axis). Three-component ground velocity PSDs are indicated by three colors, vertical (Z) in blue, radial (R) in red and transverse (T) in black. Radial and transverse components were obtained by using the locations of the center of Isaac and Lee, reported in Brown (2011) for Lee and Berg (2013) for Isaac respectively.

Each point in Figure 3.4 represents PSDs computed for a time-series length of 1 hour. The entire time interval of data that was used to create Figure 3.4 was three days (August 29-31, 2012 for Isaac and September 3-5, 2011 for Lee).

Vertical-component data (blue) and horizontal-component data (red and black) make two separate clusters in Figure 3.4 when plotted against surface pressure from the co-located barometers. Horizontal-component PSDs are typically larger than vertical-component PSDs by about 2-3 orders of magnitude. Green dash lines in Figure 3.4 were determined by the least squares, fitting the formula $log_{10}(S_V)=A\ log_{10}(S_P)+B$ for different pressure ranges. In this formula, S_V is the ground velocity PSD and S_P is the surface pressure PSD. The coefficients determined by this fitting process (A and B) are summarized in Table 3-1. In total, there are five independent lines in Figure 3.4 and Figure 3.5 and each line is denoted by its name (V_g , V_{L1} , V_{L2} , H_g and H_L).

Both vertical and horizontal data were fit separately below and above the threshold pressure (PSD) $S_P=10$ (Pa²s). This threshold pressure was first chosen from vertical-component data that show clear a break in the data. We overlay the vertical PSDs from two cyclones in Figure 3.5 (top). Because Isaac was much stronger than Lee, we can see more points in higher pressure ranges for Isaac but the threshold pressure seems to agree between the two cyclones.

By fitting data from both cyclones above $S_P=10$, the dash line denoted by V_g was obtained. For the vertical-component data below this threshold value, we obtained V_{L2} . The latter is constant as the coefficient A was set to zero. There is a slight difference on this constant value between Isaac and Lee. In order to indicate this difference, we denote the value for Isaac by V_{L1} (Table 3-1) but it is not significantly different from V_{L2} that was determined from the combined vertical-component data. But this difference indicates that the background noise level, created by other noise sources, varies seasonally and sometimes year to year. If we took into account the differences between these flat noise levels from two cyclones, the threshold value ($S_P=10$) can vary from $S_P=5$ to 20 approximately.

Existence of a threshold value is not so obvious in horizontal-component data in Figure 3.4. It is partly because an overall trend in horizontal data shows a large gradient for the entire pressure range (Figure 3.4 and Figure 3.5). We believe this overall trend in gradient is caused by the well-known ground tilt. Tilt causes the same effect with horizontal acceleration and is particularly large in low-frequency bands below 0.02 Hz (Rodgers, 1968; Farrell, 1969; Aki and Richards, 2002).

There is an additional feature in horizontal data; if we overlay data from two tropical cyclones (Figure 3.5, bottom), there is a hint that the gradient becomes steeper as pressure increases. The least squares fits below and above $S_P=10$ (lines H_g and H_L) clearly show a steepening trend in gradient. Although we used two lines to fit horizontal data in Figure 3, in terms of underlying physical processes, it is hard to imagine a threshold pressure for horizontal data that causes a sudden change. We interpret that this gradient increase occurs gradually.

But why does the gradient in horizontal data increase with pressure? We speculate that there exists a direct wind effect for high pressure ranges. In general, pressure fluctuation for a frequency range 0.01-0.02 Hz is controlled by winds and is nearly proportional to the square of wind velocity. Therefore, some effects of wind are already included in pressure changes. But when the wind becomes strong, it can exert forces directly on nearby trees and observational facilities and generate additional ground tilt. This should be in addition to surface pressure changes and thus could be a cause for an increase in gradients in Figure 3.5. However, this is a speculation and details are hard to verify with current data sets.

In Figure 3.6, we show similar seismic amplitudes vs. pressure plot for Tropical Storm Lee for four different frequencies, 0.01-0.02 Hz (top left), 0.04-0.05 Hz (top right), 0.09-0.10 Hz (bottom left) and 0.14-0.15 Hz (bottom, right). Amplitude differences between horizontal-component data and vertical-component data are the largest for 0.01-0.02 Hz and quite large for 0.04-0.05 Hz. Both panels at top show that horizontal amplitudes increase with pressure amplitudes (PSD). The differences in vertical and horizontal amplitudes

decrease in higher frequency plots and the correlation between horizontal amplitudes and pressure amplitudes also becomes smaller. In the panel for 0.09-0.10 Hz, there may still be a weak correlation for pressure above 1-10 (Pa²s) but in the 0.14-0.15 Hz plot, seismic amplitudes change little with local surface pressure. Clearly the dominance of local atmospheric effects is confined to low frequencies below about 0.05 Hz. It should also be noted that these higher-frequency signals in the bottom panels are mostly the secondary microseism (seismic noise) that are generated in the oceans (Longuet-Higgins, 1950; Hasselmann, 1963).

3.4. Discussion and Summary

One of the most robust features in our observation is the existence of a threshold pressure in vertical-component data at a pressure PSD of about $S_P=10$ (Pa^2s). Because of scatter in data, this value contains some uncertainties and can vary from $S_P=5$ to 20. Below this threshold pressure, vertical amplitudes do not change with pressure. This lack of correlation means that the local atmospheric pressure is not the main source of seismic ground motion (noise) at the site. These signals below the threshold pressure were generated by processes other than the local atmospheric pressure, such as ocean waves away from the station. The threshold pressure can be viewed as the pressure when the effects of the local atmospheric pressure exceed those of other seismic-noise sources. In order to understand the land-atmosphere interaction in more details, we must focus on the pressure range above this threshold.

We take a view that atmospheric pressure acts as an excitation source at Earth's surface for seismic waves. In the whole, coupled Earth system, this view may not apply if phase velocity of atmospheric waves were close to phase velocity of seismic waves in the solid Earth as the transmission of waves become very efficient between the atmosphere and the solid Earth. But such a match in phase velocity is not likely to occur as atmospheric waves have velocities of a few hundred meters per second and seismic waves have velocities of 3-4 km/s for surface waves and faster body waves. It was pointed out previously (Sorrells, 1971; Sorrells and Goforth, 1973) that atmospheric pressure acts almost as a surface load under such a condition. Seismic data show such amplitude behaviors to first order, although they should also contain some smaller-amplitude propagating surface waves. But those seismic data are in the near-field and seem to be dominated by pressure loading effects.

The proportionality constant (A in the log-log formula) between S_V and S_P in Figure 2 (and 3) is not 1 above the threshold pressure. Instead, it is about 1.5 (V_g in Table 1). We interpret this observation as follows; the excitation of seismic ground motion by atmospheric pressure occurs by a force that can be considered to be a random force. This is because atmospheric pressure has very short correlation distance on Earth's surface (about 100 m or less). It changes its sign with short wavelengths of the order of 10-100 m (e.g. Herron, Tolstoy and Kraft, 1969; McDonald, Douze and Herrin, 1971). On the other hand, the pressure source is spread out over many kilometers. In essence, we have a rapidly fluctuating source that extends over a large area. In such a case, one can approximate that the excited seismic ground motion PSDs become proportional to pressure PSD by $S_v \propto L^2 S_p$

where L is the correlation length in the surface pressure field (Kobayashi and Nishida, 1998; Fukao *et al.*, 2002; Tanimoto, 2005; Tanimoto and Valovcin, 2015). In such a model, if the correlation length L is proportional to $S_p^{0.25}$, the gradient of 1.5 can be explained. This means that the correlation length changes with pressure. Physically, one would expect that larger pressure is related to stronger wind. If strong lateral wind exists, one can imagine that the correlation length in the surface pressure field should become larger as pressure at a location can be transported to nearby location by winds. However, why the exponent becomes 0.25 is left unexplained. Understanding it requires a careful theoretical study.

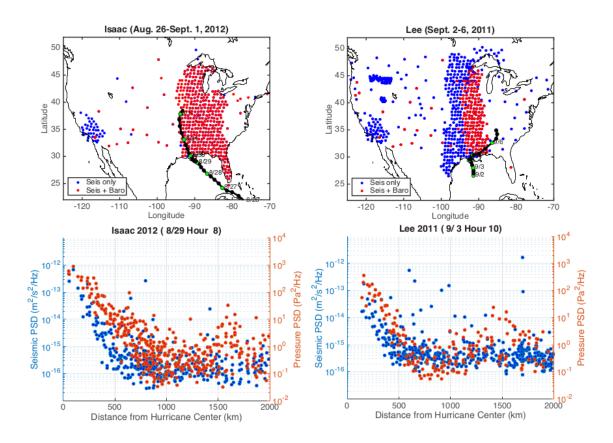


Figure 3.1: (top left) Track of Hurricane Isaac (August 2012) and seismic stations from EarthScope. The black circles are the locations of its center at every 6 h. The green circles indicate the midnight of each day. The red circles indicate the stations that had barometer and seismometer. The blue circles indicate the stations with seismometer only. (top right) Track of Tropical Cyclone Lee (September 2011). (bottom left) Seismic vertical PSD and pressure PSD plotted against distance from the center of Isaac. (bottom right) Seismic vertical PSDs and pressure PSDs for Lee.

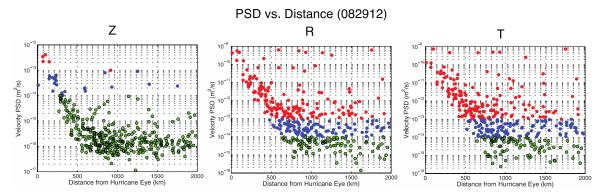


Figure 3.2: An example for the amplitude (PSD) – distance plot for three component seismic data. These results are for UTC 12:00, August 29, 2012. Colors indicate the range of amplitudes, red circles for larger than 10-12, blue between 10-14 and 10-12 and green for less than 10-14. Amplitudes for horizontal components (R: radial, T:transverse) are much higher and contain larger scatter than vertical component. Decreasing trend with distance from the center is seen for all three components. R and T are with respect to the hurricane center.

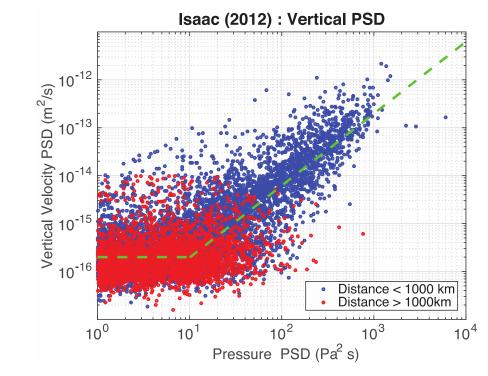


Figure 3.3: Comparison of vertical PSD of Isaac for stations closer than 1000 km from the center (blue) and for stations beyond 1000 km (red). Although there exist some stations beyond 1000 km (red points) that have pressure PSD of 100 (Pa2s), they are still within the scatter of data and do not deviate from the trend that blue data points make.

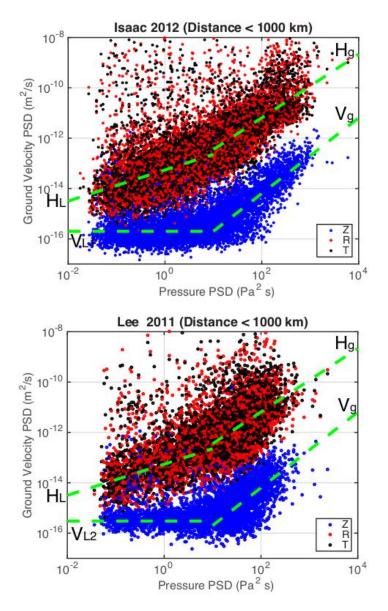


Figure 3.4: Seismic amplitudes (PSD) plotted against pressure PSD for every 1-hour interval. Top is for Hurricane Isaac and bottom is for Tropical Storm Lee. Vertical PSDs are denoted by blue circles, radial by red and transverse by black. Lines by the least-squares fit are shown by green dashes. Except for V_{L1} , they were derived from the combined data set for Isaac and Lee. Hg is for horizontal component data above the threshold value $S_P=10$. H_L is for horizontal component data below this threshold pressure. V_g is for vertical component data above the threshold pressure, determined from the combined data from both tropical cyclones. V_{L1} is for below the threshold for Isaac only. V_{L2} is for the combined data of Isaac and Lee. The coefficients are in Table 1.

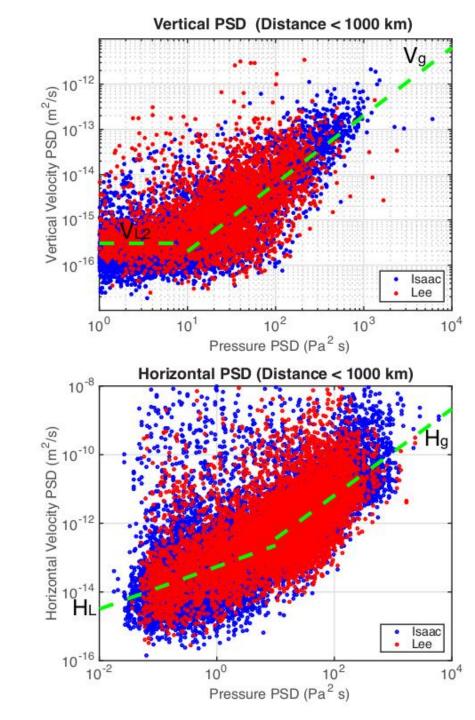


Figure 3.5: Same data as in Figure 3.4 but the data from Isaac and Lee were overlaid. Top is the vertical component data and bottom is the horizontal component data. Lines are the same with those in Figure 3.4.

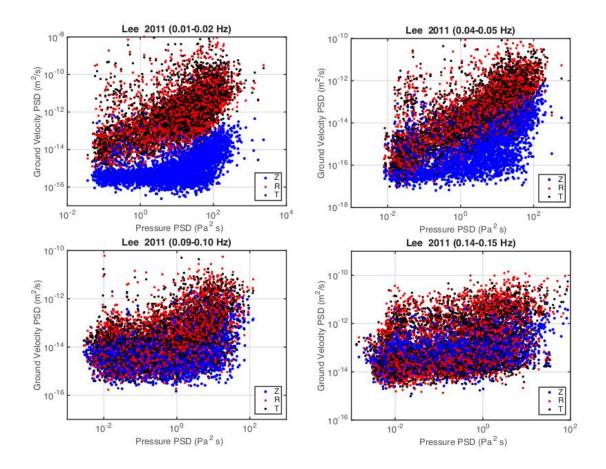


Figure 3.6: Seismic amplitudes (PSD) vs. pressure PSD for four frequency ranges, 0.01-0.02 Hz (top, left), 0.04-0.05 Hz (top, right), 0.09-0.10 Hz (bottom, left) and 0.14-0.15 Hz (bottom, right). Because of tilt, horizontal component data have much larger amplitudes than vertical component data for lower frequency ranges (0.01-0.02 and 0.04-0.05 Hz) and have good correlation with local pressure data. In higher frequency ranges (0.09-0.10 and 0.14-0.15 Hz), tilt effects are much smaller and vertical and horizontal components have similar amplitudes. In the 0.14-0.15 Hz plot, signals are generated in.

Table 3-1: Least Squares Fit by the Formula log10(SV) = A log10(SP) + B for Various Ranges^a IDs are the same as in Figures 2–4. Ranges of barometer (pressure) PSD are in the second column. VL1 is for Isaac only, but all others were derived for the combined data of Isaac and Lee

ID	Range (S _P)	A	В
V_{g}	$S_P > 10$	1.501±0.001	-17.20±0.08
V_{L1}	$S_{P} < 10$	0.0	-15.70±0.02
V_{L2}	$S_{P} < 10$	0.0	-15.52±0.02
H_{g}	$S_{P} > 10$	1.261±0.020	-13.71±0.02
H_{L}	$S_{P} < 10$	0.618±0.031	-13.26±0.30

3.5. Appendix

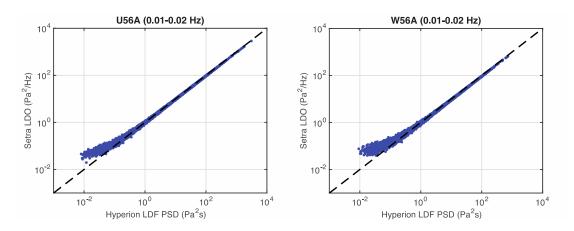


Figure 3.7: For many one-hour time series throughout 2014, for two stations U56A and W56A, pressure PSD (average between 0.01 and 0.02 Hz) were computed for barometer data (sensor Setra 278) and infrasound data (sensor Hyperion). Dash lines indicate that PSD amplitudes are equal between two instruments. They are consistent down to about 0.1 Pa²s below which the low resolution limit seems to be reached for Setra 278.

3.6. References

Aki, K. and Richards, P. G. (2002) *Quantitative seismology*. University Science Books.

Available at:

https://www.researchgate.net/publication/215755941_Quantitative_Seismology

- (Accessed: 3 May 2018).
- Berg, R. (2013) 'Tropical Cyclone Report: Hurricane Isaac (AL092012) 21 August 1
 September 2012'. Miami, FL: NOAA/National Weather Service.
- Brown, D. P. (2011) 'Tropical Cyclone Report: Tropical Storm Lee (AL132011) 2-5 September 2011'. Miami, FL: NOAA/National Weather Service.
- Farrell, W. E. (1969) 'A gyroscopic seismometer: Measurements during the borrego earthquake', *Bulletin of the Seismological Society of America*. Bulletin of the Seismological Society of America, 59(3), pp. 1239–1245. Available at: https://pubs.geoscienceworld.org/ssa/bssa/article/59/3/1239/101572/a-gyroscopic-seismometer-measurements-during-the (Accessed: 7 May 2018).
- Fukao, Y. et al. (2002) 'A theory of the Earth's background free oscillations', Journal of Geophysical Research: Solid Earth, 107(B9), p. ESE 11-1-ESE 11-10. doi: 10.1029/2001JB000153.
- Hasselmann, K. (1963) 'A statistical analysis of the generation of microseisms', *Rev. of Geophys.*, 1(2), pp. 177–210.
- Herron, T. J., Tolstoy, I. and Kraft, D. W. (1969) 'Atmospheric pressure background fluctuations in the mesoscale range', *Journal of Geophysical Research*. Wiley-Blackwell, 74(6), pp. 1321–1329. doi: 10.1029/JB074i006p01321.
- Kobayashi, N. and Nishida, K. (1998) 'Continuous excitation of planetary free oscillations by atmospheric disturbances', *Nature*, 395(6700), pp. 357–360. doi: 10.1038/26427.
- Longuet-Higgins, M. S. (1950) 'A Theory of the Origin of Microseisms', *Philosophical*

- Transactions of the Royal Society A: Mathematical, Physical and Engineering Sciences, 243(857), pp. 1–35. doi: 10.1098/rsta.1950.0012.
- McDonald, J. A., Douze, E. J. and Herrin, E. (1971) 'The Structure of Atmospheric

 Turbulence and its Application to the Design of Pipe Arrays', *Geophysical Journal*of the Royal Astronomical Society, 26(1–4), pp. 99–109. doi: 10.1111/j.1365246X.1971.tb03385.x.
- Rodgers, P. W. (1968) 'The response of the horizontal pendulum seismometer to Rayleigh and Love waves, tilt, and free oscillations of the earth', *Bulletin of the Seismological Society of America*, 58(5), pp. 1385–1406. Available at: http://www.bssaonline.org/cgi/content/abstract/58/5/1385.
- Sorrells, G. G. (1971) 'A Preliminary Investigation into the Relationship between Long-Period Seismic Noise and Local Fluctuations in the Atmospheric Pressure Field', *Geophysical Journal of the Royal Astronomical Society*, 26(1–4), pp. 71–82. doi: 10.1111/j.1365-246X.1971.tb03383.x.
- Sorrells, G. G. and Goforth, T. T. (1973) 'LOW-FREQUENCY EARTH MOTION

 GENERATED BY SLOWLY PROPAGATING PARTIALLY ORGANIZED

 PRESSURE FIELDS', Bulletin of the Seismological Society of America, 63(5), pp. 1583–1601.
- Tanimoto, T. (2005) 'The oceanic excitation hypothesis for the continuous oscillations of the Earth', *Geophysical Journal International*, 160(1), pp. 276–288. doi: 10.1111/j.1365-246X.2004.02484.x.

- Tanimoto, T., Heki, K. and Artru-Lambin, J. (2015) 'Interaction of Solid Earth, Atmosphere, and Ionosphere', in *Treatise on Geophysics: Second Edition*, pp. 421–443. doi: 10.1016/B978-0-444-53802-4.00083-X.
- Tanimoto, T. and Lamontagne, A. (2014) 'Temporal and spatial evolution of an on-land hurricane observed by seismic data', *Geophysical Research Letters*. Wiley-Blackwell, 41(21), pp. 7532–7538. doi: 10.1002/2014GL061934.
- Tanimoto, T. and Valovcin, A. (2015) 'Stochastic excitation of seismic waves by a hurricane', *Journal of Geophysical Research : Solid Earth*, 120, pp. 7713–7728. doi: 10

4. Modeling the excitation of seismic waves by the Joplin tornado

Except for minor additions, this chapter appeared essentially in this form in:

Valovcin, A., & Tanimoto, T. (2017). Modeling the excitation of seismic waves by the Joplin tornado. Geophysical Research Letters, 44. https://doi.org/10.1002/2017GL074185

4.1. Introduction

Tornadoes are among the most common natural disasters in the United States. Various methods are currently used to forecast tornadoes, including surface weather stations and incoherent scatter and Doppler radar (Mitchell *et al.*, 1998). These methods can successfully detect the possible locations of tornadoes and funnel clouds. However, determining the timing of a tornado touchdown still strongly relies on reports from storm chasers and spotters. Other studies have shown that tornadoes generate characteristic seismic and infrasound signals when they have touched down, providing a possible alternative detection method (Tatom, Knupp and Vitton, 1995; Tatom and Vitton, 2001; Ingel, 2004; Talmadge C. & Waxler R., 2016).

The purposes of this study are: (1) to examine the seismic excitation mechanism of tornadoes; and (2) to test whether a seismic approach can provide a new method to evaluate the size of tornadoes. To test these ideas, we use data from the Earthscope Transportable Array (TA), a network of co-located seismometers and barometers. Some of the stations in this network have recorded signals from tornadoes that passed within a 10km radius (Tytell *et al.*, 2016). We seek a seismic approach to evaluate the tornado strength through waveform modeling of the seismic signals generated by the tornado.

In this paper, we focus on the signals generated by the May, 2011 Joplin Tornado. The seismic and barometric data recorded during this tornado provide an opportunity to study the excitation of the seismic waves when it has touched down. We report our results for a low-frequency band (between 0.01 and 0.03 Hz) because we can match waveforms

well for this range. We show the existence of a relationship between the recorded strength of the storm and the amplitude of the observed seismic data.

We describe our data on the Joplin tornado in section 2, our method in section 3, the main results in section 4 and our interpretations in section 5.

4.2. The Joplin Tornado

On May 22, 2011, an Enhanced Fujita Scale 5 (EF5) tornado passed through the town of Joplin, Missouri. An EF5 tornado is the most strongly rated intensity on the EF scale, exhibiting wind gusts over 200 mph (http://www.spc.noaa.gov/efscale/). The tornado touched down at 22:34 UTC southwest of Joplin and traveled for 22.1 miles with a maximum width of 23:12 1 mile before lifting off at UTC (http://www.weather.gov/sgf/news_events_2011may22). A map of its path is shown in Figure 4.1, with locations and intensities taken from the National Weather Service. The tornado passed within 3km of one station in the TA, T38A, as seen in Figure 4.1 (right). This station recorded both seismic and pressure data for the event.

We are limited to the use of this one station because the tornado-generated seismic signals do not appear to propagate much further than 25km from the source. Figure 4.3 (left) shows a comparison between the vertical seismic data recorded at the five stations closest to the track of the tornado. The locations of these stations are shown in Figure 4.1 (right). The black dashed lines in Figure 4.3 indicate the times of tornado touchdown and liftoff. Between these times, when the tornado was in contact with the ground, high amplitude signals are evident in the recording at T38A, whereas, the other four stations show no such

signal. We attribute the high amplitude signals found at T38A to the seismic waves generated by the Joplin tornado after coming into contact with the ground. We also find that the high amplitude signals indicative of tornado generation are most prevalent between 0.01-0.03 Hz. Higher frequencies do not show this large amplitude signal during the event, as shown in Figure 4.2, which includes the seismic signals at 0.09-0.11 Hz and 9-11Hz for comparison.

4.3. Methods

Figure 4.3 (right) shows the filtered vertical seismic trace (0.01-0.03 Hz) on top (blue line) and the filtered barometric data for the same frequency band in the middle (red line). Time origin for the data is 21:00 UTC. The waveforms of the vertical component and those of the pressure are quite different; the large-amplitude pressure phase arrived after 7000 sec while the vertical component signal (top trace) started almost immediately after the Joplin tornado touched the ground (left dashed line). We also note that the seismic and pressure waveforms match closely phase-to-phase, especially after the liftoff of the tornado. This indicates that the vertical component seismic data contain both signals from the ground (seismic signals) and also from the air (air-wave signals).

Since we are interested in modeling seismic signals that propagated through the ground, we remove air-wave related signals in the seismic data. Using the data after the liftoff (the vertical dash on the right in Figure 4.3), we obtain the proportionality constant between vertical seismic data and pressure data. We then use this constant to correct for the pressure (air-wave) signals and subtract the surface pressure effect from the vertical seismic

trace. We interpret the higher amplitude vertical seismic signals that occur towards the end of the tornado lifespan following liftoff as high amplitude pressure signals.

This high amplitude pressure is likely being caused by fluctuations in atmospheric pressure in the region surrounding the tornado due to air turbulence, high winds, and other local storm effects. Previous studies have shown that atmospheric pressure does in fact excite seismic waves (Sorrells, 1971; Sorrells and Goforth, 1973; Tanimoto and Valovcin, 2016). It is likely that there are many local pressure fluctuations in the region at this time, for that is when the tornado's path brings it closest to the station. It is therefore possible that the tornado affects the local air pressure variations, which contributes to seismic signals in the vertical component. When a tornado touches down, it is met with a large amount of friction, and the energy used to overcome this friction, as well as energy from turbulent pressure fluctuations within the funnel of the tornado, is transferred into the ground. This energy is then converted to seismic and thermal energy (Tatom, Knupp and Vitton, 1995; Tatom and Vitton, 2001). We want to isolate these signals coming from the ground generated directly by the tornado, not signals that are coming from other turbulent fluctuations in air pressure surrounding it. Thus, we subtract the recorded pressure signal from the vertical seismic data using the previously mentioned proportionality constant to get the corrected vertical data, shown as the third trace in Figure 4.3 (right).

Because a tornado is a moving seismic source applying force to the ground, we approximate it as many individual sources along the path that will add up to be the observed signal. We interpolate possible source locations along the observed path of the Joplin

tornado, spaced 5 seconds apart, resulting in 457 sources between when the tornado touched down and when it lifted off 38 minutes later. Tornado timing and location information for use in the interpolation was taken from the National Weather Service and a local news station (http://www.news9.com/category/239687/joplin-tornado-timeline-interactive). The interpolated locations are spaced equally temporally (every 5 seconds) between the known reported locations of the tornado that also had timing information. The path is shown in Figure 4.4, where the interpolated locations are shown as the blue circles and the black stars are the known locations with times used for the calculation. Because we low-pass filter the seismic data (0.01-0.03 Hz), we believe this sampling interval (5 sec) is justified. For the analysis of higher frequency data, sampling in the time domain may have to be at smaller intervals.

We approximate the source as vertical forces because a tornado contains a low-pressure vertical core at its center inside a funnel of rapidly spinning air. There might also be some rotational motion in the source due to the vorticity but the main effect comes from the vertical pressure difference when the tornado touches the ground. For a complete analysis of three-component seismic data, a more complex source model may be required to analyze seismic data.

At each source location, we generate a Green's Function (GF) using a vertical triangular pulse force (from a publicly available program by O. Coutant, https://isterre.fr/) and the local Missouri velocity model from the Central U.S. Seismic Velocity Model (Herrmann and Ammon, 1997). We ignored the effects of local topography for this study.

Due to some limitations of the GF program, the source and the receiver cannot be at the same depth, so to account for this, we placed the receiver at shallow depth, on the order of meters. We do not believe that this would largely affect the results. Each GF is created using the same parameters for the triangular pulse source amplitude. We filter these synthetic signals to 0.01-0.03 Hz to match the frequency band within which we observed the tornado signals.

To solve for the amplitude of each synthetic seismogram (GF), we perform a least squares inversion. Our equation relating the recorded data, the source amplitudes and the synthetic seismograms is of the form:

$$d_j = \sum_{i=1}^N s_i G_{ij} \tag{1}$$

where the pressure-corrected digitized velocity seismogram is $d_j = d(t_j)$, (j = 1,2,3...), s_i are the source amplitudes in Newtons, G_{ij} are the synthetic seismograms by surface vertical forces (GFs) and N is the number of sources that we generated over the tornado path. Using a linear least squares equation of the form d = Gs and solving for s we get:

$$\mathbf{s} = (\mathbf{G}^T \mathbf{G} + \varepsilon^2 \mathbf{I})^{-1} \mathbf{G}^T \mathbf{d} \tag{2}$$

where $d = (d_1, d_2, d_3 ...)$ and we use a constant damping parameter ε^2 on the diagonal elements. By performing this inversion with various damping parameters, we seek a good fit to the pressure-corrected vertical seismic data and obtained source amplitudes over the duration of the tornado.

4.4. Results

The results from the inversion are shown in Figure 4.5. The top panel shows the solutions for source strength amplitude (s in equation 2) as it varies over the lifespan of the tornado, using three different values for ε^2 which give variance reductions (VR) in the fit of 99% (blue), 93% (red) and 87% (green). The bottom panel shows the fit for each solution compared to the pressure-corrected vertical seismic data (black line) obtained from the source amplitudes we solved for. The model fits the data for the duration of time that the tornado was in contact with the ground, except for a slight amplitude misfit. Choice of an alternative damping parameter does not change the overall characteristics of the solution and the fit.

For smaller damping parameters, we can create a much better fit to the black trace, shown in Figure 4.5 (bottom). However, the solution then makes the source strength much larger (see the blue line in Figure 4.5, top). We chose a damping parameter such that the fit between two traces start to deteriorate, which here is the fit with 93% VR.

4.5. Discussion

Figure 4.6 shows the comparison of our source amplitudes to the EF rating of the tornado at various times. These are the same source amplitudes from the 93% VR solution (red line) from Figure 4.5 (top). Overall, we find a good correlation; when the source amplitudes are largest, the tornado is reported as EF 4-5 (red shaded area) and when the source amplitudes are smallest, it is reported as EF 0-2 (blue shaded areas). It is also interesting to note how this relates to the amplitude of the seismogram over time. Although

the strength of the tornado and the amplitude of the seismic source is changing over time, the recorded seismogram remains relatively consistent in amplitude. This is explained by the location of the tornado relative to the receiver. While the tornado is growing weaker towards the end of its lifespan, it is also approaching the station. This results in the appearance that the seismic waves have remained fairly consistent in amplitude.

Overall, this analysis shows that it is possible to model the seismic signal that is generated by a tornado that has touched down and use it to evaluate the strength of the event. With our basic inversion we are able to fit the pressure-corrected vertical seismic data reasonably well.

Our results indicate that it may be possible to use seismic signals to evaluate the magnitude of tornadoes. However, it also clarified two constraints are needed in order to apply such a seismic approach. The first necessary constraint is the barometric pressure recorded during the storm, which ensures that the signals modeled are those coming from the ground rather than the atmosphere above. An array of seismic instruments alone would not allow a separation of seismic signals from atmospheric waves. Therefore, our approach requires co-located barometers and seismometers. If we could develop wave-simulation codes for a coupled atmosphere and solid earth medium, it may be possible to model the wavefields that contain both seismic waves and atmospheric waves. Such an approach would not require the barometric data in addition to the seismic and could increase the number of events able to be studied.

The second constraint is on the amplitudes of the signals. Since the amplitudes of the excited seismic signals are so small, the tornadoes must pass very close to the seismic stations. At this low frequency range (0.01-0.03 Hz) we are likely observing the near-field effects. To monitor tornadoes on a larger scale, we may need a much denser network of seismic stations, preferably co-located with barometer instruments.

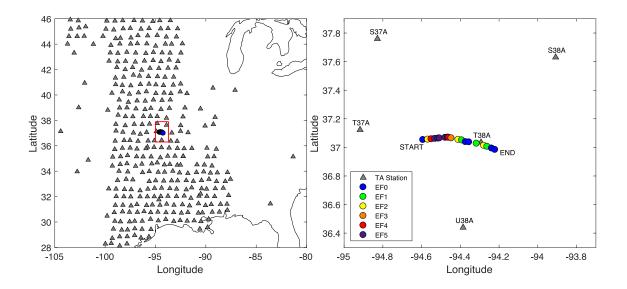


Figure 4.1: Map of stations locations (triangles) and the track of the Joplin tornado as it traveled through the Transportable Array (right panel from START to END). At each station, a seismometer and a barometer are co-located. Red box on left figure indicate the area shown in the right figure. Tornado locations and EF ratings from NOAA and NWS, are shown in colors, indicating the recorded intensity of this tornado on the EF scale.

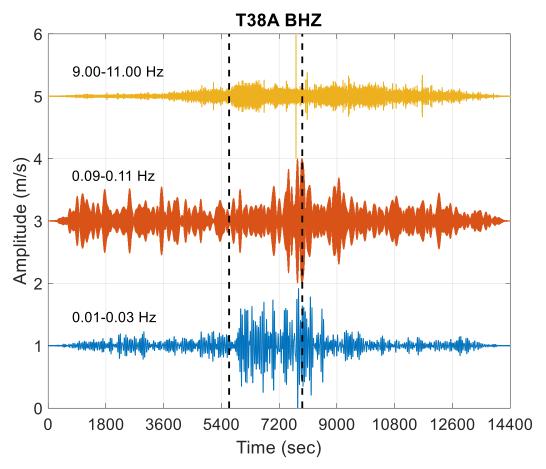


Figure 4.2: Seismic signal recorded at station T38Z at three frequency ranges: 0.01-0.03 Hz (blue trace), 0.09-0.11 Hz (orange trace) and 9-11 Hz (yellow trace). The trace at 0.01-0.03 Hz is the only one that clearly shows a higher amplitude signal during the time that the tornado was in contact with the ground (time between the black dashed lines).

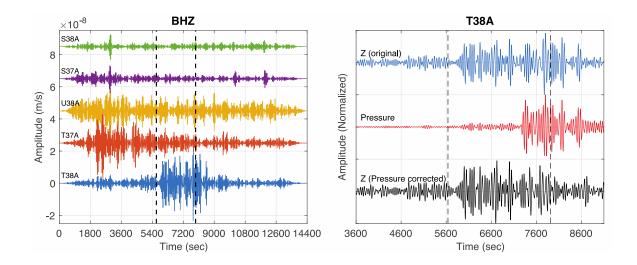


Figure 4.3: (left) The vertical seismic signal recorded at the five closest stations, showing that the signal generated by the tornado does not travel very far. The closest station, T38A, ranges from 2-24km from the tornado as it moves along its path, and is the only station with high amplitude signals recorded during the duration of the storm (between the black dashed line). (right) Vertical seismic data (blue) and barometric pressure (red) recorded at station T38A during the Joplin tornado. Black dashed vertical lines indicate the times of tornado touchdown and liftoff. The original vertical component seismogram (top) contains both airwaves and seismic waves. Airwaves are independently recorded by barometers in the second trace (red line) and are removed from the top seismogram by cross-correlation and subtraction. The subtracted vertical motion is the third (black) trace. This is the signal that propagated in the solid Earth.

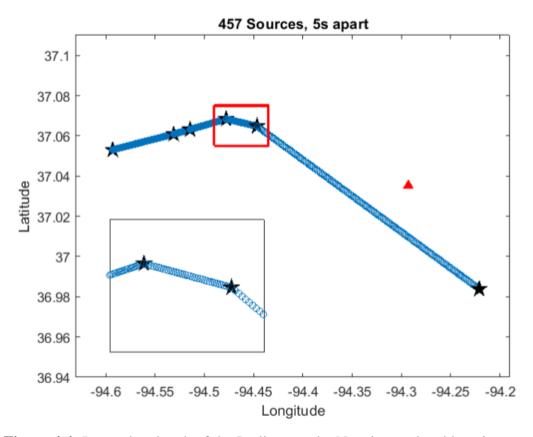


Figure 4.4: Interpolated path of the Joplin tornado. New interpolated locations are spaced 5 seconds apart (blue circles). The points given as black stars are the known locations with timing information that were used for the interpolation. Station T38A is given as the red triangle.

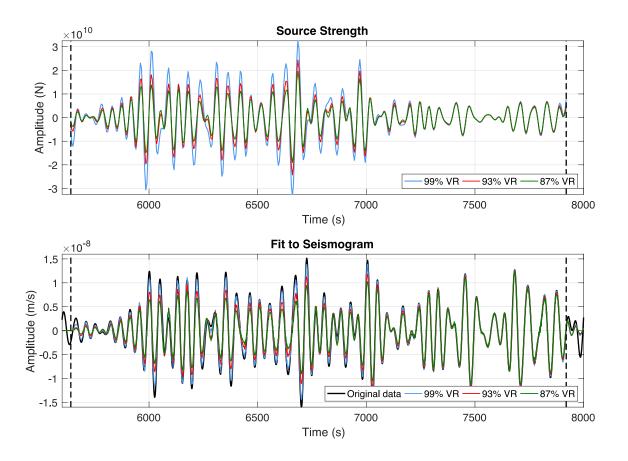


Figure 4.5: Results of the inversion for seismic source strength of the tornado. (top) The source strength amplitudes over time, as the tornado traveled along its path for three damping parameters, resulting in variance reductions in the fit of 99% (blue), 93% (red) and 87% (green). The source strength is quite high up to 7000 seconds in the plot. Black dashed lines indicated times of tornado touchdown and liftoff. (bottom) Comparison of the theoretical seismograms created for the derived source amplitude in the top panel to the actual recorded vertical seismic data (black). The model fits the data quite well, except for slight amplitude mismatch in earlier parts of seismogram (up to about 6700 sec).

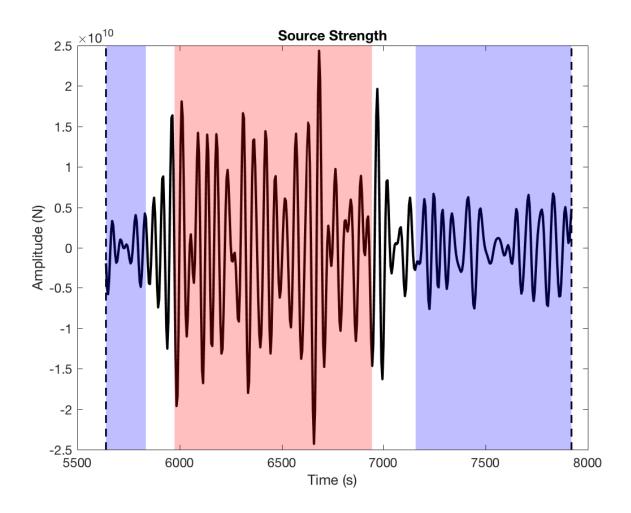


Figure 4.6: Comparison of source strength amplitude (derived from seismic data) to the actual recorded strength of the tornado (EF scale). The source strength amplitude is the same as the 93% VR solution in Figure 4.5 (top). The red highlighted section indicates when the Joplin tornado was recorded as EF4-5 intensity, and the blue highlighted sections are when the tornado was recorded as EF0-2. Clearly there is correlation between our seismic results and the EF scales reported for this tornado.

4.6. References

Herrmann, R. B. and Ammon, C. J. (1997) 'Faulting parameters of earthquakes in the New Madrid, Missouri, region', *Engineering Geology*. Elsevier, 46(3–4), pp. 299–311.

- doi: 10.1016/S0013-7952(97)00008-2.
- Ingel, L. K. (2004) 'An Effective Mechanism of Seismic Signal Generation during the Interaction of Tornadoes with the Earth' s Surface', 395(2), pp. 292–295.
- Mitchell, E. D. W. et al. (1998) 'The National Severe Storms Laboratory Tornado Detection Algorithm', Weather and Forecasting, 13(2), pp. 352–366. doi: 10.1175/1520-0434(1998)013<0352:TNSSLT>2.0.CO;2.
- Sorrells, G. G. (1971) 'A Preliminary Investigation into the Relationship between Long-Period Seismic Noise and Local Fluctuations in the Atmospheric Pressure Field', *Geophysical Journal of the Royal Astronomical Society*, 26(1–4), pp. 71–82. doi: 10.1111/j.1365-246X.1971.tb03383.x.
- Sorrells, G. G. and Goforth, T. T. (1973) 'LOW-FREQUENCY EARTH MOTION

 GENERATED BY SLOWLY PROPAGATING PARTIALLY ORGANIZED

 PRESSURE FIELDS', Bulletin of the Seismological Society of America, 63(5), pp. 1583–1601.
- Talmadge C. & Waxler R. (2016) 'Infrasound from Tornadoes: Theory, Measurement, and Prospects for Their Use in Early Warning Systems', *Acoustic Today, Acoustical Society of America*, 12(1), pp. 43–51.
- Tanimoto, T. and Valovcin, A. (2016) 'Existence of the threshold pressure for seismic excitation by atmospheric disturbances', *Geophysical Research Letters*. Wiley-Blackwell, 43(21), p. 11,202-11,208. doi: 10.1002/2016GL070858.
- Tatom, F. B., Knupp, K. R. and Vitton, S. J. (1995) 'Tornado Detection Based on Seismic

- Signal', Journal of Applied Meteorology, 34.
- Tatom, F. and Vitton, S. (2001) 'The Transfer of Energy from a Tornado into the Ground', Seismological Research Letters, 72(1), pp. 12–21. Available at: http://171.66.125.217/content/72/1/12.short.
- Tytell, J. et al. (2016) 'The USArray Transportable Array as a platform for weather observation and research', *Bulletin of the American Meteorological Society*, 97(4), pp. 603–619. doi: 10.1175/BAMS-D-14-00204.1.

5. Backprojection of Tropical Cyclones in the Atlantic

This chapter is in preparation for publication.

5.1. Introduction

Microseisms, the continuous oscillations of the Earth, are mostly associated with the frequencies generated by ocean waves. The different peak frequencies can be attributed to two generation mechanisms: (1) the primary microseisms, with periods from 10-20s, produced by coupling between ocean waves and the solid Earth in shallow environments (Hasselmann, 1963; Ardhuin *et al.*, 2011; Gualtieri *et al.*, 2018) and (2) the secondary microseisms, with periods less than 10s, produced by wave-wave interactions that occur near the ocean surface (Longuet-Higgins, 1950; Hasselmann, 1963).

In a similar manner to the generation of secondary microseisms, tropical cyclones (hurricanes and typhoons) are also thought to produce microseisms in this frequency range while they are over the ocean (Zhang, Gerstoft and Bromirski, 2010; Ardhuin *et al.*, 2011; Farra *et al.*, 2016; Gualtieri *et al.*, 2018). The strong winds from the storms excite higher amplitude ocean waves, which interact with each other and generate forcing equivalent to vertical forces (Longuet-Higgins, 1950). The goal of this study is to understand these processes in detail by examining many hurricane data, because being able to study them remotely while they are over the ocean has more potential for use in hazard monitoring, unlike previous studies where we examined hurricanes after they made landfall (Tanimoto and Lamontagne, 2014; Tanimoto and Valovcin, 2015, 2016).

In this paper we demonstrate how we can track a strong hurricane over the ocean through time using a beamforming method with a dense array and backprojecting seismic wave energy all the way back to the excitation sources. We show the detailed results of the

backprojection for Hurricane Sandy, followed by examples from a number of other tropical cyclones. We then examine the physical requirements for the backprojection to be successful as related to the size of the storms.

5.2. Data and Methods

For this study we used stations in the Southern California Seismic Network (SCSN) as shown in Figure 5.1: **Map of the stations in the Southern California Seismic Network.**, as well as a few select stations from Earthscope's Transportable Array (TA). The SCSN is an ideal network to examine P-wave microseism generation by tropical cyclones over the Atlantic as it is within the distances between 30 and 90 degrees and allows us to avoid the triplication effects from the upper mantle discontinuities (Dziewonski and Anderson, 1981; Kennett and Engdahl, 1991). Track data for 27 hurricanes between 2011 and 2017 was obtained from the National Weather Center's hurricane database (HURDAT). We will focus on the backprojection results from Hurricane Sandy (October, 2012) first but show the results from other hurricanes as well.

Previous studies have reported that ocean storms generate 1-10s period waves (Ardhuin *et al.*, 2011; Farra *et al.*, 2016; Gualtieri *et al.*, 2018), which we confirmed with stations in the Transportable Array. Figure 5.2 shows two spectrograms (time-frequency plots) for stations R58B and 060Z, located in Virginia and Florida. The vertical axes are frequency and the horizontal axes are days beginning on October 20, 2012. The color represents the amplitude of the power spectral densities of the vertical components in decibels; both spectra show a bright spot around 0.2 Hz when Hurricane Sandy passed near

them (at 6-8 days for 060Z and at 8-10 days for R58B) and confirmed that Hurricane Sandy was generating waves around 0.2Hz. Other stations along the coast showed this same feature.

We perform a backprojection of these 0.2 Hz P-waves using the SCSN and we focus on the vertical seismograph component (LHZ). For this backprojection we use a frequency-wavenumber (f-k) analysis, where at each station n the frequency spectra $F_n(\omega)$ for a given time-series are correlated and summed for a given wavevector \mathbf{k} . The Preliminary Earth Reference Model (PREM) is used in the ray-tracing part of the analysis, which maps the wavenumbers by using this velocity model to calculate the takeoff angles and arclength of the ray paths (Dziewonski and Anderson, 1981). The wavevector (\mathbf{k}_x , \mathbf{k}_y) with the largest sum |J| is most likely to be the incoming wave direction:

$$J(k_x, k_y) = \frac{1}{N} \sum_{n=1}^{N} e^{i(k_x x_n + k_y y_n)} F_n(\omega)$$

where J is a complex number that represents the sum over N stations each with a vector (x_n, y_n) that points to an arbitrary reference point. For a given \mathbf{k} , |J| is then the fit of signal propagating with that wavevector. In this study we use one-minute-long time series with no overlaps, apply the Hanning window, calculate J, and then stack and average |J| over a six-hour window. We performed this backprojection on the 27 hurricanes listed in

Table 5-1. There are more sophisticated backprojection approaches like the maximum likelihood method by Capon (1970) and the MUSIC method (Schmidt, 1979), but we have found that this simple approach works quite well for our analysis.

5.3. Results

5.3.1. Backprojection of Tropical Cyclones

The results from the backprojection described above for one six-hour window of Hurricane Sandy is shown in Figure 5.3. The center of the hurricane is given by the green star, the color of which indicates the strength of the storm at that time on the Saffir-Simpson Scale (TS and TD stand for tropical storm and tropical depression, respectively). The colorbar is a logarithmic scale of the power (in dB) normalized to the maximum value of the power, which is the reason the values are negative with a maximum of value of zero. Warm colors indicate the most likely location for the origin of the 0.2 Hz waves.

We find a peak that can be associated with Hurricane Sandy. This peak follows the location of the storm through time, as seen in Figure 5.4, which shows the results from 0600 UTC on 10/28 until 1200 UTC on 10/29. We also observe that the peak is not located directly beneath the reported center of Sandy. There is also a smearing effect on the peak. This smearing is likely an artifact of using one seismic array for the back projection, which tends to elongate the peak in the source-stations (array) direction. The use of another array in a different azimuth could help to better elucidate the true location of the peak.

The reason that the peak is not directly under the center of the storm is likely to be real. Zhang *et al* (2010) also reported a similar phenomenon; in performing a backprojection for Typhoon Ioke (2006), they reported that the P-wave peak often trailed behind the storm. They attribute this to the storm traveling faster than the propagation speed of the ocean infragravity waves, so southward blown waves are interacting with northward waves that

were previously excited by the storm. Our results differ slightly in that many of the P-wave peaks we find are not only behind the storm, but also to the west. Still, these excitation sources must be the locations where wave-wave interactions are occurring, and it follows that this would not be directly beneath the center of the storm. In examining the approximate diameters of the Hurricane Sandy, it is also evident that the peaks occur at the edge of the storm, suggesting this is where more of the wave-wave interactions are taking place. This follows from what we discussed about the wave interactions earlier. In this study, we find that the excitation source does track the location of Hurricane Sandy at least for about a day, as shown in Figure 5.4. The P-wave excitation source can be tracked when Sandy moved northward off the east coast of the United States.

We applied this backprojection method to all 27 hurricanes between 2011 and 2017 that are listed in

Table 5-1. P-wave sources track the storm for some of them only. In order to objectively assess this situation, we calculated the "percent peak time", which is the amount of time where the method resulted in a visible peak compared to the amount of time that the storms were a tropical storm or stronger (hurricanes). Looking at the percent peak time values in Figure 5.5, the hurricanes fall into three groups, and so we categorize them as such: those with over 25% peaks (black), with 15-25% peaks (blue) and less than 15% (red). This grouping becomes more clear when we compare the percentage to hurricane size, as we will discuss below (Figure 5.9 through Figure 5.11). Out of the 27 hurricanes, the back projection yielded consistent peaks for 16 of the storms (black points). Some of these storms

were occurring simultaneously, which complicates the interpretation of the backprojection results. For the main results we focus on the single hurricanes that occurred without interference from another storm, 7 of which had the highest peak percentages. The peak percentage values of all of the single storms are shown in Figure 5.5.

Selected hours showing the backprojection results from these 7 single hurricanes are given in Figure 5.6; these storms are Hurricanes Irene (2011), Katia (2011), Gonzalo (2014), Kate (2015), Gaston (2016), Irma (2017) and Ophelia (2017). In each case, there is a visible peak near the reported center of the storm, although again, the peaks are mostly offset to the south and east like they were with Sandy.

5.3.2. Comparing Hurricane Size

In order to understand why the back projection works for some hurricanes but not for others, we examined two quantities that relate to the size and strength of the storm: (1) the area and (2) the wind speeds. The area is the surface area of the hurricane from the maximum recorded radius of 63km/h winds. We compute them using data from the HURDAT database. This database reports both the maximum sustained wind speed and the maximum recorded radius of 63km/h (34 knots) winds in each quadrant of the storm at every six hours along the hurricane track. This information for each hurricane in this study can be found in Table 5-3 in the Appendix. We used the reported radii to calculate the area of the quarter circle in each quadrant, and then added these together to get the overall area as in Figure 5.7 equation shown and given by the below:

$$A_{hurr} = \frac{\pi}{4} (R_{NE}^2 + R_{SE}^2 + R_{SW}^2 + R_{NW}^2)$$

where R_{NE} , R_{SE} , R_{SW} , and R_{NW} are the reported maximum 63km/h wind radii in the northeast, southeast, southwest and northwest quadrants, respectively. Some examples of the radii data for Hurricane Sandy can be found in Table 5-2. Figure 5.8 shows examples of the area of Hurricane Sandy over time, using the method described. The calculated average 63km/h wind areas and average maximum sustained wind speeds for each of the 27 hurricanes in this study are given in

Table 5-1. In Figure 5.9 and Figure 5.10, we have plotted these values against the peak percentage for all of the single hurricanes. The colors of the points indicate the peak percentages described above. We notice that most of the hurricanes with both low average wind areas and max wind speeds are those with the lower peak percentages (red points). This indicates that the success of tracking a storm with backprojection is dependent on its overall size.

5.4. Discussion

From the backprojection of Hurricane Sandy shown in Figure 5.4 and the other hurricanes shown in Figure 5.6, it is clear that there is potential to track hurricanes over the ocean using this method. It is also evident, as shown in Figure 5.9 and Figure 5.10, that there is some dependence on the overall size of the storm, specifically the wind speeds and the area. It appears that if a storm is too small, then it does not excite enough waves in the frequency band we are looking at, and performing the backprojection does not result in any peaks that we can associate with the storm. The minimum threshold for the average maximum sustained wind speeds seems to be around 100 km/h. There is more variability in

the average area, however, those storms with few back projected peaks have areas on the order of 1.5e5 km² or smaller. It is possible that one factor effects this result more than another, for example, the average area of Hurricane Gaston (2016) falls into the range of areas of the storms for which there were few to no peaks (9.76e4 km²), however it's wind speeds were quite a bit higher (119.7 km/h average), so this could be the reason that the backprojection works more consistently (Figure 5.9 and Figure 5.10).

In Figure 5.11 we show the average wind speeds plotted against the average areas for each of the single storms. Most of the storms with low wind speeds and small areas are clearly those with the lowest percentages of peaks. Some of the storms stand out from the others in terms of their area and wind speeds. Hurricanes Sandy (2012) and Alex (2016) were both considerably larger than the rest of the storms in this study. However, both of these storms became extratropical cyclones at the end of their lifespan, meaning that they lost their hurricane structure, which is also when they grew in size. A few, such as Hurricanes Gonzalo (2014) and Irma (2017), also have very high maximum sustained wind speeds. To further constrain the physical requirements for the backprojection to be successful, more work is required to find an actual cut-off for the overall size of the storm needed.

The case of multiple hurricanes at once complicates how we can interpret the backprojection results. Examples from the multiple storm cases examined in this study are given in Figure 5.12. We show here the results from hurricanes Ophelia and Philippe (2011), Leslie and Michael (2012), Matthew and Nicole (2016) and Jose, Lee and Maria (2017).

Often in the scenario where there are two hurricanes simultaneously, the peak from the backprojection will be between them. This makes sense because two storms tend to create conditions for the wave-wave interactions between the storms, as the ocean waves excited by each individual storm would be meeting somewhere between them. The peaks tend to remain between the storms as long as both cyclones are at least the size of tropical storms or stronger. Once one storm dissipates or grows week, the backprojected peaks tend to then follow whichever large cyclone is left.

5.5. Conclusions

There is clearly potential to track large tropical cyclones over the ocean using the backprojection method presented here. It could provide an additional method to locate these storms in real time, alongside satellite and radar data. With concerns of increasingly powerful and numerous tropical cyclones as a likely result of global warming, new methods of studying these storms using seismic data could be useful (Bromirski and Kossin, 2008; Ebeling and Stein, 2011). There is an apparent dependence on the size of the cyclone in order for the backprojection to work consistently, but it is effective on cyclones with sufficient wind speeds and overall area. The analysis also gets complicated when more than one large cyclone is present in close proximity in the Atlantic, however, for single large cyclones especially, this method holds merit. With further refinement, it could prove a useful tool in studying and tracking tropical cyclones.

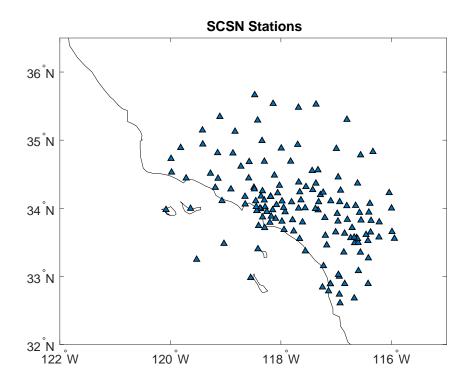


Figure 5.1: Map of the stations in the Southern California Seismic Network.

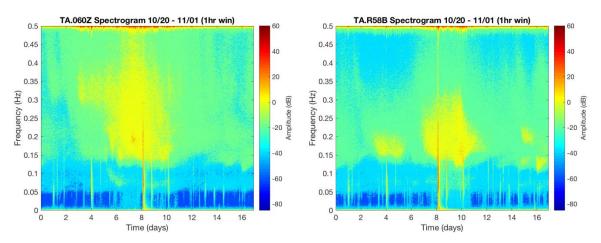


Figure 5.2: Frequency spectra recorded on TA stations R58B and 060Z from October 20 to November 1, 2012. Peaks around 0.2Hz occur at 6-8 days for 060Z and 8-10 days for R58B, which is when Hurricane Sandy was closest to these stations.

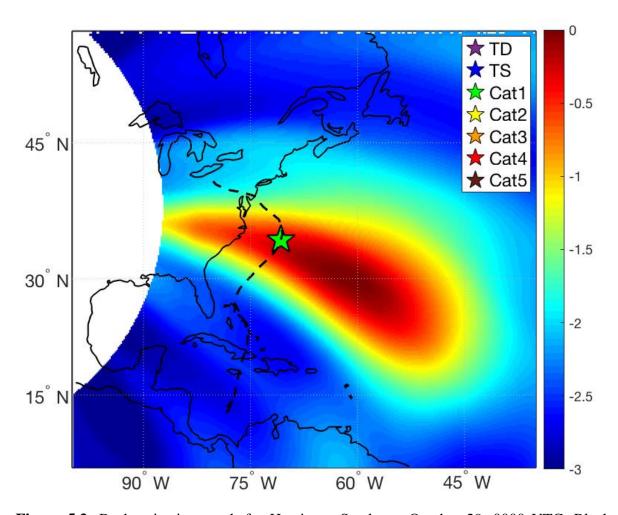


Figure 5.3: Backprojection result for Hurricane Sandy on October 29, 0000 UTC. Black dashed line shows the path of the storm and the green star is the location of the storm center at that time. Units of the color bar are normalized as $\log(dB/dB_{MAX})$. The peak in the 0.2 Hz waves occurs to the east and south of the reported center of Hurricane Sandy.

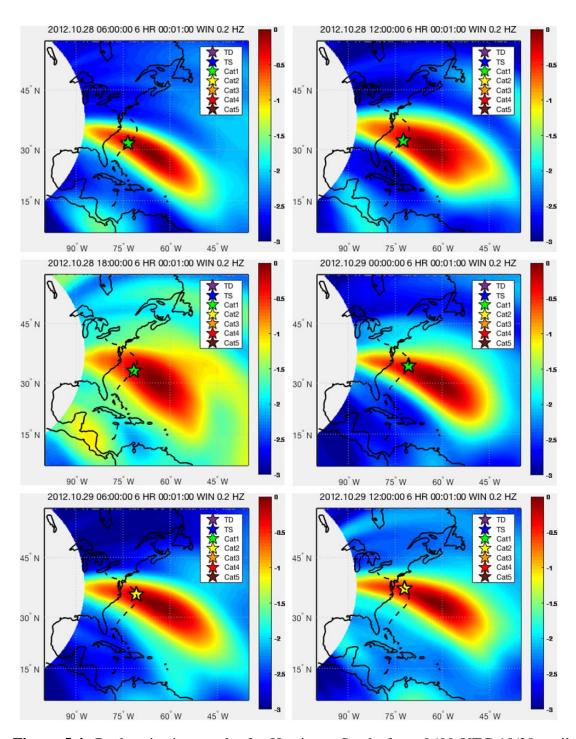


Figure 5.4: Backprojection results for Hurricane Sandy from 0600 UTC 10/28 until 1200 UTC 10/29. Color bar scale is the same as shown in Figure 5.3. As Sandy moves northward in the Atlantic, the backprojected 0.2 Hz peak moves with it.

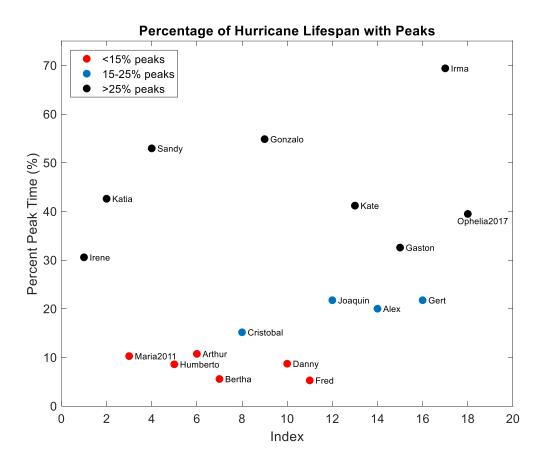


Figure 5.5: The peak percentage time for each of the 18 single hurricanes in this study. Colors indicate the values of the percentage, < 15% (red), 15-25% (blue) and >25% (black).

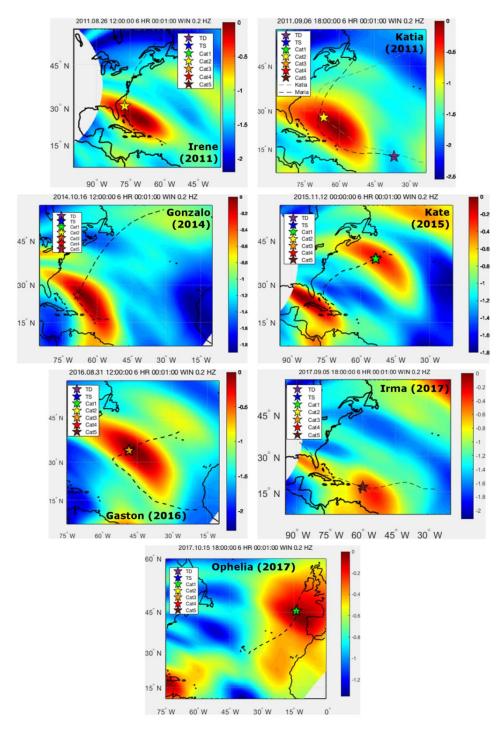


Figure 5.6: Back projection results for Hurricanes Irene (2011), Katia (2011), Gonzalo (2014), Kate (2015), Gaston (2016), Irma (2017) and Ophelia (2017). Each plot shows the results over one six-hour period for each storm.

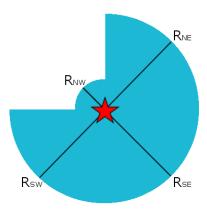


Figure 5.7: Example of calculating the area of a hurricane using the reported maximum wind radii in each quadrant.

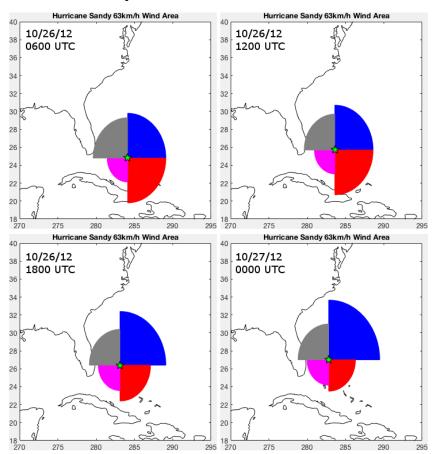


Figure 5.8: Maximum 63km/h wind radii areas for Hurricane Sandy from 10/26 0600 UTC until 10/27 0000 UTC.

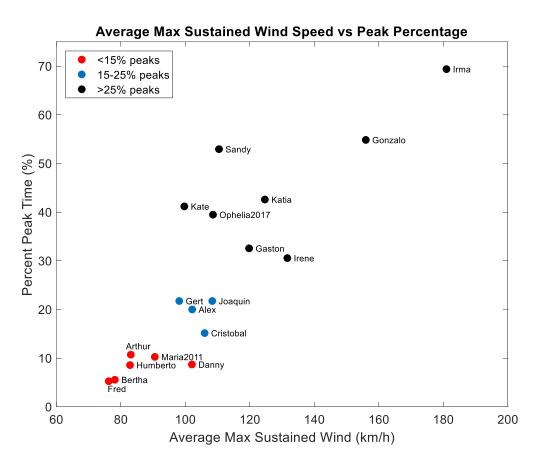


Figure 5.9: Peak percentages against the average maximum sustained wind speed for each storm in this study. Storms with the lowest percentages are also those with the lowest wind speeds.

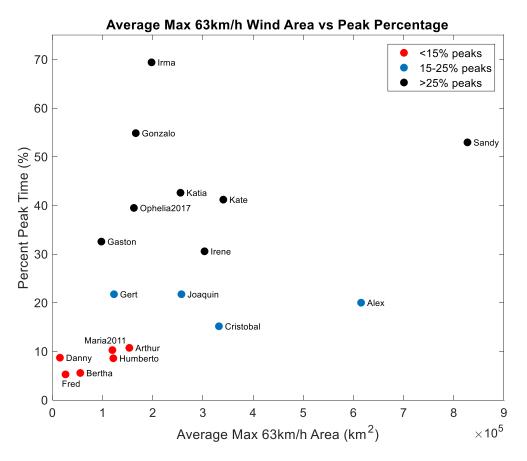


Figure 5.10: Peak percentages against the average 63km/h wind area for each storm in this study. Most storms with the lowest percentages are also those with the smallest areas.

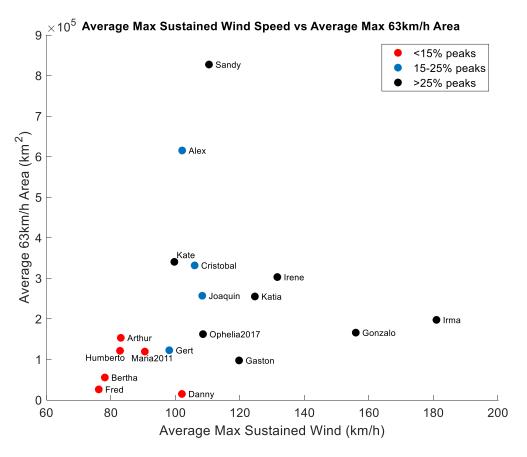


Figure 5.11: Average 63km/h wind areas plotted against the average maximum sustained wind speeds for each storm in this study.

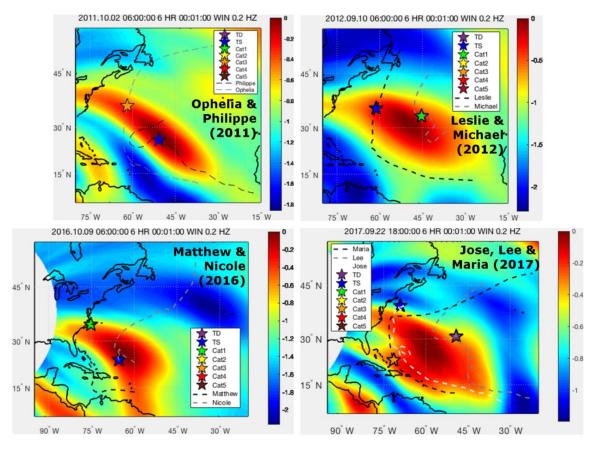


Figure 5.12: Backprojection results for four sets of storms, Hurricanes Ophelia and Philippe (2011), Hurricanes Leslie and Michael (2012), Hurricanes Matthew and Nicole (2016) and Hurricanes Jose, Lee and Maria (2017). Each plot is for a six-hour time period. In each case, the 0.2 Hz peak is generally located between the centers of the storms.

Table 5-1: Names, dates and size information of all hurricanes examined in this study.

Name	Dates	Year	Category	Average 63km/h Area (km^2)	Average Max Sustained Wind (km/h)
Irene	08/21 - 08/28	2011	3	3.03E+05	131.6
Katia	08/29 - 09/10	2011	4	2.49E+05	124.6
Maria	09/06 - 09/16	2011	1	1.19E+05	90.5
Ophelia	09/20 - 10/03	2011	4	1.79E+05	96.4
Philippe	09/24 - 10/08	2011	1	4.10E+04	91.3
Leslie	08/28 - 09/12	2012	1	2.02E+05	99.6
Michael	09/02 - 09/12	2012	3	2.66E+04	111.8

Sandy	10/21 - 10/31	2012	3	8.27E+05	110.4
Humberto	09/08 - 09/19	2013	1	1.21E+05	82.8
Arthur	06/28 - 07/09	2014	2	1.53E+05	83.1
Bertha	07/29 - 08/09	2014	1	5.56E+04	78.1
Cristobal	08/23 - 09/02	2014	1	3.32E+05	106.0
Gonzalo	10/11 - 10/20	2014	4	1.66E+05	155.9
Danny	08/17 - 08/24	2015	3	1.50E+04	102.0
Fred	08/30 - 09/06	2015	1	2.61E+04	76.2
Joaquin	09/26 - 10/15	2015	4	2.57E+05	107.1
Kate	11/08 - 11/13	2015	1	3.41E+05	99.7
Alex	01/12 - 01/15	2016	1	6.15E+05	102.1
Gaston	08/22 - 09/02	2016	3	9.76E+04	119.7
Matthew	09/28 - 10/09	2016	5	1.90E+05	189.6
Nicole	10/04 - 10/18	2016	4	3.58E+05	118.3
Gert	08/12 - 08/18	2017	2	1.23E+05	98.1
Irma	08/30 - 09/13	2017	5	1.98E+05	183.7
Jose	09/04 - 09/25	2017	4	1.57E+05	123.3
Lee	09/14 - 09/30	2017	3	3.33E+04	93.8
Maria	09/16 - 10/02	2017	5	2.34E+05	149.0
Ophelia	10/06 - 10/17	2017	3	1.62E+05	108.5
_					

Table 5-2: Examples of the maximum 63 km/h wind radii in each quadrant as given by HURDAT for Hurricane Sandy.

Date	Hour	Latitude	Longitude	R _{NE} (km)	R _{SE} (km)	R _{SW} (km)	R _{NW} (km)			
20121026	6	25.7	-76.4	555.6	555.6	296.3	444.5			
20121026	12	26.4	-76.9	666.7	444.5	314.8	444.5			
20121026	18	27	-77.2	740.8	388.9	314.8	444.5			
20121027	0	27.5	-77.1	833.4	388.9	333.4	500.0			
	Average 63km/h Area (km^2): 8.27E+05									

127

5.6. Appendix

Table 5-3: Track information for the hurricanes used in this study. Data from the National Hurricane Center's North Atlantic hurricane database (HURDAT).

					Irene				
				Maximum	Minimum	63km/h	63km/h	63km/h	63km/h
Date	Hour	Latitude	Longitude	Sustained Wind	Pressure	Wind NE	Wind SE	Wind SW	Wind NW
				Speed (km/h)	(mbar)	Radii (km)	Radii (km)	Radii (km)	Radii (km)
20110821	0	15	-59	83.3	1006	194.5	0.0	0.0	83.3
20110821	6	16	-60.6	83.3	1006	240.8	0.0	0.0	148.2
20110821	12	16.8	-62.2	83.3	1005	240.8	0.0	0.0	129.6
20110821	18	17.5	-63.7	92.6	999	240.8	37.0	0.0	129.6
20110822	0	17.9	-65	111.1	993	240.8	55.6	55.6	166.7
20110822	6	18.2	-65.9	120.4	990	240.8	111.1	111.1	166.7
20110822	12	18.9	-67	129.6	989	296.3	111.1	111.1	166.7
20110822	18	19.3	-68	138.9	988	296.3	111.1	74.1	166.7
20110823	0	19.7	-68.8	148.2	981	296.3	129.6	92.6	185.2
20110823	6	20.1	-69.7	148.2	978	333.4	222.2	166.7	240.8
20110823	12	20.4	-70.6	148.2	978	333.4	222.2	166.7	240.8
20110823	18	20.7	-71.2	148.2	977	333.4	222.2	166.7	240.8
20110824	0	21	-71.9	148.2	969	333.4	277.8	166.7	277.8
20110824	6	21.3	-72.5	175.9	965	333.4	277.8	166.7	277.8
20110824	12	21.9	-73.3	194.5	957	333.4	277.8	166.7	277.8
20110824	18	22.7	-74.3	185.2	954	370.4	333.4	185.2	277.8
20110825	0	23.5	-75.1	175.9	952	407.4	333.4	185.2	277.8
20110825	6	24.1	-75.9	175.9	950	407.4	333.4	185.2	277.8
20110825	12	25.4	-76.6	166.7	950	463.0	370.4	185.2	296.3

-	_
į.	
U	J
1	0

20110828 20110828	0 6	9.5 9.4	-19 -20.3	37.0 37.0	1012 1011	0.0	0.0	0.0	0.0
				Speed (km/h)	(mbar)	Radii (km)	Radii (km)	Radii (km)	Radii (km)
Date	Hour	Latitude	Longitude	Sustained Wind	Pressure	Wind NE	Wind SE	Wind SW	Wind NW
				Maximum	Minimum	63km/h	63km/h	63km/h	63km/h
					Katia				
20110830	0	53	-60	74.1	991	0.0	500.0	0.0	0.0
20110829	18	51.3	-63.8	74.1	987	0.0	666.7	0.0	0.0
20110829	12	49.1	-66.7	74.1	985	666.7	666.7	555.6	0.0
20110829	6	46.5	-69.5	74.1	983	666.7	666.7	666.7	0.0
20110829	0	44.2	-72.1	83.3	979	426.0	583.4	463.0	92.6
20110828	18	42.5	-73.1	92.6	970	426.0	518.6	333.4	92.6
20110828	13	40.6	-74	101.9	965	426.0	518.6	240.8	92.6
20110828	12	40.3	-74.1	101.9	963	426.0	518.6	240.8	92.6
20110828	9.35	39.4	-74.4	111.1	959	426.0	518.6	296.3	203.7
20110828	6	38.1	-75	120.4	958	426.0	518.6	296.3	203.7
20110828	0	36.7	-75.7	120.4	951	388.9	416.7	277.8	231.5
20110827	18	35.5	-76.3	120.4	950	388.9	416.7	277.8	231.5
20110827	12	34.7	-76.8 -76.6	138.9	952	416.7	416.7	239.3	239.5
20110827	6	33.4	-77.1 -76.8	138.9	952	416.7	416.7	259.3 259.3	259.3
20110826 20110827	18	31.1 32.1	-77.5 -77.1	148.2 138.9	950 952	463.0 416.7	416.7 416.7	259.3	324.1 259.3
20110826	12	30	-77.4	157.4	947	463.0	370.4	240.8	324.1
20110826	6	28.8	-77.3	166.7	942	463.0	370.4	240.8	324.1
20110826	0	27.7	-77.3	166.7	946	463.0	370.4	231.5	296.3
20110825	18	26.5	-77.2	166.7	950	463.0	370.4	231.5	296.3

20110828	18	9.3	-22.9	46.3	1009	0.0	0.0	0.0	0.0
20110829	0	9.3	-24.2	46.3	1009	0.0	0.0	0.0	0.0
20110829	6	9.5	-25.6	46.3	1009	0.0	0.0	0.0	0.0
20110829	12	9.9	-27	55.6	1008	0.0	0.0	0.0	0.0
20110829	18	10.6	-28.2	55.6	1008	0.0	0.0	0.0	0.0
20110830	0	11	-29.6	64.8	1006	55.6	0.0	0.0	55.6
20110830	6	11.5	-31.1	74.1	1004	55.6	0.0	0.0	55.6
20110830	12	12	-32.9	83.3	1001	74.1	55.6	0.0	92.6
20110830	18	12.6	-34.6	92.6	997	92.6	74.1	37.0	111.1
20110831	0	13.1	-36.4	92.6	997	111.1	74.1	37.0	129.6
20110831	6	13.6	-38.2	101.9	994	129.6	74.1	37.0	148.2
20110831	12	14	-40	101.9	994	166.7	92.6	55.6	166.7
20110831	18	14.4	-41.8	111.1	990	185.2	120.4	74.1	203.7
20110901	0	14.8	-43.5	120.4	988	203.7	148.2	92.6	203.7
20110901	6	15.1	-45.2	120.4	988	222.2	166.7	92.6	203.7
20110901	12	15.3	-46.9	120.4	988	240.8	185.2	92.6	222.2
20110901	18	15.7	-48.5	120.4	988	259.3	203.7	92.6	222.2
20110902	0	16.2	-50	120.4	988	259.3	222.2	92.6	222.2
20110902	6	16.8	-51.2	120.4	988	277.8	222.2	92.6	222.2
20110902	12	17.4	-52.1	120.4	987	277.8	222.2	111.1	222.2
20110902	18	18	-53	120.4	987	277.8	222.2	129.6	222.2
20110903	0	18.4	-53.9	120.4	987	277.8	222.2	129.6	222.2
20110903	6	18.8	-54.7	120.4	987	277.8	222.2	129.6	222.2
20110903	12	19.4	-55.4	120.4	986	277.8	222.2	129.6	222.2
20110903	18	19.9	-56.2	120.4	982	277.8	222.2	129.6	222.2
20110904	0	20.4	-57.1	129.6	978	277.8	222.2	129.6	222.2
20110904	6	21.1	-57.9	138.9	969	277.8	222.2	129.6	222.2

				1					
20110904	12	21.7	-58.8	157.4	961	277.8	222.2	148.2	222.2
20110904	18	22.3	-59.7	166.7	959	277.8	222.2	148.2	222.2
20110905	0	23	-60.6	166.7	957	277.8	222.2	166.7	240.8
20110905	6	23.6	-61.6	175.9	954	296.3	222.2	166.7	240.8
20110905	12	24.2	-62.6	185.2	950	314.8	222.2	185.2	259.3
20110905	18	24.8	-63.4	203.7	946	333.4	222.2	185.2	259.3
20110906	0	25.6	-64	222.2	942	333.4	222.2	203.7	259.3
20110906	6	26.2	-64.8	213.0	946	333.4	222.2	203.7	259.3
20110906	12	26.7	-65.6	194.5	954	333.4	222.2	203.7	259.3
20110906	18	27.3	-66.2	175.9	959	333.4	231.5	222.2	259.3
20110907	0	27.7	-66.9	157.4	964	333.4	240.8	222.2	277.8
20110907	6	28.2	-67.6	157.4	967	333.4	259.3	222.2	277.8
20110907	12	28.8	-68.4	148.2	969	333.4	277.8	222.2	296.3
20110907	18	29.4	-69.3	148.2	969	333.4	296.3	222.2	314.8
20110908	0	30.3	-69.9	148.2	968	351.9	314.8	277.8	333.4
20110908	6	31.5	-70.1	148.2	967	370.4	333.4	277.8	333.4
20110908	12	32.8	-70.2	148.2	966	370.4	333.4	277.8	333.4
20110908	18	34.1	-70	148.2	965	370.4	351.9	333.4	296.3
20110909	0	35.6	-69.4	148.2	964	370.4	370.4	333.4	296.3
20110909	6	37.1	-68.4	138.9	963	370.4	388.9	277.8	296.3
20110909	12	38.5	-67.1	138.9	961	370.4	407.4	296.3	296.3
20110909	18	39.8	-64.6	138.9	960	370.4	407.4	351.9	296.3
20110910	0	41	-60.5	138.9	958	370.4	426.0	407.4	296.3
20110910	6	42.2	-56.1	138.9	956	370.4	463.0	463.0	296.3
20110910	12	43.5	-50.6	138.9	954	370.4	500.0	500.0	296.3
20110910	18	45.4	-43.7	138.9	954	370.4	500.0	500.0	296.3
20110911	0	47.3	-37.2	129.6	957	370.4	500.0	500.0	296.3

20110011		10.1	21.2	120.6	0.60	270.4	500.0	700.0	2062
20110911	6	49.1	-31.3	129.6	960	370.4	500.0	500.0	296.3
20110911	12	51.1	-26	111.1	964	370.4	500.0	500.0	296.3
20110911	18	52.8	-21.1	111.1	966	370.4	500.0	500.0	296.3
20110912	0	54.7	-16.3	111.1	968	370.4	500.0	500.0	296.3
20110912	6	56.2	-11.6	111.1	970	370.4	500.0	500.0	296.3
20110912	12	58	-7	111.1	972	370.4	500.0	500.0	296.3
20110912	18	59.5	0	111.1	974	370.4	500.0	500.0	296.3
					Maria				

					Maria				
Date	Hour	Latitude	Longitude	Maximum Sustained Wind	Minimum Pressure	63km/h Wind NE	63km/h Wind SE	63km/h Wind SW	63km/h Wind NW
				Speed (km/h)	(mbar)	Radii (km)	Radii (km)	Radii (km)	Radii (km)
20110906	18	11.5	-35.9	55.6	1008	0.0	0.0	0.0	0.0
20110907	0	11.9	-37.5	64.8	1007	111.1	0.0	0.0	0.0
20110907	6	12.3	-39.1	74.1	1006	111.1	0.0	0.0	0.0
20110907	12	12.8	-41	83.3	1004	138.9	0.0	0.0	138.9
20110907	18	13	-43	83.3	1004	166.7	0.0	0.0	138.9
20110908	0	13.2	-45.2	83.3	1003	185.2	0.0	0.0	166.7
20110908	6	13.2	-47.7	83.3	1002	277.8	0.0	0.0	166.7
20110908	12	13	-50.1	74.1	1004	277.8	0.0	0.0	166.7
20110908	18	13.2	-52.1	74.1	1004	250.0	0.0	0.0	166.7
20110909	0	13.5	-53.7	74.1	1004	250.0	0.0	0.0	166.7
20110909	6	13.9	-55.2	74.1	1003	250.0	0.0	0.0	185.2
20110909	12	14.3	-56.6	83.3	1003	250.0	0.0	0.0	185.2
20110909	18	14.9	-57.9	83.3	1004	250.0	111.1	0.0	185.2
20110910	0	15.4	-59	83.3	1004	277.8	250.0	0.0	185.2
20110910	6	16	-60	83.3	1005	277.8	166.7	0.0	185.2
20110910	12	16.9	-61.1	83.3	1005	277.8	0.0	0.0	0.0

_		٥
5		
(٨	1
:	_	Ĭ
ľ	۸	J

20110910	18	17.8	-62	83.3	1005	277.8	0.0	0.0	0.0
20110910	0	18.3	-62.7	83.3	1005	333.4	0.0	0.0	138.9
20110911	6	18.7	-63.4	92.6	1003	333.4	0.0	0.0	138.9
20110911	12	19.1	-64.1	92.6	1004	333.4	138.9	0.0	156.9
20110911	18	19.1	-64.7	92.6	1004	333.4	185.2	0.0	166.7
20110911	0	20	-65.3	92.6	1005	333.4	185.2	0.0	166.7
20110912	6	20.4	-66.1	92.6	1005	333.4	185.2	0.0	166.7
20110912	12	20.4	-66.9	92.6	1005	333.4	185.2	0.0	111.1
20110912	18	20.8	-67.1	92.6	1006	333.4	333.4	0.0	111.1
20110912	0	20.8	-67.3	83.3	1006	388.9	333.4	0.0	111.1
20110913	6	21.3	-67.5	83.3	1006	333.4	333.4	0.0	0.0
20110913	12	21.7	-67.7	83.3	1006	333.4	333.4	0.0	0.0
20110913	18	22.3	-68	83.3	1005	277.8	277.8	0.0	0.0
20110913	0	23.1	-68.5	83.3	1003	277.8	277.8	0.0	111.1
20110914	6	23.9	-69	92.6	1004	277.8	277.8	0.0	111.1
20110914	12	24.7	-69.3	92.6	1001	277.8	277.8	0.0	111.1
20110914	18	25.8	-69.3	101.9	1000	277.8	277.8	0.0	0.0
20110915	0	27.2	-68.9	111.1	999	333.4	333.4	0.0	0.0
20110915	6	28.8	-68.4	111.1	995	333.4	333.4	0.0	0.0
20110915	12	30.9	-67.8	111.1	991	333.4	333.4	0.0	0.0
20110915	18	33.7	-66.9	120.4	987	333.4	333.4	111.1	111.1
20110916	0	36.8	-64.8	129.6	984	333.4	333.4	111.1	111.1
20110916	6	39.8	-62.1	129.6	983	333.4	333.4	111.1	111.1
20110916	12	42.9	-58.2	120.4	983	333.4	444.5	111.1	111.1
20110916	18	46.7	-53.9	111.1	983	555.6	500.0	111.1	111.1
	10	,			Ophelia	223.0	200.0		
Date	Hour	Latitude	Longitude	Maximum	Minimum	63km/h	63km/h	63km/h	63km/h

				Sustained Wind	Pressure	Wind NE	Wind SE	Wind SW	Wind NW
				Speed (km/h)	(mbar)	Radii (km)	Radii (km)	Radii (km)	Radii (km)
20110920	6	11.6	-37	46.3	1008	0.0	0.0	0.0	0.0
20110920	12	11.9	-37.7	46.3	1007	0.0	0.0	0.0	0.0
20110920	18	12.2	-38.6	55.6	1007	0.0	0.0	0.0	0.0
20110921	0	12.5	-39.7	74.1	1005	277.8	0.0	0.0	222.2
20110921	6	12.7	-41.1	83.3	1004	277.8	166.7	0.0	277.8
20110921	12	12.9	-42.6	92.6	999	370.4	222.2	0.0	333.4
20110921	18	13.1	-44.1	92.6	999	370.4	222.2	0.0	333.4
20110922	0	13.3	-45.2	92.6	998	370.4	222.2	0.0	333.4
20110922	6	13.5	-46.3	101.9	993	370.4	222.2	0.0	333.4
20110922	12	13.7	-47.3	101.9	993	370.4	222.2	111.1	333.4
20110922	18	13.9	-48.3	92.6	997	370.4	222.2	111.1	333.4
20110923	0	14.1	-49.4	83.3	1000	407.4	222.2	111.1	277.8
20110923	6	14.4	-50.5	74.1	1003	407.4	222.2	0.0	222.2
20110923	12	14.7	-51.7	83.3	1003	407.4	222.2	0.0	185.2
20110923	18	15.2	-52.9	92.6	1001	407.4	185.2	0.0	185.2
20110924	0	15.8	-54	83.3	1004	407.4	185.2	0.0	185.2
20110924	6	16.5	-54.8	83.3	1005	407.4	185.2	0.0	185.2
20110924	12	17.2	-55.9	83.3	1005	407.4	185.2	0.0	185.2
20110924	18	17.6	-57	74.1	1007	407.4	185.2	0.0	185.2
20110925	0	17.9	-58	74.1	1008	407.4	185.2	0.0	185.2
20110925	6	18.2	-59	64.8	1008	370.4	185.2	0.0	0.0
20110925	12	18.4	-59.8	55.6	1010	0.0	0.0	0.0	0.0
20110925	18	18.6	-60.5	55.6	1012	0.0	0.0	0.0	0.0
20110926	0	18.5	-60.8	46.3	1012	0.0	0.0	0.0	0.0
20110926	6	18.3	-60.7	46.3	1012	0.0	0.0	0.0	0.0

								Т	
20110926	12	18	-60.5	46.3	1012	0.0	0.0	0.0	0.0
20110926	18	17.8	-60.2	46.3	1012	0.0	0.0	0.0	0.0
20110927	0	17.6	-59.9	46.3	1012	0.0	0.0	0.0	0.0
20110927	6	17.6	-59.5	46.3	1012	0.0	0.0	0.0	0.0
20110927	12	17.8	-59.3	46.3	1010	0.0	0.0	0.0	0.0
20110927	18	18	-59.4	46.3	1009	0.0	0.0	0.0	0.0
20110928	0	18.1	-59.5	55.6	1009	0.0	0.0	0.0	0.0
20110928	6	18.2	-59.6	74.1	1005	111.1	111.1	0.0	0.0
20110928	12	18.4	-59.8	74.1	1001	138.9	138.9	0.0	55.6
20110928	18	18.7	-60.1	83.3	1001	138.9	138.9	0.0	83.3
20110929	0	19.1	-60.5	92.6	995	166.7	138.9	0.0	138.9
20110929	6	19.6	-60.9	101.9	995	166.7	138.9	0.0	138.9
20110929	12	20.2	-61.4	101.9	991	166.7	138.9	0.0	138.9
20110929	18	21	-61.9	120.4	987	222.2	166.7	111.1	138.9
20110930	0	21.6	-62.3	129.6	982	277.8	222.2	111.1	166.7
20110930	6	22.4	-62.7	157.4	971	277.8	277.8	111.1	166.7
20110930	12	23.4	-63	175.9	966	277.8	277.8	111.1	166.7
20110930	18	24.6	-63.3	185.2	959	277.8	277.8	111.1	166.7
20111001	0	25.9	-63.3	194.5	955	333.4	333.4	111.1	166.7
20111001	6	27.3	-63.2	194.5	951	333.4	333.4	148.2	166.7
20111001	12	28.9	-63.1	194.5	948	333.4	333.4	148.2	166.7
20111001	18	30.7	-62.9	203.7	946	333.4	333.4	148.2	166.7
20111002	0	32.8	-62.5	222.2	940	333.4	333.4	148.2	166.7
20111002	6	35	-62.1	203.7	945	333.4	333.4	148.2	166.7
20111002	12	37.4	-61.6	194.5	951	333.4	333.4	148.2	166.7
20111002	18	40.1	-60.8	166.7	960	333.4	370.4	148.2	166.7
20111003	0	42.8	-59.6	129.6	972	333.4	370.4	185.2	166.7

20111004	12	51.3	-31.9	74.1	996	0.0	403.0	0.0	0.0
20111004	1.0	510	21.0	7.4.1	006	0.0	463.0	0.0	0.0
20111004	6	50.6	-37.8	74.1	996	0.0	463.0	0.0	0.0
20111004	0	49.9	-43.6	74.1	994	0.0	463.0	0.0	0.0
20111003	18	48.9	-49.2	83.3	994	277.8	463.0	324.1	111.1
20111003	12	47.4	-54	92.6	994	277.8	463.0	277.8	111.1
20111003	10	46.9	-55.4	111.1	990	333.4	370.4	222.2	111.1
20111003	6	45.4	-57.6	111.1	980	333.4	370.4	222.2	111.1

	Philippe									
				Maximum	Minimum	63km/h	63km/h	63km/h	63km/h	
Date	Hour	Latitude	Longitude	Sustained Wind	Pressure	Wind NE	Wind SE	Wind SW	Wind NW	
				Speed (km/h)	(mbar)	Radii (km)	Radii (km)	Radii (km)	Radii (km)	
20110923	0	8.3	-17.5	37.0	1010	0.0	0.0	0.0	0.0	
20110923	6	8.6	-19.1	37.0	1010	0.0	0.0	0.0	0.0	
20110923	12	9	-20.6	46.3	1010	0.0	0.0	0.0	0.0	
20110923	18	9.5	-22	46.3	1009	0.0	0.0	0.0	0.0	
20110924	0	10.4	-23.3	55.6	1008	0.0	0.0	0.0	0.0	
20110924	6	11	-24.7	55.6	1007	0.0	0.0	0.0	0.0	
20110924	12	11.1	-26.1	64.8	1006	55.6	0.0	0.0	55.6	
20110924	18	11.2	-27.3	64.8	1006	55.6	0.0	0.0	55.6	
20110925	0	11.5	-28.4	64.8	1006	55.6	0.0	0.0	83.3	
20110925	6	12.1	-29.4	74.1	1006	83.3	55.6	55.6	83.3	
20110925	12	12.7	-30.3	74.1	1006	83.3	55.6	55.6	83.3	
20110925	18	13.2	-31.2	83.3	1005	83.3	55.6	83.3	111.1	
20110926	0	13.8	-32.1	83.3	1005	111.1	83.3	83.3	111.1	
20110926	6	14.4	-33	83.3	1004	111.1	83.3	83.3	111.1	
20110926	12	14.9	-33.6	92.6	1003	111.1	83.3	83.3	111.1	
20110926	18	15.3	-34.1	92.6	1003	111.1	111.1	83.3	111.1	

ļ		`	
	_	ĭ	

20110927	0	15.4	-34.4	83.3	1004	138.9	111.1	111.1	83.3
20110927	6	15.5	-34.7	83.3	1004	138.9	138.9	111.1	83.3
20110927	12	15.6	-35.2	74.1	1005	138.9	111.1	83.3	83.3
20110927	18	15.7	-35.8	64.8	1006	138.9	83.3	0.0	83.3
20110928	0	15.8	-36.6	55.6	1007	0.0	0.0	0.0	0.0
20110928	6	16	-37.4	55.6	1007	0.0	0.0	0.0	0.0
20110928	12	16.2	-38.4	64.8	1006	166.7	111.1	0.0	83.3
20110928	18	16.6	-39.4	74.1	1005	166.7	111.1	0.0	83.3
20110929	0	17.1	-40.5	74.1	1005	166.7	111.1	0.0	83.3
20110929	6	17.8	-41.5	83.3	1004	166.7	111.1	0.0	83.3
20110929	12	18.7	-42.3	83.3	1004	166.7	83.3	0.0	83.3
20110929	18	19.7	-43	83.3	1005	166.7	83.3	0.0	111.1
20110930	0	20.7	-43.6	74.1	1007	166.7	55.6	0.0	111.1
20110930	6	21.7	-44.2	74.1	1007	138.9	55.6	0.0	111.1
20110930	12	22.5	-44.8	83.3	1006	138.9	55.6	55.6	111.1
20110930	18	23.2	-45.6	83.3	1005	138.9	55.6	55.6	111.1
20111001	0	23.8	-46.3	92.6	1003	138.9	55.6	55.6	111.1
20111001	6	24.1	-47	101.9	999	138.9	83.3	55.6	138.9
20111001	12	24.4	-47.6	111.1	997	166.7	83.3	83.3	138.9
20111001	18	24.8	-48.4	111.1	995	166.7	111.1	83.3	166.7
20111002	0	25.2	-49.3	111.1	993	166.7	138.9	83.3	166.7
20111002	6	25.8	-50.3	92.6	998	166.7	138.9	83.3	166.7
20111002	12	26.2	-51.2	74.1	1004	166.7	138.9	83.3	166.7
20111002	18	26.3	-52.3	74.1	1004	166.7	138.9	111.1	166.7
20111003	0	26.2	-53.2	83.3	1004	166.7	138.9	111.1	166.7
20111003	6	25.6	-54	92.6	1001	166.7	138.9	83.3	138.9
20111003	12	24.9	-54.8	101.9	998	166.7	138.9	83.3	111.1

L		
7		`
ž	5	_

20111065	4.0				0.5 = 1		100 -	0.5.5.1	
20111003	18	24.3	-55.6	111.1	995	166.7	138.9	83.3	111.1
20111004	0	23.8	-56.6	120.4	992	166.7	138.9	83.3	111.1
20111004	6	23.7	-57.7	120.4	992	166.7	138.9	83.3	111.1
20111004	12	23.8	-58.7	111.1	993	138.9	138.9	83.3	83.3
20111004	18	24	-59.6	111.1	994	138.9	138.9	55.6	83.3
20111005	0	24.3	-60.2	111.1	994	138.9	138.9	55.6	55.6
20111005	6	24.7	-60.7	111.1	994	138.9	138.9	55.6	55.6
20111005	12	25.2	-61	101.9	995	138.9	138.9	83.3	83.3
20111005	18	25.5	-61.1	101.9	995	138.9	138.9	83.3	83.3
20111006	0	25.9	-61.1	111.1	992	138.9	138.9	83.3	83.3
20111006	6	26.5	-61	120.4	987	138.9	138.9	83.3	83.3
20111006	12	27.4	-60.4	129.6	983	138.9	138.9	83.3	83.3
20111006	18	28.2	-59.7	148.2	977	111.1	138.9	111.1	111.1
20111007	0	28.7	-58.8	148.2	976	111.1	138.9	111.1	138.9
20111007	6	29	-57.7	148.2	976	111.1	138.9	138.9	138.9
20111007	12	29.3	-56.5	148.2	977	138.9	166.7	138.9	138.9
20111007	18	29.7	-55.1	129.6	981	138.9	166.7	138.9	138.9
20111008	0	30.1	-53.5	120.4	986	111.1	166.7	138.9	138.9
20111008	6	30.9	-51.4	111.1	987	111.1	166.7	138.9	138.9
20111008	12	32.3	-48.7	111.1	987	138.9	166.7	138.9	138.9
					Leslie				
				Maximum	Minimum	63km/h	63km/h	63km/h	63km/h
Date	Hour	Latitude	Longitude	Sustained Wind	Pressure	Wind NE	Wind SE	Wind SW	Wind NW
				Speed (km/h)	(mbar)	Radii (km)	Radii (km)	Radii (km)	Radii (km)
20120828	12	12.9	-27.4	37.0	1010	0.0	0.0	0.0	0.0
20120828	18	13	-29.6	37.0	1010	0.0	0.0	0.0	0.0
20120829	0	13.1	-31.7	46.3	1009	0.0	0.0	0.0	0.0

20120829	6	13.2	-33.7	46.3	1009	0.0	0.0	0.0	0.0
20120829	12	13.3	-35.6	46.3	1009	0.0	0.0	0.0	0.0
20120829	18	13.4	-37.5	46.3	1008	0.0	0.0	0.0	0.0
20120830	0	13.5	-39.2	55.6	1007	0.0	0.0	0.0	0.0
20120830	6	13.6	-40.9	55.6	1006	0.0	0.0	0.0	0.0
20120830	12	13.8	-42.6	64.8	1005	55.6	0.0	0.0	0.0
20120830	18	14.2	-44.2	74.1	1004	74.1	55.6	0.0	74.1
20120831	0	14.7	-45.8	83.3	1002	74.1	55.6	0.0	74.1
20120831	6	15.3	-47.4	92.6	1001	111.1	92.6	55.6	111.1
20120831	12	16	-49	101.9	999	111.1	92.6	55.6	111.1
20120831	18	16.5	-50.6	101.9	999	148.2	111.1	74.1	129.6
20120901	0	17.1	-52.2	111.1	998	148.2	111.1	74.1	129.6
20120901	6	17.6	-53.8	111.1	996	185.2	166.7	92.6	166.7
20120901	12	18.1	-55.3	111.1	995	222.2	259.3	111.1	185.2
20120901	18	18.8	-56.8	111.1	994	222.2	259.3	111.1	222.2
20120902	0	19.6	-58.1	111.1	994	277.8	277.8	111.1	259.3
20120902	6	20.4	-59.4	101.9	995	277.8	277.8	111.1	259.3
20120902	12	21.2	-60.7	92.6	997	333.4	333.4	111.1	259.3
20120902	18	22.1	-61.4	92.6	997	333.4	296.3	111.1	259.3
20120903	0	22.9	-61.7	92.6	997	333.4	296.3	111.1	259.3
20120903	6	23.4	-62.2	92.6	996	333.4	296.3	111.1	259.3
20120903	12	23.5	-62.6	92.6	993	333.4	296.3	111.1	259.3
20120903	18	23.8	-62.8	101.9	990	333.4	296.3	111.1	240.8
20120904	0	24.2	-62.6	111.1	989	333.4	333.4	111.1	222.2
20120904	6	24.5	-62.5	111.1	988	333.4	333.4	111.1	203.7
20120904	12	24.8	-62.5	111.1	988	333.4	333.4	111.1	185.2
20120904	18	25	-62.6	111.1	988	259.3	370.4	111.1	185.2

١		
	^	
	Ξ	ı

20120905	0	25.2	-62.8	111.1	988	259.3	370.4	111.1	185.2
20120905	6	25.4	-62.8	120.4	985	259.3	370.4	111.1	259.3
20120905	12	25.6	-62.8	129.6	982	259.3	370.4	111.1	259.3
20120905	18	25.8	-62.7	129.6	982	277.8	370.4	111.1	259.3
20120906	0	26	-62.6	120.4	984	296.3	314.8	185.2	277.8
20120906	6	26.2	-62.5	120.4	984	296.3	314.8	185.2	277.8
20120906	12	26.3	-62.4	120.4	983	296.3	314.8	185.2	277.8
20120906	18	26.4	-62.3	120.4	982	296.3	259.3	185.2	259.3
20120907	0	26.5	-62.2	120.4	982	296.3	259.3	185.2	259.3
20120907	6	26.6	-62.2	120.4	982	296.3	259.3	185.2	259.3
20120907	12	26.8	-62.2	111.1	981	296.3	259.3	185.2	259.3
20120907	18	27.1	-62.2	111.1	981	296.3	259.3	185.2	277.8
20120908	0	27.4	-62.3	111.1	983	296.3	259.3	185.2	277.8
20120908	6	27.8	-62.4	101.9	985	296.3	259.3	185.2	277.8
20120908	12	28.3	-62.5	101.9	987	296.3	259.3	185.2	277.8
20120908	18	29	-62.5	101.9	988	296.3	259.3	185.2	277.8
20120909	0	29.7	-62.6	101.9	988	296.3	259.3	185.2	277.8
20120909	6	30.5	-62.6	101.9	988	314.8	277.8	240.8	277.8
20120909	12	31.5	-62.5	101.9	988	314.8	277.8	240.8	277.8
20120909	18	32.6	-62.3	101.9	988	314.8	277.8	222.2	277.8
20120910	0	33.8	-62	101.9	988	314.8	277.8	222.2	277.8
20120910	6	35.1	-61.6	111.1	985	333.4	333.4	259.3	277.8
20120910	12	36.4	-60.8	120.4	980	333.4	333.4	259.3	277.8
20120910	18	38.5	-59.8	120.4	975	333.4	333.4	259.3	277.8
20120911	0	41.1	-58.6	120.4	970	333.4	333.4	259.3	277.8
20120911	6	44	-57.3	120.4	968	500.0	500.0	333.4	277.8
20120911	9	45.8	-56.1	120.4	968	500.0	500.0	333.4	277.8

_	_
1	_
۲	-

20120906

30.3

18

-41

20120911	12	47.7	-54.9	120.4	970	555.6	555.6	333.4	277.8
20120911	18	51.6	-51.9	111.1	972	555.6	555.6	333.4	277.8
20120912	0	55.5	-48.5	101.9	975	555.6	555.6	333.4	277.8
				Ī	Michael				
				Maximum	Minimum	63km/h	63km/h	63km/h	63km/h
Date	Hour	Latitude	Longitude	Sustained Wind	Pressure	Wind NE	Wind SE	Wind SW	Wind NW
				Speed (km/h)	(mbar)	Radii (km)	Radii (km)	Radii (km)	Radii (km)
20120902	0	28.9	-36.7	37.0	1015	0.0	0.0	0.0	0.0
20120902	6	28.1	-37.9	46.3	1015	0.0	0.0	0.0	0.0
20120902	12	27.2	-39.2	46.3	1015	0.0	0.0	0.0	0.0
20120902	18	26.4	-40.1	46.3	1015	0.0	0.0	0.0	0.0
20120903	0	25.8	-40.7	46.3	1015	0.0	0.0	0.0	0.0
20120903	6	25.4	-41.2	46.3	1015	0.0	0.0	0.0	0.0
20120903	12	25.3	-41.7	46.3	1014	0.0	0.0	0.0	0.0
20120903	18	25.5	-42.1	55.6	1013	0.0	0.0	0.0	0.0
20120904	0	25.8	-42.5	55.6	1011	0.0	0.0	0.0	0.0
20120904	6	26.2	-43	64.8	1009	55.6	0.0	0.0	37.0
20120904	12	26.7	-43.5	74.1	1007	55.6	55.6	0.0	37.0
20120904	18	27.1	-43.7	83.3	1006	55.6	55.6	37.0	37.0
20120905	0	27.4	-43.8	83.3	1005	55.6	55.6	37.0	37.0
20120905	6	27.8	-43.8	83.3	1005	55.6	55.6	37.0	55.6
20120905	12	28.2	-43.5	92.6	1001	92.6	74.1	37.0	55.6
20120905	18	28.6	-43.1	120.4	992	92.6	74.1	37.0	55.6
20120906	0	29	-42.6	148.2	981	111.1	74.1	37.0	74.1
20120906	6	29.4	-42	175.9	968	111.1	111.1	55.6	74.1
20120906	12	29.9	-41.4	185.2	964	111.1	111.1	55.6	74.1
20120006	1.0	20.2	4.1	175.0	0.60	1111	111 1	7.4.1	741

968

175.9

111.1

111.1

74.1

74.1

۰	_
_	℩⋋
-	_
	``
ı	$\mathbf{}$

20120907	0	30.6	-40.8	1667	970	111.1	111.1	92.6	02.6
				166.7					92.6
20120907	6	30.9	-40.8	166.7	970	111.1	111.1	92.6	92.6
20120907	12	31.1	-41	166.7	970	111.1	111.1	92.6	92.6
20120907	18	31.3	-41.2	157.4	973	111.1	111.1	92.6	92.6
20120908	0	31.6	-41.5	148.2	977	111.1	111.1	74.1	74.1
20120908	6	32	-41.7	148.2	978	111.1	111.1	74.1	74.1
20120908	12	32.4	-41.9	157.4	975	111.1	111.1	74.1	74.1
20120908	18	32.9	-42.1	166.7	972	111.1	111.1	74.1	74.1
20120909	0	33.3	-42.3	166.7	973	111.1	111.1	74.1	74.1
20120909	6	33.6	-42.6	157.4	976	111.1	111.1	74.1	74.1
20120909	12	33.7	-42.9	157.4	976	111.1	111.1	92.6	111.1
20120909	18	33.7	-43.5	148.2	979	111.1	111.1	92.6	111.1
20120910	0	33.6	-44.1	138.9	982	129.6	129.6	111.1	111.1
20120910	6	33.4	-44.9	129.6	985	129.6	129.6	111.1	111.1
20120910	12	33.6	-45.8	129.6	986	129.6	129.6	111.1	111.1
20120910	18	33.9	-46.9	120.4	988	129.6	129.6	111.1	111.1
20120911	0	34.8	-47.8	111.1	991	129.6	129.6	55.6	55.6
20120911	6	36.4	-47.8	101.9	994	129.6	129.6	0.0	0.0
20120911	12	38.2	-47.6	83.3	997	129.6	129.6	0.0	0.0
20120911	18	40.2	-46.6	74.1	1000	129.6	129.6	0.0	0.0
20120912	0	42.5	-45	64.8	1003	129.6	129.6	0.0	0.0
20120912	6	45	-42.6	55.6	1006	0.0	0.0	0.0	0.0
					Sandy				
				Maximum	Minimum	63km/h	63km/h	63km/h	63km/h
Date	Hour	Latitude	Longitude	Sustained Wind	Pressure	Wind NE	Wind SE	Wind SW	Wind NW
			Ü	Speed (km/h)	(mbar)	Radii (km)	Radii (km)	Radii (km)	Radii (km)
20121021	18	14.3	-77.4	46.3	1006	0.0	0.0	0.0	0.0

20121023	0	12.6	-78.4	74.1	998	92.6	111.1	0.0	0.0
20121023	6	12.9	-78.1	74.1	998	129.6	148.2	0.0	0.0
20121023	12	13.4	-77.9	74.1	995	185.2	185.2	0.0	0.0
20121023	18	14	-77.6	83.3	993	185.2	222.2	0.0	0.0
20121024	0	14.7	-77.3	101.9	990	185.2	277.8	74.1	74.1
20121024	6	15.6	-77.1	111.1	987	185.2	277.8	92.6	92.6
20121024	12	16.6	-76.9	120.4	981	222.2	296.3	129.6	129.6
20121024	18	17.7	-76.7	138.9	972	277.8	333.4	129.6	129.6
20121025	0	18.9	-76.4	157.4	964	333.4	444.5	129.6	129.6
20121025	6	20.1	-76	185.2	954	444.5	444.5	129.6	222.2
20121025	9	20.9	-75.7	175.9	960	444.5	444.5	129.6	333.4
20121025	12	21.7	-75.5	175.9	966	444.5	444.5	129.6	444.5
20121025	18	23.3	-75.3	166.7	963	500.0	500.0	222.2	500.0
20121026	0	24.8	-75.9	138.9	965	555.6	555.6	296.3	500.0
20121026	6	25.7	-76.4	129.6	968	555.6	555.6	296.3	444.5
20121026	12	26.4	-76.9	120.4	970	666.7	444.5	314.8	444.5
20121026	18	27	-77.2	120.4	971	740.8	388.9	314.8	444.5
20121027	0	27.5	-77.1	111.1	969	833.4	388.9	333.4	500.0
20121027	6	28.1	-76.9	111.1	968	833.4	481.5	333.4	518.6
20121027	12	28.8	-76.5	129.6	956	833.4	555.6	388.9	518.6

129.6

120.4

120.4

1005

1003

1002

1000

960

960

959

833.4

889.0

833.4

0.0

0.0

0.0

92.6

0.0

0.0

0.0

111.1

555.6

555.6

555.6

0.0

0.0

0.0

0.0

444.5

555.6

555.6

0.0

0.0

0.0

0.0

518.6

518.6

500.0

46.3

46.3

55.6

64.8

20121022

20121022

20121022

20121022

20121027

20121028

20121028

18

0

6

29.7

30.5

31.3

0

6

12

18

13.9

13.5

13.1

12.7

-77.8

-78.2

-78.6

-78.7

-75.6

-74.7

-73.9

L	_
	$\overline{}$
-	-
	◺

20121028	12	32	-73	120.4	954	833.4	555.6	555.6	500.0
20121028	18	32.8	-72	120.4	952	833.4	555.6	648.2	500.0
20121029	0	33.9	-71	129.6	950	833.4	555.6	740.8	500.0
20121029	6	35.3	-70.5	148.2	947	777.8	666.7	833.4	500.0
20121029	12	36.9	-71	157.4	945	777.8	777.8	740.8	500.0
20121029	18	38.3	-73.2	148.2	940	777.8	777.8	740.8	777.8
20121030	0	39.5	-74.5	129.6	946	851.9	685.2	740.8	907.5
20121030	6	39.9	-76.2	101.9	960	833.4	740.8	296.3	981.6
20121030	12	40.1	-77.8	92.6	978	833.4	907.5	0.0	926.0
20121030	18	40.4	-78.9	74.1	986	0.0	981.6	0.0	796.4
20121031	0	40.7	-79.8	64.8	992	0.0	0.0	0.0	759.3
20121031	6	41.1	-80.3	64.8	993	0.0	0.0	0.0	703.8
20121031	12	41.5	-80.7	55.6	995	0.0	0.0	0.0	0.0
					_				-

Humberto Maximum 63km/h 63km/h 63km/h Minimum 63km/h Latitude Longitude **Sustained Wind** Wind NE Wind SE Wind SW Wind NW **Date** Hour **Pressure** Speed (km/h) Radii (km) Radii (km) (mbar) Radii (km) Radii (km) 13 20130908 0 -17.6 46.3 1009 0.0 0.0 0.0 0.0 20130908 6 13 -18.4 46.3 1009 0.0 0.0 0.0 0.0 20130908 0.0 0.0 12 13 -19.3 46.3 1009 0.0 0.0 0.0 20130908 18 13 -20.3 46.3 1008 0.0 0.0 0.0 13.1 1007 0.0 20130909 -21.3 55.6 0.0 0.0 0.0 0 20130909 13.3 -22.4 64.8 1006 0.0 0.0 74.1 111.1 6 20130909 12 13.5 -23.6 74.1 1005 111.1 0.0 74.1 111.1 20130909 18 13.7 -24.6 83.3 1004 148.2 74.1 74.1 111.1 20130910 13.9 -25.5 92.6 1002 74.1 0 166.7 111.1 111.1 20130910 185.2 148.2 129.6 6 14.1 -26.5 101.9 1000 92.6

20130711	U	15.1	20.3	101.7	770	222.2	100.7	111.1	100.7
20130911	6	15.6	-28.6	111.1	994	222.2	185.2	111.1	166.7
20130911	12	16.3	-28.9	129.6	987	222.2	185.2	111.1	166.7
20130911	18	17.4	-28.9	148.2	979	222.2	185.2	111.1	166.7
20130912	0	18.6	-28.9	148.2	979	240.8	222.2	129.6	185.2
20130912	6	19.9	-28.9	148.2	979	259.3	240.8	129.6	240.8
20130912	12	21.2	-28.9	138.9	980	277.8	259.3	129.6	296.3
20130912	18	22.3	-29.1	138.9	980	296.3	277.8	148.2	296.3
20130913	0	23.2	-29.5	129.6	982	333.4	296.3	166.7	296.3
20130913	6	24	-30	111.1	986	370.4	296.3	185.2	296.3
20130913	12	24.6	-30.8	101.9	988	370.4	296.3	203.7	296.3
20130913	18	24.8	-31.7	83.3	995	333.4	259.3	185.2	296.3
20130914	0	24.8	-32.6	74.1	999	333.4	222.2	148.2	259.3
20130914	6	24.9	-33.6	64.8	1003	333.4	0.0	0.0	222.2
20130914	12	25.2	-34.8	64.8	1004	333.4	0.0	0.0	222.2
20130914	18	25.5	-36.3	64.8	1005	333.4	0.0	0.0	222.2
20130915	0	25.6	-37.8	64.8	1004	333.4	0.0	0.0	222.2
20130915	6	25.6	-38.9	64.8	1004	351.9	0.0	0.0	222.2
20130915	12	25.9	-39.7	64.8	1004	370.4	0.0	0.0	222.2
20130915	18	26.4	-40.4	64.8	1004	370.4	0.0	0.0	222.2
20130916	0	26.7	-41.3	64.8	1004	370.4	0.0	0.0	222.2
20130916	6	26.7	-42.4	64.8	1004	351.9	0.0	0.0	203.7

74.1

74.1

64.8

1000

1000

1002

101.9

101.9

101.9

1000

999

998

185.2

203.7

222.2

333.4

314.8

296.3

148.2

148.2

166.7

0.0

0.0

0.0

92.6

92.6

111.1

0.0

0.0

0.0

185.2

166.7

0.0

148.2

148.2

166.7

20130910

20130910

20130911

20130916

20130916

20130917

12

18

0

26.8

26.9

27

-42.9

-43.3

-43.2

12

18

0

14.3

14.7

15.1

-27.3

-27.9

-28.3

ь	_
٠.	
-	\rightarrow
ŕ	7
•	٠,

20130917	6	27.4	-42.9	64.8	1002	259.3	222.2	0.0	0.0
20130917	12	28.4	-42.6	74.1	1000	222.2	222.2	0.0	0.0
20130917	18	29.5	-42.7	74.1	1000	222.2	0.0	0.0	0.0
20130918	0	30.5	-43.2	64.8	1003	222.2	0.0	0.0	0.0
20130918	6	31.1	-43.6	55.6	1006	0.0	0.0	0.0	0.0
20130918	12	31.6	-43.9	55.6	1006	0.0	0.0	0.0	0.0
20130918	18	32	-44.1	55.6	1007	0.0	0.0	0.0	0.0
20130919	0	32.5	-44.3	55.6	1007	0.0	0.0	0.0	0.0
20130919	6	33	-44.5	55.6	1007	0.0	0.0	0.0	0.0

Arthur

			1						
				Maximum	Minimum	63km/h	63km/h	63km/h	63km/h
Date	Hour	Latitude	Longitude	Sustained Wind	Pressure	Wind NE	Wind SE	Wind SW	Wind NW
				Speed (km/h)	(mbar)	Radii (km)	Radii (km)	Radii (km)	Radii (km)
20140628	18	32	-78.2	37.0	1017	0.0	0.0	0.0	0.0
20140629	0	31.2	-77.8	37.0	1017	0.0	0.0	0.0	0.0
20140629	6	30.5	-77.4	37.0	1017	0.0	0.0	0.0	0.0
20140629	12	30	-77.2	37.0	1016	0.0	0.0	0.0	0.0
20140629	18	29.7	-77.2	46.3	1015	0.0	0.0	0.0	0.0
20140630	0	29.5	-77.5	46.3	1014	0.0	0.0	0.0	0.0
20140630	6	29.2	-78	46.3	1013	0.0	0.0	0.0	0.0
20140630	12	28.7	-78.4	46.3	1011	0.0	0.0	0.0	0.0
20140630	18	28.1	-78.7	55.6	1010	0.0	0.0	0.0	0.0
20140701	0	27.7	-78.9	55.6	1008	0.0	0.0	0.0	0.0
20140701	6	27.5	-79.1	55.6	1007	0.0	0.0	0.0	0.0
20140701	12	27.5	-79.2	64.8	1005	0.0	74.1	74.1	0.0
20140701	18	27.7	-79.3	74.1	1003	74.1	111.1	92.6	74.1
20140702	0	27.9	-79.2	83.3	999	111.1	129.6	92.6	74.1

1
' K
┺
٠,
\sim

20140702	6	28.2	-79.1	92.6	995	111.1	129.6	92.6	74.1
20140702	12	28.7	-79	101.9	995	111.1	129.6	92.6	74.1
20140702	18	29.4	-79.1	111.1	994	129.6	129.6	111.1	92.6
20140703	0	30.1	-79.2	120.4	987	129.6	148.2	111.1	92.6
20140703	6	30.9	-79.1	129.6	984	129.6	148.2	111.1	92.6
20140703	12	31.8	-78.8	148.2	981	185.2	185.2	111.1	92.6
20140703	18	32.9	-78.3	148.2	978	203.7	240.8	148.2	111.1
20140704	0	34	-77.3	157.4	975	203.7	240.8	148.2	111.1
20140704	3.15	34.7	-76.6	157.4	973	203.7	240.8	148.2	111.1
20140704	6	35.3	-76	157.4	972	185.2	203.7	166.7	74.1
20140704	8	35.8	-75.5	157.4	973	185.2	203.7	166.7	74.1
20140704	12	36.8	-74.4	148.2	976	185.2	203.7	166.7	111.1
20140704	18	38.4	-72.4	129.6	978	222.2	259.3	185.2	129.6
20140705	0	40.2	-69.7	120.4	976	222.2	259.3	185.2	129.6
20140705	6	42.3	-67.6	111.1	981	222.2	259.3	185.2	129.6
20140705	12	44.1	-66.5	111.1	982	259.3	333.4	259.3	129.6
20140705	18	45.9	-65.3	101.9	980	388.9	333.4	407.4	185.2
20140706	0	47.1	-64	92.6	981	166.7	203.7	333.4	333.4
20140706	6	47.6	-62.4	83.3	982	166.7	370.4	0.0	0.0
20140706	12	48.5	-60.2	74.1	986	0.0	277.8	0.0	0.0
20140706	18	50.3	-58.1	64.8	989	0.0	333.4	0.0	0.0
20140707	0	52.3	-56.4	64.8	988	0.0	444.5	0.0	0.0
20140707	6	54.2	-55.4	64.8	985	0.0	444.5	0.0	0.0
20140707	12	56	-54.7	64.8	984	592.6	444.5	0.0	0.0
20140707	18	57.3	-54.2	74.1	985	592.6	444.5	296.3	0.0
20140708	0	58.1	-54.1	83.3	988	592.6	370.4	277.8	0.0
20140708	6	58.9	-54.7	74.1	991	592.6	333.4	222.2	0.0

20140708	12	59.4	-56.1	64.8	993	592.6	0.0	0.0	0.0
20140708	18	60	-57	55.6	995	0.0	0.0	0.0	0.0
20140709	0	60.3	-56.7	55.6	997	0.0	0.0	0.0	0.0
20140709	6	60.1	-56.2	46.3	1001	0.0	0.0	0.0	0.0
20140709	12	59.8	-55.7	46.3	1005	0.0	0.0	0.0	0.0
20140709	18	59.5	-55	46.3	1008	0.0	0.0	0.0	0.0

Bertha

Date	Hour	Latitude	Longitude	Maximum Sustained Wind Speed (km/h)	Minimum Pressure (mbar)	63km/h Wind NE Radii (km)	63km/h Wind SE Radii (km)	63km/h Wind SW Radii (km)	63km/h Wind NW Radii (km)
20140729	6	9.6	-37.1	46.3	1013	0.0	0.0	0.0	0.0
20140729	12	9.5	-38.6	55.6	1012	0.0	0.0	0.0	0.0
20140729	18	9.5	-40.1	55.6	1012	0.0	0.0	0.0	0.0
20140730	0	9.6	-41.5	55.6	1012	0.0	0.0	0.0	0.0
20140730	6	9.7	-43	55.6	1012	0.0	0.0	0.0	0.0
20140730	12	9.8	-44.7	55.6	1012	0.0	0.0	0.0	0.0
20140730	18	10	-46.4	55.6	1011	0.0	0.0	0.0	0.0
20140731	0	10.4	-48	64.8	1010	74.1	74.1	0.0	74.1
20140731	6	10.7	-49.7	64.8	1009	74.1	74.1	0.0	74.1
20140731	12	11	-51.4	74.1	1008	74.1	74.1	0.0	74.1
20140731	18	11.5	-53.1	74.1	1007	74.1	74.1	0.0	74.1
20140801	0	12.2	-54.6	74.1	1007	74.1	74.1	0.0	74.1
20140801	6	13	-56.2	74.1	1007	74.1	74.1	0.0	74.1
20140801	12	13.8	-58.1	83.3	1006	129.6	74.1	0.0	74.1
20140801	18	14.5	-60.3	83.3	1006	185.2	74.1	0.0	74.1
20140802	0	15.2	-62.3	83.3	1007	185.2	55.6	0.0	74.1
20140802	6	15.9	-64.1	74.1	1008	185.2	55.6	0.0	74.1

۲	_
-	4
\	9

20140802	12	16.7	-65.9	74.1	1009	185.2	55.6	0.0	74.1
20140802	18	17.9	-67.6	74.1	1010	222.2	74.1	0.0	74.1
20140803	0	19.2	-69	74.1	1011	259.3	129.6	0.0	74.1
20140803	6	20.3	-70.4	74.1	1012	259.3	185.2	0.0	92.6
20140803	12	21.4	-71.6	74.1	1013	259.3	185.2	0.0	92.6
20140803	14	21.8	-71.9	74.1	1013	259.3	185.2	0.0	92.6
20140803	18	22.7	-72.5	83.3	1012	259.3	185.2	0.0	92.6
20140804	0	24.1	-73.1	101.9	1007	259.3	185.2	0.0	74.1
20140804	6	25.4	-73.5	111.1	1004	259.3	185.2	0.0	74.1
20140804	12	26.8	-73.6	129.6	998	259.3	185.2	55.6	74.1
20140804	18	28.5	-73.6	129.6	999	222.2	185.2	55.6	74.1
20140805	0	30.5	-73.4	120.4	1001	203.7	185.2	55.6	55.6
20140805	6	32.5	-73.2	101.9	1003	203.7	185.2	55.6	55.6
20140805	12	34.2	-72.7	92.6	1005	222.2	185.2	0.0	0.0
20140805	18	35.5	-71.2	83.3	1006	222.2	222.2	0.0	0.0
20140806	0	36.8	-69.3	83.3	1007	222.2	222.2	0.0	0.0
20140806	6	38.1	-66.9	83.3	1007	185.2	222.2	0.0	0.0
20140806	12	39.4	-64.1	83.3	1006	185.2	222.2	0.0	0.0
20140806	18	40.8	-61.3	83.3	1002	185.2	259.3	0.0	0.0
20140807	0	42.1	-58.4	92.6	996	55.6	259.3	111.1	55.6
20140807	6	43.4	-55.6	83.3	998	55.6	259.3	111.1	55.6
20140807	12	44.6	-52.5	74.1	999	0.0	259.3	111.1	0.0
20140807	18	46	-49.5	74.1	1000	0.0	259.3	111.1	0.0
20140808	0	47.4	-46.6	64.8	1001	0.0	259.3	0.0	0.0
20140808	6	47.9	-43	64.8	1001	0.0	259.3	0.0	0.0
20140808	12	47.5	-39.4	64.8	1002	0.0	259.3	0.0	0.0
20140808	18	46.9	-34.9	64.8	1002	0.0	259.3	0.0	0.0

۲		
(J	h

20140828

20140828

6

12

34.8

36.3

-69

-67.1

20140809	0	47	-29	64.8	1003	0.0	259.3	0.0	0.0
20140809	6	47.1	-22	64.8	1003	0.0	259.3	0.0	0.0
20140809	12	47.5	-15	64.8	1003	0.0	259.3	0.0	0.0
				C	Cristobal				
Maximum Minir						63km/h	63km/h	63km/h	63km/h
Date	Hour	Latitude	Longitude	Sustained Wind	Pressure	Wind NE	Wind SE	Wind SW	Wind NW
				Speed (km/h)	(mbar)	Radii (km)	Radii (km)	Radii (km)	Radii (km)
20140823	18	21.5	-72.2	55.6	1005	0.0	0.0	0.0	0.0
20140824	0	22	-72.5	55.6	1004	0.0	0.0	0.0	0.0
20140824	6	22.6	-72.9	64.8	1002	111.1	111.1	0.0	0.0
20140824	12	23.3	-73	74.1	1001	111.1	129.6	0.0	0.0
20140824	18	24	-73	83.3	1001	111.1	129.6	0.0	0.0
20140825	0	24.2	-73	83.3	998	111.1	148.2	0.0	0.0
20140825	6	24.4	-72.9	83.3	996	111.1	222.2	0.0	0.0
20140825	12	24.7	-72.7	92.6	993	111.1	222.2	0.0	0.0
20140825	18	24.9	-72.4	92.6	992	111.1	333.4	0.0	0.0
20140826	0	25.1	-72.1	120.4	989	111.1	333.4	111.1	55.6
20140826	6	25.6	-72	120.4	989	148.2	333.4	111.1	55.6
20140826	12	26.7	-71.8	120.4	988	148.2	333.4	111.1	55.6
20140826	18	28.1	-71.4	120.4	987	333.4	388.9	111.1	111.1
20140827	0	29.5	-71.5	129.6	983	333.4	388.9	111.1	185.2
20140827	6	30.6	-72	129.6	983	333.4	333.4	111.1	185.2
20140827	12	31.6	-72.2	129.6	983	333.4	333.4	111.1	185.2
20140827	18	32.3	-71.8	120.4	984	333.4	333.4	111.1	129.6
20140828	0	33.5	-70.7	120.4	984	333.4	333.4	111.1	129.6

120.4

129.6

982

979

333.4

333.4

333.4

333.4

111.1

111.1

129.6

129.6

ь	_
-	
Ć	л
Ľ	

20140830	18	54	-32	111.1	971	444.5	555.6 555.6	666.7	370.4
20140831	0	58	-28.9	111.1	971	444.5	555.6	666.7	370.4
20140831	6	61	-27	111.1	963	370.4	500.0	444.5	370.4
20140831	12	62	-26	111.1	964	370.4	500.0	444.5	370.4
20140831	18	63	-24.5	101.9	968	370.4	500.0	444.5	370.4
20140901	0	64	-22	92.6	974	370.4	500.0	444.5	370.4
20140901	6	65	-19.5	92.6	978	370.4	500.0	444.5	370.4
20140901	12	66	-17	83.3	980	0.0	370.4	370.4	370.4
20140901	18	67	-15.4	83.3	982	0.0	370.4	370.4	370.4
20140902	0	68	-15	74.1	984	0.0	370.4	370.4	370.4
20140902	6	69	-15	64.8	985	0.0	370.4	370.4	370.4
				(Gonzalo				
				Maximum	Minimum	63km/h	63km/h	63km/h	63km/h
	Hour	Latitude	Longitude	Sustained Wind	Pressure	Wind NE	Wind SE	Wind SW	Wind NW
Date	11041		I	0 10 0	(mbar)	Radii (km)	Radii (km)	Radii (km)	Radii (km)
Date		_	_	Speed (km/h)	(IIIDar)	Kaun (Kin)	114411 (11111)	144411 (11111)	readii (iiiii)
Date 20141011	18	16.4	-54.9	Speed (km/h) 46.3	1010	0.0	0.0	0.0	0.0
		16.4 16.4	-54.9 -55.9	. /	` /	` ′	` /	` /	` /
20141011	18			46.3	1010	0.0	0.0	0.0	0.0

			1	1					1
20141012	18	16.4	-58.8	74.1	1004	92.6	74.1	0.0	92.6
20141013	0	16.5	-59.7	83.3	1001	92.6	74.1	0.0	92.6
20141013	6	16.7	-60.6	101.9	996	111.1	74.1	37.0	111.1
20141013	12	17	-61.5	120.4	992	148.2	92.6	55.6	148.2
20141013	18	17.6	-62.4	129.6	988	166.7	111.1	74.1	166.7
20141014	0	18.3	-63.2	148.2	983	166.7	111.1	92.6	166.7
20141014	6	19.1	-64	166.7	976	166.7	111.1	92.6	166.7
20141014	12	19.9	-64.8	175.9	973	166.7	111.1	92.6	166.7
20141014	18	20.8	-65.5	185.2	968	166.7	111.1	92.6	166.7
20141015	0	21.7	-66.2	213.0	956	185.2	111.1	129.6	185.2
20141015	6	22.5	-67	213.0	953	185.2	111.1	129.6	185.2
20141015	12	23.1	-67.7	213.0	949	203.7	148.2	148.2	203.7
20141015	18	23.8	-68.3	203.7	953	203.7	148.2	148.2	203.7
20141016	0	24.4	-68.6	203.7	953	203.7	166.7	166.7	203.7
20141016	6	25	-68.7	213.0	948	222.2	203.7	166.7	203.7
20141016	12	25.6	-68.7	231.5	940	240.8	240.8	166.7	203.7
20141016	18	26.5	-68.3	231.5	942	240.8	240.8	166.7	203.7
20141017	0	27.4	-67.8	222.2	942	259.3	277.8	203.7	203.7
20141017	6	28.6	-67.2	213.0	945	259.3	277.8	203.7	203.7
20141017	12	29.8	-66.5	203.7	947	259.3	277.8	203.7	203.7
20141017	18	31	-65.7	194.5	949	259.3	277.8	203.7	203.7
20141018	0	32.2	-64.9	175.9	952	259.3	277.8	203.7	203.7
20141018	6	33.7	-63.9	166.7	955	259.3	277.8	203.7	203.7
20141018	12	35.6	-62.6	157.4	960	277.8	333.4	259.3	185.2
20141018	18	38.2	-60.9	157.4	964	333.4	407.4	296.3	185.2
20141019	0	41.2	-58.3	157.4	965	333.4	500.0	333.4	166.7
20141019	6	44.5	-54.8	148.2	968	333.4	500.0	333.4	166.7

20141019 20141019	18	47.8 50.6	-50.1 -44.8	129.6 120.4	970 976	333.4 333.4	500.0 500.0	333.4 444.5	166.7 148.2
20141020	0	52.6	-38.3	101.9	982	333.4	592.6	555.6	0.0
20141020	6	53.9	-30.9	92.6	988	333.4	592.6	555.6	0.0
					_				

Danny

				Maximum	Minimum	63km/h	63km/h	63km/h	63km/h
Date	Hour	Latitude	Longitude	Sustained Wind	Pressure	Wind NE	Wind SE	Wind SW	Wind NW
				Speed (km/h)	(mbar)	Radii (km)	Radii (km)	Radii (km)	Radii (km)
20150817	0	9.6	-29.3	46.3	1011	0.0	0.0	0.0	0.0
20150817	6	9.6	-30.4	46.3	1011	0.0	0.0	0.0	0.0
20150817	12	9.7	-31.5	46.3	1011	0.0	0.0	0.0	0.0
20150817	18	10	-32.6	46.3	1010	0.0	0.0	0.0	0.0
20150818	0	10.3	-33.7	46.3	1010	0.0	0.0	0.0	0.0
20150818	6	10.4	-34.8	55.6	1009	0.0	0.0	0.0	0.0
20150818	12	10.5	-35.9	64.8	1008	74.1	0.0	0.0	74.1
20150818	18	10.7	-37.1	74.1	1006	74.1	55.6	0.0	74.1
20150819	0	10.9	-38.4	83.3	1005	92.6	55.6	0.0	74.1
20150819	6	11	-39.5	83.3	1003	92.6	55.6	0.0	74.1
20150819	12	11.2	-40.6	83.3	1002	92.6	55.6	55.6	74.1
20150819	18	11.5	-41.5	92.6	1001	92.6	55.6	37.0	74.1
20150820	0	11.7	-42.5	101.9	1000	92.6	55.6	37.0	74.1
20150820	6	11.9	-43.5	111.1	998	92.6	55.6	37.0	74.1
20150820	12	12.3	-44.4	120.4	995	92.6	55.6	55.6	74.1
20150820	18	12.8	-45.3	138.9	990	92.6	55.6	55.6	74.1
20150821	0	13.2	-46.2	157.4	981	92.6	55.6	55.6	74.1
20150821	6	13.5	-47	175.9	973	92.6	55.6	55.6	74.1
20150821	12	13.8	-47.8	203.7	960	92.6	55.6	55.6	92.6

_	
7	_
4	וע
_	Δ

				Maximum	Minimum	63km/h	63km/h	63km/h	63km/h	
Fred										
20150824	12	15.8	-61.3	55.6	1009	0.0	0.0	0.0	0.0	
20150824	6	15.8	-60.4	64.8	1008	92.6	55.6	0.0	0.0	
20150824	0	15.6	-59.3	74.1	1007	92.6	55.6	0.0	0.0	
20150823	18	15.6	-58.2	74.1	1004	92.6	55.6	0.0	74.1	
20150823	12	15.7	-56.7	83.3	1002	92.6	55.6	37.0	74.1	
20150823	6	15.7	-55.3	92.6	1001	92.6	55.6	37.0	92.6	
20150823	0	15.6	-54	101.9	999	92.6	55.6	37.0	92.6	
20150822	18	15.5	-52.7	120.4	990	92.6	55.6	55.6	92.6	
20150822	12	15.3	-51.4	138.9	985	92.6	55.6	55.6	92.6	
20150822	6	15	-50.3	157.4	980	92.6	55.6	55.6	92.6	
20150822	0	14.7	-49.4	175.9	973	92.6	55.6	55.6	92.6	
20150821	18	14.3	-48.6	194.5	966	92.6	55.6	55.6	92.6	

Date	Hour	Latitude	Longitude	Maximum Sustained Wind	Minimum Pressure	63km/h Wind NE	63km/h Wind SE	63km/h Wind SW	63km/h Wind NW
				Speed (km/h)	(mbar)	Radii (km)	Radii (km)	Radii (km)	Radii (km)
20150830	0	11.6	-17.5	55.6	1007	0.0	0.0	0.0	0.0
20150830	6	12.2	-18.4	64.8	1005	55.6	55.6	0.0	55.6
20150830	12	13.1	-19.5	83.3	1004	92.6	92.6	0.0	55.6
20150830	18	14	-20.7	101.9	998	111.1	111.1	55.6	92.6
20150831	0	14.6	-21.7	120.4	992	129.6	129.6	92.6	111.1
20150831	6	15.3	-22.5	129.6	989	129.6	129.6	92.6	111.1
20150831	12	16.1	-23.3	138.9	986	129.6	129.6	92.6	111.1
20150831	18	16.8	-24.1	129.6	988	129.6	129.6	92.6	111.1
20150901	0	17.4	-24.9	120.4	991	129.6	129.6	92.6	111.1
20150901	6	17.8	-25.7	111.1	994	129.6	129.6	74.1	111.1
20150901	12	18.2	-26.7	92.6	1000	129.6	74.1	74.1	129.6

۰	_
(
C	-

	1	Ī	ı	I			ı		1
20150901	18	18.7	-27.6	83.3	1003	129.6	74.1	74.1	129.6
20150902	0	19.1	-28.7	83.3	1003	129.6	74.1	74.1	129.6
20150902	6	19.3	-29.7	74.1	1004	129.6	74.1	74.1	129.6
20150902	12	19.6	-30.5	74.1	1005	111.1	74.1	0.0	92.6
20150902	18	20	-31.4	64.8	1006	111.1	55.6	0.0	92.6
20150903	0	20.4	-32.2	64.8	1006	111.1	55.6	0.0	92.6
20150903	6	20.7	-32.9	74.1	1005	111.1	74.1	0.0	74.1
20150903	12	21.3	-33.7	74.1	1005	111.1	74.1	0.0	74.1
20150903	18	21.8	-34.9	64.8	1005	111.1	74.1	0.0	74.1
20150904	0	21.9	-36	64.8	1005	111.1	74.1	0.0	74.1
20150904	6	22	-36.9	64.8	1005	111.1	74.1	0.0	74.1
20150904	12	22.2	-37.9	55.6	1005	0.0	0.0	0.0	0.0
20150904	18	22.4	-38.7	55.6	1006	0.0	0.0	0.0	0.0
20150905	0	22.7	-39.6	64.8	1006	55.6	0.0	0.0	0.0
20150905	6	23	-40.6	64.8	1007	55.6	0.0	0.0	0.0
20150905	12	23.3	-41.5	55.6	1008	0.0	0.0	0.0	0.0
20150905	18	23.5	-42.2	55.6	1008	0.0	0.0	0.0	0.0
20150906	0	23.8	-42.9	55.6	1009	0.0	0.0	0.0	0.0
20150906	6	24.5	-43.3	55.6	1010	0.0	0.0	0.0	0.0
20150906	12	25.3	-43.2	46.3	1010	0.0	0.0	0.0	0.0
				J	Joaquin				
				Maximum	Minimum	63km/h	63km/h	63km/h	63km/h
Date	Hour	Latitude	Longitude	Sustained Wind	Pressure	Wind NE	Wind SE	Wind SW	Wind NW
				Speed (km/h)	(mbar)	Radii (km)	Radii (km)	Radii (km)	Radii (km)
20150926	18	26.8	-68.7	37.0	1011	0.0	0.0	0.0	0.0
20150927	0	26.9	-68.6	37.0	1011	0.0	0.0	0.0	0.0
20150927	6	27	-68.5	37.0	1010	0.0	0.0	0.0	0.0

20150927	12	27.1	-68.6	46.3	1009	0.0	0.0	0.0	0.0
20150927	18	27.2	-68.8	55.6	1007	0.0	0.0	0.0	0.0
20150928	0	27.4	-69	55.6	1007	0.0	0.0	0.0	0.0
20150928	6	27.6	-69.3	55.6	1007	0.0	0.0	0.0	0.0
20150928	12	27.7	-69.7	55.6	1006	0.0	0.0	0.0	0.0
20150928	18	27.4	-70	55.6	1003	0.0	0.0	0.0	0.0
20150929	0	26.9	-70.1	64.8	1002	0.0	111.1	0.0	0.0
20150929	6	26.5	-70.3	64.8	1002	0.0	111.1	0.0	0.0
20150929	12	26.2	-70.5	83.3	999	0.0	129.6	0.0	0.0
20150929	18	26	-70.8	101.9	992	111.1	148.2	0.0	0.0
20150930	0	25.8	-71.3	111.1	985	129.6	148.2	55.6	55.6
20150930	6	25.4	-71.8	120.4	978	148.2	166.7	74.1	74.1
20150930	12	24.9	-72.2	129.6	971	166.7	203.7	111.1	111.1
20150930	18	24.4	-72.5	148.2	961	185.2	222.2	148.2	148.2
20151001	0	23.9	-72.9	185.2	951	185.2	240.8	166.7	166.7
20151001	6	23.5	-73.3	203.7	947	203.7	259.3	185.2	185.2
20151001	12	23.1	-73.7	213.0	942	203.7	277.8	222.2	203.7
20151001	18	23	-74.2	213.0	936	203.7	296.3	240.8	203.7
20151002	0	22.9	-74.4	222.2	931	222.2	314.8	240.8	222.2
20151002	6	23	-74.7	222.2	935	222.2	333.4	259.3	222.2
20151002	12	23.4	-74.8	213.0	937	240.8	333.4	259.3	222.2
20151002	16	23.6	-74.8	203.7	940	240.8	333.4	259.3	222.2
20151002	18	23.8	-74.7	203.7	941	259.3	333.4	259.3	222.2
20151002	21	24.1	-74.5	203.7	942	259.3	333.4	259.3	222.2
20151003	0	24.3	-74.3	213.0	943	259.3	333.4	259.3	222.2
20151003	6	24.8	-73.6	222.2	945	277.8	333.4	259.3	222.2
20151003	12	25.4	-72.6	250.0	934	277.8	333.4	240.8	203.7

Ċ	7	
	٠;	

20151003	18	26.3	-71	240.8	934	296.3	333.4	240.8	203.7
20151004	0	27.4	-69.5	213.0	941	296.3	333.4	240.8	203.7
20151004	6	28.9	-68.3	194.5	949	296.3	333.4	222.2	203.7
20151004	12	30.4	-67.2	175.9	956	296.3	314.8	222.2	203.7
20151004	18	31.6	-66.5	157.4	958	314.8	314.8	222.2	203.7
20151005	0	32.6	-66	138.9	961	314.8	314.8	240.8	222.2
20151005	6	33.6	-65.6	138.9	964	314.8	314.8	240.8	222.2
20151005	12	34.4	-65.2	138.9	964	314.8	314.8	259.3	240.8
20151005	18	35.3	-64.5	138.9	964	314.8	314.8	277.8	240.8
20151006	0	36.2	-63.6	138.9	967	296.3	333.4	296.3	259.3
20151006	6	37	-62.3	138.9	970	296.3	333.4	314.8	277.8
20151006	12	37.9	-60.4	129.6	974	296.3	351.9	351.9	277.8
20151006	18	38.8	-58	129.6	974	296.3	351.9	370.4	277.8
20151007	0	39.6	-54.9	129.6	974	296.3	370.4	407.4	296.3
20151007	6	40.3	-51.5	120.4	977	296.3	388.9	426.0	296.3
20151007	12	41	-47.5	111.1	977	296.3	426.0	463.0	296.3
20151007	18	41.5	-43.3	111.1	977	296.3	444.5	481.5	296.3
20151008	0	41.9	-39.1	101.9	977	296.3	463.0	500.0	277.8
20151008	6	42.4	-35	92.6	977	314.8	481.5	500.0	259.3
20151008	12	43	-31	83.3	980	333.4	500.0	518.6	259.3
20151008	18	43.5	-27.3	83.3	984	333.4	518.6	500.0	259.3
20151009	0	43.9	-24.1	83.3	987	351.9	518.6	500.0	240.8
20151009	6	44.1	-21.9	83.3	988	351.9	537.1	463.0	240.8
20151009	12	44.2	-19.9	83.3	988	370.4	518.6	426.0	259.3
20151009	18	44.1	-18.2	74.1	989	370.4	500.0	388.9	296.3
20151010	0	43.8	-16.4	64.8	992	370.4	481.5	370.4	370.4
20151010	6	43.4	-15	64.8	993	370.4	426.0	444.5	444.5

1
S
∞

20151010	1.0	10.1	100		00.5	222 1	250 1	0.0	0.0
20151010	12	43.1	-13.9	64.8	996	333.4	370.4	0.0	0.0
20151010	18	42.8	-12.9	55.6	998	0.0	0.0	0.0	0.0
20151011	0	42.5	-12	55.6	999	0.0	0.0	0.0	0.0
20151011	6	42.2	-11.3	55.6	1000	0.0	0.0	0.0	0.0
20151011	12	41.8	-10.8	64.8	1001	0.0	0.0	0.0	222.2
20151011	18	41.2	-10.5	64.8	1001	0.0	0.0	259.3	259.3
20151012	0	40.4	-10.2	64.8	1002	0.0	0.0	222.2	259.3
20151012	6	39.8	-9.7	64.8	1002	0.0	0.0	222.2	259.3
20151012	12	39.5	-9.1	64.8	1003	0.0	0.0	222.2	259.3
20151012	18	39.1	-8.8	55.6	1005	0.0	0.0	0.0	0.0
20151013	0	38.6	-8.9	46.3	1007	0.0	0.0	0.0	0.0
20151013	6	38	-9.1	37.0	1009	0.0	0.0	0.0	0.0
20151013	12	37.3	-9.2	37.0	1010	0.0	0.0	0.0	0.0
20151013	18	36.6	-9.1	37.0	1010	0.0	0.0	0.0	0.0
20151014	0	36	-9	37.0	1011	0.0	0.0	0.0	0.0
20151014	6	35.5	-8.7	37.0	1011	0.0	0.0	0.0	0.0
20151014	12	35.1	-8.4	37.0	1011	0.0	0.0	0.0	0.0
20151014	18	35	-8	27.8	1012	0.0	0.0	0.0	0.0
20151015	0	35.2	-7.7	27.8	1012	0.0	0.0	0.0	0.0
					Kate				
				Maximum	Minimum	63km/h	63km/h	63km/h	63km/h
Date	Hour	Latitude	Longitude	Sustained Wind	Pressure	Wind NE	Wind SE	Wind SW	Wind NW
				Speed (km/h)	(mbar)	Radii (km)	Radii (km)	Radii (km)	Radii (km)
20151108	18	22.2	-71.5	55.6	1010	0.0	0.0	0.0	0.0
20151109	0	22.8	-72.6	55.6	1010	0.0	0.0	0.0	0.0
20151109	6	23.4	-73.7	64.8	1010	92.6	0.0	0.0	55.6
20151109	12	24.1	-74.8	74.1	1008	111.1	0.0	0.0	55.6

L	
,	_
ì	~

20151109	18	25	-75.7	83.3	1008	129.6	0.0	0.0	55.6
20151110	0	26.4	-76.2	92.6	1006	129.6	92.6	0.0	37.0
20151110	6	28	-76.2	101.9	1003	129.6	92.6	37.0	37.0
20151110	12	29.5	-75.4	111.1	998	129.6	129.6	37.0	37.0
20151110	18	31.2	-74	111.1	993	129.6	129.6	37.0	37.0
20151111	0	33.1	-71.3	120.4	990	148.2	148.2	111.1	37.0
20151111	6	35.2	-67.6	129.6	985	148.2	185.2	185.2	37.0
20151111	12	36.2	-62.5	138.9	980	222.2	333.4	333.4	92.6
20151111	18	37.6	-58.2	120.4	980	277.8	370.4	333.4	111.1
20151112	0	38.9	-55	120.4	980	333.4	388.9	333.4	166.7
20151112	6	40	-52	120.4	980	407.4	407.4	333.4	222.2
20151112	12	41.3	-50.4	101.9	981	407.4	407.4	333.4	222.2
20151112	18	41.9	-49.9	101.9	983	407.4	407.4	333.4	222.2
20151113	0	41.5	-49.2	92.6	985	1000.1	963.0	370.4	407.4
20151113	6	40.8	-47.5	83.3	985	1148.2	851.9	333.4	407.4
20151113	12	40.7	-45.4	83.3	987	1314.9	740.8	277.8	407.4
					Alex				

	Alex										
				Maximum	Minimum	63km/h	63km/h	63km/h	63km/h		
Date	Hour	Latitude	Longitude	Sustained Wind	Pressure	Wind NE	Wind SE	Wind SW	Wind NW		
				Speed (km/h)	(mbar)	Radii (km)	Radii (km)	Radii (km)	Radii (km)		
20160107	0	26.6	-75.3	74.1	1010	277.8	0.0	277.8	314.8		
20160107	6	27.6	-74.7	83.3	1003	370.4	166.7	222.2	314.8		
20160107	12	28.7	-73.8	92.6	997	463.0	222.2	185.2	314.8		
20160107	18	30	-72.5	101.9	987	463.0	240.8	222.2	351.9		
20160108	0	31.4	-70.6	101.9	986	463.0	277.8	277.8	444.5		
20160108	6	32.4	-68.8	101.9	986	500.0	277.8	277.8	444.5		
20160108	12	33	-67.1	83.3	991	611.2	314.8	222.2	370.4		

۲		
c	7	١
2	_	

20160108	18	33.5	-65	83.3	991	740.8	370.4	222.2	370.4
20160109	0	34	-62.9	83.3	991	740.8	370.4	222.2	444.5
20160109	6	34.5	-60.5	92.6	991	740.8	277.8	222.2	555.6
20160109	12	35	-58.3	101.9	989	740.8	277.8	222.2	555.6
20160109	18	35.1	-56.1	111.1	985	740.8	370.4	222.2	444.5
20160110	0	34.4	-54.2	120.4	981	740.8	370.4	333.4	444.5
20160110	6	33.7	-52.7	120.4	981	740.8	370.4	388.9	444.5
20160110	12	32.9	-51.2	120.4	979	740.8	370.4	444.5	444.5
20160110	18	32.1	-49.1	111.1	980	740.8	370.4	444.5	555.6
20160111	0	31.6	-46.5	101.9	980	740.8	444.5	444.5	740.8
20160111	6	31.6	-44.6	101.9	980	740.8	444.5	444.5	740.8
20160111	12	31.3	-43.4	101.9	980	740.8	444.5	444.5	740.8
20160111	18	30	-42.5	92.6	982	740.8	222.2	444.5	740.8
20160112	0	28.4	-41.7	92.6	985	740.8	111.1	444.5	740.8
20160112	6	26.3	-40.2	92.6	988	518.6	111.1	444.5	740.8
20160112	12	25	-38	92.6	988	277.8	148.2	370.4	555.6
20160112	18	25.1	-35.9	92.6	988	185.2	185.2	185.2	185.2
20160113	0	25.4	-34.7	92.6	988	185.2	185.2	185.2	185.2
20160113	6	25.6	-33.6	83.3	989	129.6	185.2	148.2	111.1
20160113	12	26	-32.5	83.3	989	55.6	185.2	148.2	111.1
20160113	18	26.7	-31.4	83.3	990	111.1	222.2	222.2	0.0
20160114	0	27.9	-30.4	101.9	988	111.1	222.2	222.2	0.0
20160114	6	29.3	-29.6	120.4	985	222.2	240.8	185.2	55.6
20160114	12	30.8	-28.7	138.9	981	222.2	240.8	185.2	92.6
20160114	18	32.5	-28	138.9	981	277.8	277.8	185.2	185.2
20160115	0	33.9	-27.6	129.6	984	277.8	277.8	185.2	185.2
20160115	6	35.4	-27.2	120.4	986	500.0	277.8	185.2	185.2

۰	_
_	7
	٠,

20160115	12	38	-27	101.9	986	740.8	555.6	333.4	277.8
20160115	18	41.5	-27.7	101.9	986	777.8	777.8	444.5	222.2
20160116	0	45.1	-28.9	101.9	984	777.8	777.8	444.5	222.2
20160116	6	48.9	-30.2	101.9	982	777.8	777.8	444.5	222.2
20160116	12	53	-32	101.9	980	777.8	777.8	444.5	407.4
20160116	18	56	-37	101.9	979	777.8	444.5	444.5	777.8
20160117	0	57	-42	129.6	978	889.0	0.0	0.0	1111.2

Gaston

				Maximum	Minimum	63km/h	63km/h	63km/h	63km/h
Date	Hour	Latitude	Longitude	Sustained Wind	Pressure	Wind NE	Wind SE	Wind SW	Wind NW
				Speed (km/h)	(mbar)	Radii (km)	Radii (km)	Radii (km)	Radii (km)
20160821	12	11	-19.4	37.0	1009	0.0	0.0	0.0	0.0
20160821	18	11	-21.2	37.0	1009	0.0	0.0	0.0	0.0
20160822	0	11	-23	46.3	1009	0.0	0.0	0.0	0.0
20160822	6	11.2	-24.8	46.3	1009	0.0	0.0	0.0	0.0
20160822	12	11.5	-26.5	55.6	1008	0.0	0.0	0.0	0.0
20160822	18	12	-28.2	64.8	1007	92.6	55.6	55.6	55.6
20160823	0	12.5	-29.9	74.1	1006	92.6	55.6	55.6	55.6
20160823	6	13	-31.6	83.3	1005	92.6	74.1	55.6	92.6
20160823	12	13.5	-33.4	101.9	1003	111.1	74.1	55.6	111.1
20160823	18	13.9	-35	101.9	1003	111.1	74.1	55.6	111.1
20160824	0	14.2	-36.5	101.9	1000	111.1	74.1	55.6	111.1
20160824	6	14.8	-37.9	111.1	997	111.1	74.1	55.6	111.1
20160824	12	15.8	-39.1	120.4	992	166.7	166.7	74.1	111.1
20160824	18	16.9	-40.2	120.4	988	185.2	185.2	74.1	148.2
20160825	0	18	-41.4	120.4	988	185.2	185.2	74.1	185.2
20160825	6	18.9	-42.7	120.4	988	185.2	185.2	74.1	185.2

_	
5	
()	

20160825	12	19.8	-44	111.1	992	185.2	166.7	74.1	185.2
20160825	18	21	-45	101.9	996	185.2	148.2	55.6	185.2
20160826	0	22.3	-46	101.9	996	185.2	148.2	55.6	185.2
20160826	6	23.6	-47	101.9	996	203.7	148.2	55.6	185.2
20160826	12	24.8	-47.9	101.9	996	222.2	148.2	55.6	185.2
20160826	18	25.8	-49.1	101.9	996	222.2	148.2	55.6	185.2
20160827	0	26.7	-50.3	101.9	996	185.2	148.2	55.6	148.2
20160827	6	27.5	-51.5	101.9	996	185.2	148.2	55.6	148.2
20160827	12	28.1	-52.8	111.1	992	185.2	148.2	74.1	129.6
20160827	18	28.7	-53.6	120.4	989	222.2	166.7	92.6	129.6
20160828	0	29.3	-54.2	138.9	980	222.2	222.2	92.6	129.6
20160828	6	29.9	-54.5	148.2	976	222.2	222.2	92.6	148.2
20160828	12	30.3	-54.7	166.7	969	222.2	222.2	111.1	148.2
20160828	18	30.5	-55	185.2	962	222.2	222.2	148.2	148.2
20160829	0	30.6	-55.2	194.5	955	222.2	222.2	148.2	148.2
20160829	6	30.7	-55.3	185.2	960	222.2	222.2	148.2	148.2
20160829	12	30.8	-55.4	175.9	964	222.2	222.2	148.2	148.2
20160829	18	31.1	-55.4	166.7	967	222.2	222.2	148.2	148.2
20160830	0	31.4	-54.9	157.4	970	222.2	222.2	148.2	148.2
20160830	6	31.7	-54.4	157.4	970	222.2	222.2	148.2	148.2
20160830	12	32	-53.5	157.4	968	222.2	240.8	185.2	166.7
20160830	18	32.4	-52.5	175.9	963	222.2	259.3	185.2	166.7
20160831	0	32.7	-51.5	194.5	955	240.8	259.3	203.7	166.7
20160831	6	33.1	-50.5	194.5	955	240.8	259.3	222.2	166.7
20160831	12	33.7	-49.2	185.2	960	240.8	277.8	222.2	166.7
20160831	18	34.5	-47.9	175.9	965	240.8	277.8	222.2	166.7
20160901	0	35.5	-46.3	166.7	969	240.8	296.3	240.8	166.7

\vdash	_
	У
U	S

20160901	6	36.3	-44.3	157.4	973	240.8	296.3	259.3	166.7
20160901	12	37.1	-42	148.2	976	240.8	296.3	259.3	166.7
20160901	18	37.8	-39.5	138.9	981	240.8	296.3	259.3	166.7
20160902	0	38.2	-37	129.6	985	222.2	259.3	240.8	166.7
20160902	6	38.5	-35	120.4	988	222.2	240.8	203.7	129.6
20160902	12	38.9	-33	111.1	992	222.2	240.8	185.2	111.1
20160902	18	39.3	-31.2	83.3	1003	185.2	240.8	185.2	0.0
20160903	0	39.7	-29.5	64.8	1006	0.0	166.7	0.0	0.0
20160903	6	40.2	-27.8	55.6	1007	0.0	0.0	0.0	0.0
20160903	12	40.9	-26.1	46.3	1008	0.0	0.0	0.0	0.0

Matthew

				Maximum	Minimum	63km/h	63km/h	63km/h	63km/h
Date	Hour	Latitude	Longitude	Sustained Wind	Pressure	Wind NE	Wind SE	Wind SW	Wind NW
				Speed (km/h)	(mbar)	Radii (km)	Radii (km)	Radii (km)	Radii (km)
20160928	12	13.4	-59.8	92.6	1009	333.4	333.4	0.0	166.7
20160928	18	13.6	-61.2	92.6	1008	333.4	333.4	0.0	185.2
20160929	0	13.9	-62.6	101.9	1004	333.4	333.4	0.0	203.7
20160929	6	14	-64	101.9	1002	333.4	296.3	0.0	222.2
20160929	12	14.1	-65.5	111.1	995	333.4	259.3	92.6	240.8
20160929	18	14.2	-66.9	120.4	993	333.4	222.2	92.6	259.3
20160930	0	14.2	-68.1	129.6	987	314.8	222.2	92.6	277.8
20160930	6	14	-69.3	157.4	979	314.8	185.2	92.6	296.3
20160930	12	13.8	-70.4	185.2	968	314.8	166.7	92.6	314.8
20160930	18	13.5	-71.2	222.2	955	314.8	166.7	111.1	314.8
20161001	0	13.4	-71.9	268.5	942	314.8	166.7	111.1	314.8
20161001	6	13.4	-72.5	259.3	942	314.8	166.7	92.6	314.8
20161001	12	13.4	-73.1	250.0	944	314.8	166.7	111.1	314.8

1	7
4	4

20161001	18	13.4	-73.3	240.8	942	314.8	166.7	129.6	314.8
20161002	0	13.5	-73.5	240.8	940	314.8	166.7	129.6	296.3
20161002	6	13.7	-73.9	231.5	941	314.8	129.6	129.6	296.3
20161002	12	14	-74.3	240.8	947	314.8	148.2	129.6	277.8
20161002	18	14.2	-74.7	250.0	945	314.8	166.7	129.6	259.3
20161003	0	14.5	-75	240.8	944	314.8	185.2	148.2	240.8
20161003	6	14.9	-75	231.5	942	314.8	203.7	148.2	240.8
20161003	12	15.4	-75	231.5	941	314.8	222.2	148.2	222.2
20161003	18	15.9	-74.9	231.5	938	314.8	240.8	166.7	222.2
20161004	0	16.6	-74.6	240.8	934	314.8	259.3	166.7	203.7
20161004	6	17.5	-74.4	240.8	934	314.8	277.8	166.7	185.2
20161004	11	18.3	-74.3	240.8	935	314.8	277.8	166.7	185.2
20161004	12	18.4	-74.3	231.5	937	314.8	277.8	166.7	185.2
20161004	18	19.3	-74.3	222.2	947	296.3	277.8	166.7	185.2
20161005	0	20.1	-74.3	213.0	949	296.3	277.8	166.7	185.2
20161005	6	20.7	-74.4	203.7	960	296.3	259.3	166.7	166.7
20161005	12	21.4	-74.8	194.5	962	296.3	259.3	148.2	166.7
20161005	18	22.2	-75.4	194.5	963	296.3	259.3	129.6	166.7
20161006	0	23	-76	194.5	960	296.3	259.3	129.6	166.7
20161006	6	23.8	-76.7	203.7	952	296.3	259.3	129.6	166.7
20161006	12	24.7	-77.5	222.2	937	296.3	259.3	129.6	185.2
20161006	18	25.7	-78.3	222.2	937	296.3	259.3	148.2	203.7
20161007	0	26.7	-79	213.0	937	314.8	277.8	148.2	222.2
20161007	6	27.7	-79.7	203.7	939	314.8	277.8	148.2	222.2
20161007	12	28.9	-80.3	194.5	944	314.8	277.8	148.2	222.2
20161007	18	29.7	-80.7	185.2	946	314.8	277.8	148.2	222.2
20161008	0	30.7	-80.6	175.9	949	333.4	277.8	148.2	222.2

1
9
S

20161008	6	31.6	-80.6	157.4	953	333.4	296.3	166.7	240.8
20161008	9	32.1	-80.5	157.4	957	333.4	296.3	166.7	240.8
20161008	12	32.5	-79.9	148.2	963	351.9	296.3	166.7	259.3
20161008	15	33	-79.5	138.9	967	351.9	296.3	166.7	259.3
20161008	18	33.5	-79	129.6	973	351.9	314.8	185.2	277.8
20161009	0	33.9	-77.3	129.6	981	351.9	314.8	222.2	296.3
20161009	6	34.7	-76	129.6	983	370.4	314.8	277.8	314.8
20161009	12	35	-74.5	120.4	984	370.4	333.4	333.4	351.9
20161009	18	35.2	-72.8	111.1	987	388.9	333.4	333.4	388.9
20161010	0	35.3	-71.1	101.9	990	388.9	333.4	333.4	388.9

Nicole

				Maximum	Minimum	63km/h	63km/h	63km/h	63km/h
Date	Hour	Latitude	Longitude	Sustained Wind	Pressure	Wind NE	Wind SE	Wind SW	Wind NW
				Speed (km/h)	(mbar)	Radii (km)	Radii (km)	Radii (km)	Radii (km)
20161004	6	23.2	-59.8	64.8	1007	0.0	166.7	0.0	0.0
20161004	12	23.5	-60.3	74.1	1005	111.1	111.1	0.0	74.1
20161004	18	23.8	-60.7	83.3	1002	111.1	111.1	0.0	74.1
20161005	0	24.1	-61.2	83.3	1001	111.1	111.1	0.0	74.1
20161005	6	24.4	-61.7	83.3	1001	111.1	111.1	0.0	74.1
20161005	12	24.7	-62.5	83.3	1001	111.1	111.1	0.0	74.1
20161005	18	25.1	-63.3	92.6	1000	111.1	111.1	55.6	74.1
20161006	0	25.7	-63.9	92.6	999	111.1	111.1	55.6	74.1
20161006	6	26.2	-64.5	101.9	995	111.1	111.1	55.6	74.1
20161006	12	26.7	-64.8	111.1	991	111.1	111.1	55.6	74.1
20161006	18	27.3	-65.1	138.9	980	92.6	148.2	55.6	74.1
20161007	0	27.5	-65.2	166.7	969	92.6	148.2	92.6	92.6
20161007	6	27.6	-65.2	138.9	970	92.6	148.2	92.6	92.6

166	

20161007	12	27.6	-65.2	111.1	985	92.6	148.2	92.6	92.6
20161007	18	27.2	-65.3	101.9	992	92.6	148.2	92.6	92.6
20161008	0	26.6	-65.4	92.6	997	92.6	148.2	92.6	92.6
20161008	6	26	-65.5	74.1	1002	92.6	148.2	92.6	92.6
20161008	12	25.5	-65.6	74.1	1002	92.6	148.2	92.6	92.6
20161008	18	25	-65.7	83.3	1000	148.2	166.7	92.6	92.6
20161009	0	24.6	-65.6	83.3	999	148.2	166.7	92.6	74.1
20161009	6	24.1	-65.5	101.9	996	148.2	185.2	111.1	92.6
20161009	12	24	-65.4	101.9	993	148.2	185.2	111.1	92.6
20161009	18	24.1	-65.3	101.9	992	185.2	185.2	111.1	111.1
20161010	0	24.3	-65.2	92.6	992	185.2	185.2	111.1	111.1
20161010	6	24.8	-65.2	92.6	992	203.7	185.2	111.1	111.1
20161010	12	25.4	-65.2	92.6	992	203.7	185.2	111.1	111.1
20161010	18	26	-65.3	92.6	992	203.7	185.2	111.1	111.1
20161011	0	26.5	-65.5	92.6	992	166.7	166.7	111.1	111.1
20161011	6	26.8	-65.6	92.6	991	166.7	166.7	111.1	111.1
20161011	12	27.1	-65.8	111.1	987	166.7	166.7	111.1	111.1
20161011	18	27.2	-66.2	129.6	980	185.2	166.7	129.6	166.7
20161012	0	27.4	-66.6	138.9	976	185.2	166.7	129.6	166.7
20161012	6	27.6	-66.8	157.4	973	185.2	166.7	129.6	166.7
20161012	12	28	-66.9	175.9	969	222.2	222.2	129.6	166.7
20161012	18	28.7	-66.8	194.5	962	259.3	240.8	166.7	222.2
20161013	0	29.6	-66.5	213.0	954	277.8	277.8	166.7	277.8
20161013	6	30.6	-66.2	222.2	950	277.8	277.8	166.7	277.8
20161013	12	31.6	-65.3	203.7	956	277.8	333.4	166.7	277.8
20161013	15	32.3	-64.7	194.5	959	277.8	333.4	166.7	277.8
20161013	18	33	-63.9	175.9	962	277.8	333.4	166.7	277.8

20161014	0	34.9	-62.1	157.4 138.9	967 972	333.4	333.4 333.4	222.2 222.2	333.4
	12		-60.5			333.4			333.4
20161014	12	35.6	-58.9	129.6	975	444.5	444.5	333.4	444.5
20161014	18	36.4	-56.5	120.4	977	444.5	444.5	333.4	444.5
20161015	0	37.2	-54.2	120.4	974	444.5	444.5	333.4	500.0
20161015	6	38	-52.6	138.9	965	444.5	500.0	444.5	500.0
20161015	12	38.7	-51.1	138.9	960	666.7	611.2	444.5	666.7
20161015	18	39	-49.8	138.9	961	666.7	555.6	555.6	666.7
20161016	0	39.3	-48.7	138.9	961	666.7	611.2	555.6	777.8
20161016	6	39.1	-48	129.6	962	666.7	611.2	555.6	777.8
20161016	12	38.9	-47.2	129.6	963	666.7	611.2	555.6	666.7
20161016	18	39.4	-46.4	120.4	964	666.7	611.2	611.2	666.7
20161017	0	40.1	-45.8	120.4	965	666.7	555.6	611.2	666.7
20161017	6	40.6	-45.5	120.4	965	666.7	555.6	611.2	555.6
20161017	12	40.9	-45.1	120.4	966	666.7	555.6	611.2	555.6
20161017	18	41.8	-43.6	120.4	966	555.6	555.6	611.2	555.6
20161018	0	43.5	-41.9	111.1	966	500.0	555.6	611.2	333.4
20161018	6	45.6	-39.7	101.9	966	500.0	555.6	555.6	277.8
20161018	12	49	-38.5	101.9	966	500.0	555.6	555.6	277.8
20161018	18	53	-38.5	92.6	967	500.0	555.6	555.6	277.8
20161019	0	55.1	-38	92.6	968	500.0	555.6	555.6	277.8
20161019	6	57	-37	92.6	969	500.0	555.6	555.6	277.8
20161019	12	59	-36.5	92.6	969	500.0	555.6	555.6	277.8
					Gert				
				Maximum	Minimum	63km/h	63km/h	63km/h	63km/h
Date	Hour	Latitude	Longitude	Sustained Wind	Pressure	Wind NE	Wind SE	Wind SW	Wind NW
				Speed (km/h)	(mbar)	Radii (km)	Radii (km)	Radii (km)	Radii (km)

168

20170812	0	22.4	-66.8	46.3	1013	0.0	0.0	0.0	0.0
20170812	6	22.7	-67.8	46.3	1013	0.0	0.0	0.0	0.0
20170812	12	23.2	-68.7	46.3	1013	0.0	0.0	0.0	0.0
20170812	18	24	-69.4	55.6	1013	0.0	0.0	0.0	0.0
20170813	0	24.9	-70	64.8	1012	129.6	0.0	0.0	0.0
20170813	6	25.8	-70.6	64.8	1012	129.6	0.0	0.0	0.0
20170813	12	26.8	-71.2	64.8	1012	129.6	0.0	0.0	0.0
20170813	18	27.7	-71.6	64.8	1012	129.6	0.0	0.0	0.0
20170814	0	28.5	-71.9	74.1	1009	148.2	111.1	0.0	0.0
20170814	6	29.2	-72.1	83.3	1006	148.2	111.1	0.0	0.0
20170814	12	29.7	-72.2	92.6	1002	148.2	111.1	0.0	0.0
20170814	18	30.2	-72.3	101.9	996	166.7	148.2	55.6	92.6
20170815	0	30.8	-72.3	111.1	992	166.7	148.2	74.1	92.6
20170815	6	31.5	-72.3	120.4	986	166.7	148.2	92.6	92.6
20170815	12	32.3	-72.1	129.6	982	166.7	166.7	111.1	92.6
20170815	18	33.2	-71.8	129.6	980	185.2	185.2	111.1	92.6
20170816	0	34.2	-71	138.9	976	185.2	185.2	111.1	92.6
20170816	6	35.4	-69.5	148.2	973	203.7	203.7	129.6	74.1
20170816	12	36.8	-67.1	157.4	969	222.2	222.2	129.6	74.1
20170816	18	38.2	-64.1	175.9	962	259.3	259.3	148.2	92.6
20170817	0	39.4	-60.4	166.7	964	296.3	259.3	166.7	92.6
20170817	6	40.7	-56.2	148.2	968	333.4	277.8	185.2	92.6
20170817	12	42.2	-52	111.1	981	370.4	314.8	185.2	92.6
20170817	18	44	-48	92.6	988	407.4	407.4	185.2	37.0
20170818	0	45.9	-44.3	74.1	991	444.5	407.4	185.2	0.0
20170818	6	47.7	-40.5	64.8	994	500.0	500.0	0.0	0.0
20170818	12	48.8	-37.8	64.8	996	555.6	555.6	0.0	0.0

۰		À
c	7	١
Š	Ċ	j

20170818	18	50.5	-36.5	64.8	998	611.2	0.0	0.0	0.0
					Irma				
				Maximum	Minimum	63km/h	63km/h	63km/h	63km/h
Date	Hour	Latitude	Longitude	Sustained Wind	Pressure	Wind NE	Wind SE	Wind SW	Wind NW
				Speed (km/h)	(mbar)	Radii (km)	Radii (km)	Radii (km)	Radii (km)
20170830	0	16.1	-26.9	55.6	1008	0.0	0.0	0.0	0.0
20170830	6	16.2	-28.3	64.8	1007	55.6	0.0	0.0	0.0
20170830	12	16.3	-29.7	83.3	1006	55.6	0.0	0.0	55.6
20170830	18	16.3	-30.8	92.6	1004	55.6	55.6	0.0	55.6
20170831	0	16.3	-31.7	101.9	999	74.1	74.1	55.6	74.1
20170831	6	16.4	-32.5	120.4	994	92.6	74.1	55.6	92.6
20170831	12	16.7	-33.4	148.2	983	111.1	92.6	74.1	111.1
20170831	18	17.1	-34.2	175.9	970	129.6	92.6	74.1	111.1
20170901	0	17.5	-35.1	185.2	967	129.6	111.1	74.1	111.1
20170901	6	17.9	-36.1	185.2	967	148.2	111.1	74.1	111.1
20170901	12	18.4	-37.3	185.2	967	148.2	111.1	74.1	111.1
20170901	18	18.8	-38.5	185.2	967	166.7	111.1	74.1	111.1
20170902	0	19.1	-39.7	185.2	967	166.7	111.1	74.1	111.1
20170902	6	19.1	-41.1	185.2	967	166.7	111.1	74.1	111.1
20170902	12	18.9	-42.6	175.9	973	166.7	111.1	74.1	111.1
20170902	18	18.7	-44.1	175.9	973	166.7	111.1	74.1	129.6
20170903	0	18.5	-45.5	175.9	973	185.2	111.1	74.1	148.2
20170903	6	18.2	-46.7	175.9	973	203.7	111.1	74.1	166.7
20170903	12	17.9	-47.9	185.2	969	222.2	129.6	92.6	166.7
20170903	18	17.6	-49.2	185.2	965	222.2	148.2	92.6	185.2
20170904	0	17.3	-50.4	185.2	959	222.2	148.2	92.6	185.2
20170904	6	17	-51.5	194.5	952	222.2	148.2	92.6	185.2

20170904	18	16.7	-53.9	213.0	944	222.2	185.2	129.6	203.7
20170905	0	16.6	-55.1	231.5	943	222.2	185.2	148.2	203.7
20170905	6	16.6	-56.4	250.0	933	240.8	185.2	148.2	222.2
20170905	12	16.7	-57.8	277.8	929	259.3	203.7	148.2	240.8
20170905	18	16.9	-59.2	287.1	926	277.8	203.7	166.7	259.3
20170906	0	17.3	-60.6	287.1	915	277.8	203.7	166.7	277.8
20170906	6	17.7	-61.9	287.1	914	277.8	203.7	166.7	277.8
20170906	12	18.1	-63.3	287.1	915	296.3	203.7	166.7	277.8
20170906	18	18.6	-64.7	277.8	916	296.3	222.2	166.7	277.8
20170907	0	19.2	-66.2	277.8	916	296.3	222.2	166.7	277.8
20170907	6	19.7	-67.6	268.5	920	296.3	222.2	166.7	277.8
20170907	12	20.2	-69	268.5	921	296.3	222.2	166.7	277.8
20170907	18	20.7	-70.4	268.5	922	296.3	222.2	166.7	277.8
20170908	0	21.1	-71.8	259.3	919	296.3	222.2	166.7	277.8
20170908	5	21.5	-73	250.0	924	296.3	222.2	166.7	277.8
20170908	6	21.5	-73.2	250.0	925	296.3	222.2	166.7	277.8
20170908	12	21.8	-74.7	250.0	927	296.3	222.2	185.2	277.8
20170908	18	22	-76	259.3	925	296.3	222.2	185.2	277.8
20170909	0	22.1	-77.2	268.5	924	296.3	240.8	203.7	296.3
20170909	3	22.3	-77.9	268.5	924	296.3	259.3	203.7	296.3
20170909	6	22.4	-78.3	240.8	930	296.3	296.3	222.2	314.8
20170909	12	22.7	-79.3	203.7	941	296.3	296.3	222.2	314.8
20170909	18	23.1	-80.2	175.9	938	333.4	296.3	222.2	333.4
20170910	0	23.4	-80.9	185.2	932	388.9	314.8	222.2	333.4
20170910	6	23.7	-81.3	213.0	930	444.5	314.8	259.3	351.9
20170910	12	24.5	-81.5	213.0	931	500.0	333.4	259.3	388.9

203.7

945

222.2

166.7

111.1

185.2

20170904

12

16.8

-52.6

\vdash	_
	١
	J

20170910	13	24.7	-81.5	213.0	931	500.0	333.4	259.3	388.9
-									
20170910	18	25.6	-81.7	185.2	936	555.6	351.9	259.3	407.4
20170911	0	26.8	-81.7	148.2	942	666.7	370.4	277.8	444.5
20170911	6	28.2	-82.2	120.4	961	666.7	388.9	277.8	444.5
20170911	12	29.6	-82.7	92.6	970	666.7	426.0	277.8	444.5
20170911	18	30.9	-83.5	83.3	980	666.7	463.0	277.8	444.5
20170912	0	31.9	-84.4	64.8	986	666.7	500.0	0.0	0.0
20170912	6	32.9	-85.6	46.3	997	0.0	0.0	0.0	0.0
20170912	12	33.8	-86.9	37.0	1000	0.0	0.0	0.0	0.0
20170912	18	34.8	-88.1	27.8	1003	0.0	0.0	0.0	0.0
20170913	0	35.6	-88.9	27.8	1004	0.0	0.0	0.0	0.0
20170913	6	36.2	-89.5	27.8	1004	0.0	0.0	0.0	0.0
20170913	12	36.8	-90.1	27.8	1005	0.0	0.0	0.0	0.0
	Jose								

	1	1			0030	T			
				Maximum	Minimum	63km/h	63km/h	63km/h	63km/h
Date	Hour	Latitude	Longitude	Sustained Wind	Pressure	Wind NE	Wind SE	Wind SW	Wind NW
				Speed (km/h)	(mbar)	Radii (km)	Radii (km)	Radii (km)	Radii (km)
20170904	6	9.3	-33.5	37.0	1010	0.0	0.0	0.0	0.0
20170904	12	10	-34.9	46.3	1010	0.0	0.0	0.0	0.0
20170904	18	10.6	-36	46.3	1010	0.0	0.0	0.0	0.0
20170905	0	11.1	-37	46.3	1009	0.0	0.0	0.0	0.0
20170905	6	11.6	-37.9	55.6	1008	0.0	0.0	0.0	0.0
20170905	12	12	-38.8	64.8	1008	0.0	74.1	0.0	0.0
20170905	18	12.2	-40	74.1	1006	92.6	74.1	0.0	0.0
20170906	0	12.2	-41.3	83.3	1004	92.6	74.1	0.0	55.6
20170906	6	12.5	-42.6	92.6	1001	92.6	74.1	0.0	74.1
20170906	12	13.1	-43.9	101.9	998	92.6	74.1	74.1	92.6

20170906	18	13.7	-45.2	120.4	995	111.1	74.1	74.1	111.1
20170907	0	14.1	-46.7	129.6	993	129.6	92.6	74.1	129.6
20170907	6	14.4	-48.3	148.2	986	148.2	111.1	74.1	148.2
20170907	12	14.7	-49.9	166.7	977	166.7	111.1	74.1	166.7
20170907	18	15.1	-51.5	185.2	969	185.2	129.6	74.1	166.7
20170908	0	15.5	-53.2	194.5	964	185.2	129.6	74.1	185.2
20170908	6	15.9	-54.9	213.0	955	203.7	148.2	92.6	203.7
20170908	12	16.1	-56.4	240.8	940	222.2	166.7	92.6	203.7
20170908	18	16.4	-57.8	250.0	939	222.2	166.7	92.6	203.7
20170909	0	16.7	-58.9	250.0	938	240.8	185.2	92.6	222.2
20170909	6	17.2	-59.9	240.8	940	240.8	185.2	92.6	222.2
20170909	12	17.9	-60.8	231.5	941	240.8	203.7	92.6	222.2
20170909	18	18.6	-61.8	222.2	942	240.8	203.7	111.1	222.2
20170910	0	19.4	-62.9	213.0	943	240.8	203.7	111.1	222.2
20170910	6	20.3	-64	213.0	945	240.8	203.7	111.1	222.2
20170910	12	21.2	-65.3	213.0	948	240.8	203.7	111.1	203.7
20170910	18	22.2	-66.5	194.5	956	240.8	203.7	111.1	203.7
20170911	0	23.3	-67.6	185.2	962	240.8	203.7	111.1	203.7
20170911	6	24.3	-68.6	166.7	968	240.8	203.7	129.6	203.7
20170911	12	25.4	-69.4	157.4	972	240.8	203.7	129.6	185.2
20170911	18	26.5	-69.5	148.2	974	222.2	203.7	129.6	185.2
20170912	0	27.2	-69.4	138.9	977	222.2	203.7	129.6	166.7
20170912	6	27.6	-69.1	129.6	979	222.2	203.7	129.6	166.7
20170912	12	27.7	-68.3	129.6	979	222.2	185.2	129.6	166.7
20170912	18	27.4	-67.4	129.6	980	203.7	185.2	129.6	148.2
20170913	0	26.8	-66.7	129.6	981	203.7	185.2	129.6	148.2
20170913	6	26.3	-66.2	129.6	981	203.7	185.2	129.6	148.2

20170913	12	25.8	-65.8	129.6	981	203.7	185.2	129.6	148.2
20170913	18	25.4	-65.6	129.6	981	203.7	185.2	129.6	129.6
20170914	0	25.1	-65.7	129.6	981	203.7	185.2	129.6	129.6
20170914	6	24.9	-65.9	129.6	981	203.7	185.2	129.6	129.6
20170914	12	24.8	-66.3	120.4	983	203.7	185.2	129.6	129.6
20170914	18	25	-66.9	120.4	985	203.7	203.7	129.6	129.6
20170915	0	25.4	-67.6	111.1	988	203.7	203.7	129.6	148.2
20170915	6	25.8	-68.2	111.1	988	222.2	203.7	129.6	148.2
20170915	12	26.3	-69	111.1	986	222.2	222.2	129.6	148.2
20170915	18	26.8	-69.9	120.4	983	222.2	222.2	129.6	166.7
20170916	0	27.2	-70.7	120.4	983	240.8	222.2	148.2	166.7
20170916	6	27.7	-71.4	120.4	983	240.8	240.8	148.2	166.7
20170916	12	28.2	-71.8	120.4	980	259.3	259.3	148.2	185.2
20170916	18	28.6	-72	120.4	973	277.8	259.3	166.7	185.2
20170917	0	29.1	-72	129.6	971	277.8	277.8	166.7	203.7
20170917	6	29.8	-72	138.9	969	296.3	277.8	166.7	222.2
20170917	12	30.5	-71.9	148.2	967	314.8	296.3	185.2	222.2
20170917	18	31.2	-71.8	148.2	967	333.4	314.8	185.2	240.8
20170918	0	31.9	-71.6	148.2	972	333.4	314.8	203.7	259.3
20170918	6	32.7	-71.4	138.9	974	351.9	333.4	222.2	259.3
20170918	12	33.5	-71.2	129.6	976	370.4	333.4	222.2	277.8
20170918	18	34.2	-71.2	120.4	975	370.4	351.9	240.8	277.8
20170919	0	34.9	-71.4	120.4	972	388.9	351.9	259.3	296.3
20170919	6	35.6	-71.6	120.4	971	388.9	351.9	259.3	314.8
20170919	12	36.3	-71.7	111.1	973	388.9	351.9	277.8	314.8
20170919	18	37	-71.5	111.1	973	388.9	370.4	296.3	314.8
20170920	0	37.6	-71.2	111.1	973	388.9	370.4	296.3	333.4

_	_
_	
•	_
	\sim

	I					-	<u> </u>		
20170920	6	38.1	-70.8	111.1	975	388.9	351.9	314.8	333.4
20170920	12	38.7	-70.2	111.1	976	370.4	351.9	314.8	333.4
20170920	18	39.2	-69.4	111.1	976	370.4	351.9	333.4	333.4
20170921	0	39.4	-68.5	101.9	979	351.9	333.4	333.4	333.4
20170921	6	39.7	-68.1	101.9	982	333.4	314.8	333.4	333.4
20170921	12	39.7	-68	101.9	984	314.8	314.8	333.4	314.8
20170921	18	39.5	-68	92.6	984	296.3	277.8	333.4	314.8
20170922	0	39.5	-68.2	83.3	986	277.8	259.3	314.8	296.3
20170922	6	39.6	-68.6	83.3	989	277.8	240.8	296.3	277.8
20170922	12	39.7	-69	74.1	992	259.3	222.2	259.3	259.3
20170922	18	39.7	-69.1	74.1	996	0.0	0.0	240.8	240.8
20170923	0	39.7	-69.3	64.8	999	0.0	0.0	203.7	222.2
20170923	6	39.5	-69.6	64.8	1002	0.0	0.0	185.2	203.7
20170923	12	39.1	-69.7	55.6	1004	0.0	0.0	0.0	0.0
20170923	18	38.7	-69.1	55.6	1007	0.0	0.0	0.0	0.0
20170924	0	38.7	-68.7	46.3	1009	0.0	0.0	0.0	0.0
20170924	6	38.9	-68.4	46.3	1010	0.0	0.0	0.0	0.0
20170924	12	38.9	-68	37.0	1011	0.0	0.0	0.0	0.0
20170924	18	38.7	-68.2	27.8	1011	0.0	0.0	0.0	0.0
20170925	0	38.7	-68.7	27.8	1012	0.0	0.0	0.0	0.0
20170925	6	38.7	-69.2	27.8	1013	0.0	0.0	0.0	0.0
Lee									
				Maximum	Minimum	63km/h	63km/h	63km/h	63km/h
Date	Hour	Latitude	Longitude	Sustained Wind	Pressure	Wind NE	Wind SE	Wind SW	Wind NW
				Speed (km/h)	(mbar)	Radii (km)	Radii (km)	Radii (km)	Radii (km)
20170914	18	10.4	-23.1	46.3	1011	0.0	0.0	0.0	0.0
20170915	0	10.6	-24.7	55.6	1010	0.0	0.0	0.0	0.0

20170915	6	11.1	-26.2	55.6	1008	0.0	0.0	0.0	0.0
20170915	12	11.7	-27.6	55.6	1008	0.0	0.0	0.0	0.0
20170915	18	12.4	-29	55.6	1009	0.0	0.0	0.0	0.0
20170916	0	12.6	-30.5	55.6	1009	0.0	0.0	0.0	0.0
20170916	6	12.6	-31.9	55.6	1008	0.0	0.0	0.0	0.0
20170916	12	12.5	-33.1	64.8	1007	111.1	111.1	0.0	111.1
20170916	18	12.6	-33.9	64.8	1007	111.1	111.1	0.0	111.1
20170917	0	12.7	-34.6	64.8	1007	0.0	74.1	92.6	0.0
20170917	6	12.8	-35.4	64.8	1007	0.0	74.1	92.6	0.0
20170917	12	12.9	-36.2	55.6	1008	0.0	0.0	0.0	0.0
20170917	18	13.1	-37	55.6	1008	0.0	0.0	0.0	0.0
20170918	0	13.4	-37.9	55.6	1008	0.0	0.0	0.0	0.0
20170918	6	13.8	-39	55.6	1008	0.0	0.0	0.0	0.0
20170918	12	14.2	-40.2	55.6	1008	0.0	0.0	0.0	0.0
20170918	18	14.5	-41.5	55.6	1008	0.0	0.0	0.0	0.0
20170919	0	14.9	-42.6	46.3	1009	0.0	0.0	0.0	0.0
20170919	6	15.5	-43.3	46.3	1009	0.0	0.0	0.0	0.0
20170919	12	16.1	-43.8	55.6	1008	0.0	0.0	0.0	0.0
20170919	18	16.8	-44.4	64.8	1007	74.1	0.0	0.0	0.0
20170920	0	17.6	-45	74.1	1006	129.6	129.6	0.0	0.0
20170920	6	18.3	-45.2	64.8	1007	129.6	0.0	0.0	0.0
20170920	12	20.4	-44.1	55.6	1009	0.0	0.0	0.0	0.0
20170920	18	22	-43.9	55.6	1011	0.0	0.0	0.0	0.0
20170921	0	23.8	-43.9	46.3	1015	0.0	0.0	0.0	0.0
20170921	6	26.5	-45.3	46.3	1016	0.0	0.0	0.0	0.0
20170921	12	27.8	-46.5	46.3	1016	0.0	0.0	0.0	0.0
20170921	18	28.8	-47.5	46.3	1016	0.0	0.0	0.0	0.0

176

20170922	0	29.3	-48.3	46.3	1016	0.0	0.0	0.0	0.0
20170922	6	29.6	-48.7	46.3	1016	0.0	0.0	0.0	0.0
20170922	12	30	-48.9	46.3	1014	0.0	0.0	0.0	0.0
20170922	18	30.5	-49.1	55.6	1012	0.0	0.0	0.0	0.0
20170923	0	31.1	-49.2	64.8	1010	37.0	37.0	37.0	37.0
20170923	6	31.5	-49.3	64.8	1009	37.0	37.0	37.0	37.0
20170923	12	31.8	-49.4	74.1	1006	37.0	37.0	37.0	37.0
20170923	18	32	-49.8	83.3	1003	55.6	55.6	55.6	55.6
20170924	0	31.9	-50.1	92.6	1000	55.6	55.6	55.6	55.6
20170924	6	31.7	-50.2	120.4	990	55.6	55.6	55.6	55.6
20170924	12	31.5	-50.1	138.9	983	55.6	55.6	55.6	55.6
20170924	18	31.3	-49.8	148.2	980	55.6	55.6	55.6	55.6
20170925	0	31.2	-49.6	157.4	976	55.6	55.6	55.6	55.6
20170925	6	31	-49.5	148.2	978	55.6	55.6	55.6	55.6
20170925	12	30.8	-49.7	148.2	980	55.6	55.6	55.6	55.6
20170925	18	30.6	-50.2	138.9	984	55.6	55.6	55.6	55.6
20170926	0	30.3	-51	148.2	982	74.1	74.1	74.1	74.1
20170926	6	30.1	-52	157.4	979	74.1	74.1	74.1	74.1
20170926	12	29.9	-53.2	166.7	976	74.1	74.1	74.1	74.1
20170926	18	29.9	-54.2	175.9	972	92.6	92.6	74.1	74.1
20170927	0	29.9	-55.1	175.9	970	92.6	92.6	74.1	74.1
20170927	6	30.1	-56	175.9	967	129.6	129.6	92.6	111.1
20170927	12	30.3	-56.6	185.2	963	148.2	111.1	111.1	129.6
20170927	18	30.8	-57	185.2	962	148.2	111.1	111.1	129.6
20170928	0	31.4	-57.2	175.9	965	148.2	111.1	111.1	129.6
20170928	6	32.1	-57.3	166.7	969	148.2	148.2	129.6	129.6
20170928	12	33	-57.2	157.4	973	148.2	148.2	129.6	129.6

1	
\sim	
~ĩ	
7	

20170928	18	34.3	-56.6	148.2	977	148.2	148.2	129.6	129.6
20170929	0	35.7	-55.5	138.9	981	148.2	185.2	148.2	111.1
20170929	6	37.3	-53.8	129.6	983	185.2	222.2	203.7	111.1
20170929	12	39	-51.2	120.4	985	185.2	222.2	203.7	111.1
20170929	18	41	-48.2	101.9	987	185.2	222.2	203.7	111.1
20170930	0	43.2	-44.5	92.6	990	185.2	222.2	203.7	111.1
20170930	6	45.8	-38.9	83.3	993	166.7	240.8	240.8	0.0

TA /	
N	arıa

				Maximum	Minimum	63km/h	63km/h	63km/h	63km/h
Date	Hour	Latitude	Longitude	Sustained Wind	Pressure	Wind NE	Wind SE	Wind SW	Wind NW
				Speed (km/h)	(mbar)	Radii (km)	Radii (km)	Radii (km)	Radii (km)
20170916	12	12.2	-49.7	55.6	1006	0.0	0.0	0.0	0.0
20170916	18	12.2	-51.7	74.1	1004	74.1	0.0	0.0	74.1
20170917	0	12.4	-53.1	83.3	1002	74.1	55.6	0.0	74.1
20170917	6	12.8	-54.4	101.9	994	92.6	74.1	0.0	92.6
20170917	12	13.3	-55.7	111.1	990	111.1	74.1	55.6	92.6
20170917	18	13.6	-57	120.4	986	129.6	111.1	74.1	111.1
20170918	0	14	-58	138.9	979	166.7	111.1	74.1	129.6
20170918	6	14.3	-59	148.2	977	166.7	111.1	74.1	129.6
20170918	12	14.5	-59.7	185.2	967	203.7	166.7	129.6	166.7
20170918	18	14.9	-60.4	203.7	956	203.7	166.7	148.2	166.7
20170919	0	15.3	-61.1	268.5	924	203.7	203.7	148.2	166.7
20170919	6	15.7	-61.9	250.0	940	203.7	203.7	148.2	185.2
20170919	12	16.1	-62.7	259.3	931	222.2	203.7	148.2	185.2
20170919	18	16.6	-63.5	268.5	920	222.2	203.7	148.2	185.2
20170920	0	17	-64.3	277.8	909	240.8	203.7	185.2	203.7
20170920	3	17.3	-64.7	277.8	908	240.8	203.7	185.2	203.7

20170920	6	17.6	-65.1	259.3	913	240.8	203.7	185.2	203.7
20170920	12	18.2	-66.2	213.0	935	240.8	203.7	185.2	203.7
20170920	18	18.6	-67	175.9	959	240.8	203.7	185.2	203.7
20170921	0	19	-67.6	175.9	958	240.8	203.7	203.7	203.7
20170921	6	19.4	-68.2	185.2	959	240.8	203.7	203.7	203.7
20170921	12	19.9	-68.8	185.2	959	240.8	203.7	203.7	203.7
20170921	18	20.5	-69.5	194.5	960	259.3	240.8	203.7	203.7
20170922	0	20.8	-70	203.7	953	259.3	222.2	185.2	222.2
20170922	6	21.2	-70.5	203.7	959	259.3	222.2	185.2	240.8
20170922	12	21.9	-70.9	203.7	958	259.3	222.2	185.2	240.8
20170922	18	22.8	-71.2	203.7	959	259.3	240.8	185.2	222.2
20170923	0	23.7	-71.6	194.5	953	296.3	240.8	185.2	222.2
20170923	6	24.4	-71.9	185.2	952	314.8	314.8	185.2	222.2
20170923	12	25.1	-72.1	185.2	952	314.8	314.8	185.2	277.8
20170923	18	25.9	-72.3	185.2	952	388.9	370.4	185.2	277.8
20170924	0	26.6	-72.4	185.2	945	388.9	370.4	185.2	277.8
20170924	6	27.5	-72.6	175.9	942	388.9	370.4	222.2	296.3
20170924	12	28.4	-72.8	175.9	947	388.9	370.4	222.2	296.3
20170924	18	29.1	-72.9	166.7	943	370.4	370.4	259.3	296.3
20170925	0	29.7	-72.9	157.4	947	370.4	370.4	259.3	296.3
20170925	6	30.3	-72.9	138.9	954	370.4	370.4	296.3	314.8
20170925	12	30.8	-73	129.6	961	370.4	370.4	296.3	296.3
20170925	18	31.4	-73.1	129.6	966	333.4	333.4	296.3	296.3
20170926	0	32	-73.1	129.6	966	333.4	333.4	296.3	296.3
20170926	6	32.6	-73.1	120.4	970	370.4	388.9	296.3	296.3
20170926	12	33.3	-73.1	120.4	970	370.4	388.9	296.3	296.3
20170926	18	33.9	-73.1	120.4	975	370.4	370.4	296.3	296.3

_	J
	-
	_
~	_

				Speed (km/h)	(mbar)	Radii (km)	Radii (km)	Radii (km)	Radii (km)
Date	Hour	Latitude	Longitude	Sustained Wind	Pressure	Wind NE	Wind SE	Wind SW	Wind NW
				Maximum	Minimum	63km/h	63km/h	63km/h	63km/h
20171002	12	48	-17	55.6	1016 Ophelia	0.0	0.0	0.0	0.0
20171002	12	48	-22	74.1	1012	0.0	0.0	370.4	277.8
20171002	0	47.5	-26.5	74.1	1005	0.0	0.0	370.4	277.8
20171001	18	46.5	-31	83.3	1003	203.7	370.4	370.4	277.8
20171001	12	44.9	-35.5	83.3	999	203.7	370.4	370.4	277.8
20171001	6	43.4	-39.4	83.3	996	203.7	370.4	370.4	277.8
20171001	0	42.2	-42.6	83.3	994	203.7	370.4	370.4	277.8
20170930	18	41.2	-45.6	83.3	991	203.7	370.4	370.4	277.8
20170930	12	40	-48.8	92.6	988	203.7	370.4	370.4	333.4
20170930	6	39.1	-52.2	92.6	988	203.7	370.4	370.4	333.4
20170930	0	38.1	-55.6	92.6	988	185.2	407.4	407.4	333.4
20170929	18	37.4	-59	92.6	988	185.2	407.4	407.4	333.4
20170929	12	37	-62	92.6	988	185.2	388.9	407.4	333.4
20170929	6	37	-64.6	92.6	987	185.2	388.9	407.4	333.4
20170929	0	36.9	-66.8	101.9	985	333.4	370.4	296.3	277.8
20170928	18	36.8	-68.6	101.9	985	333.4	388.9	296.3	277.8
20170928	12	36.8	-70	111.1	982	333.4	388.9	296.3	277.8
20170928	6	36.7	-71.3	111.1	982	333.4	388.9	296.3	277.8
20170928	0	36.6	-72.2	120.4	979	370.4	370.4	296.3	277.8
20170927	18	36	-72.6	120.4	979	370.4	370.4	296.3	277.8
20170927	12	35.4	-72.8	120.4	977	370.4	370.4	296.3	277.8
20170927	6	34.9	-72.9	120.4	976	370.4	370.4	296.3	277.8
20170927	0	34.4	-73	120.4	975	370.4	370.4	296.3	296.3

180	

20171006	12	31.8	-39.5	37.0	1013	0.0	0.0	0.0	0.0
20171006	18	32.3	-38.6	37.0	1012	0.0	0.0	0.0	0.0
20171007	0	32.9	-37.3	46.3	1011	0.0	0.0	0.0	0.0
20171007	6	32.7	-38.5	55.6	1010	0.0	0.0	0.0	0.0
20171007	12	32.3	-39.5	55.6	1010	0.0	0.0	0.0	0.0
20171007	18	31.5	-39.5	55.6	1010	0.0	0.0	0.0	0.0
20171008	0	31.3	-39.5	55.6	1010	0.0	0.0	0.0	0.0
20171008	6	31	-39.6	64.8	1010	74.1	0.0	0.0	74.1
20171008	12	30.6	-39.7	64.8	1009	74.1	0.0	0.0	74.1
20171008	18	30.4	-40.1	64.8	1009	92.6	0.0	0.0	74.1
20171009	0	30.5	-40.1	64.8	1008	92.6	0.0	0.0	74.1
20171009	6	30.9	-40	64.8	1008	111.1	0.0	0.0	74.1
20171009	12	31.3	-40	64.8	1008	111.1	0.0	0.0	74.1
20171009	18	31.7	-39.6	74.1	1005	111.1	74.1	0.0	92.6
20171010	0	32	-39.1	74.1	1005	111.1	92.6	55.6	111.1
20171010	6	31.9	-38.8	83.3	1003	111.1	92.6	74.1	111.1
20171010	12	31.6	-38.5	83.3	1002	111.1	111.1	111.1	111.1
20171010	18	31.3	-38.2	83.3	1002	111.1	111.1	111.1	111.1
20171011	0	30.9	-37.8	92.6	1000	111.1	111.1	111.1	111.1
20171011	6	30.4	-37.2	101.9	998	111.1	111.1	111.1	111.1
20171011	12	30	-36.7	111.1	994	111.1	111.1	111.1	111.1
20171011	18	29.8	-36.2	120.4	991	111.1	111.1	111.1	111.1
20171012	0	29.9	-35.8	129.6	986	111.1	111.1	111.1	111.1
20171012	6	30.2	-35.7	138.9	982	111.1	111.1	111.1	111.1
20171012	12	30.4	-35.7	148.2	975	111.1	111.1	111.1	111.1
20171012	18	30.5	-35.6	157.4	971	129.6	129.6	129.6	129.6
20171013	0	30.5	-35.1	166.7	967	129.6	129.6	129.6	129.6

20171013	6	30.9	-34.4	166.7	966	129.6	129.6	129.6	129.6
20171013	12	31.4	-33.4	148.2	974	148.2	148.2	129.6	129.6
20171013	18	32	-32.5	148.2	973	148.2	148.2	148.2	129.6
20171014	0	32.6	-31.5	157.4	970	148.2	148.2	148.2	129.6
20171014	6	33.4	-29.7	175.9	963	148.2	166.7	166.7	129.6
20171014	12	34.2	-27.7	185.2	959	166.7	185.2	185.2	148.2
20171014	18	35.3	-25.2	185.2	959	166.7	203.7	203.7	166.7
20171015	0	36.4	-22.6	175.9	959	185.2	240.8	240.8	185.2
20171015	6	37.9	-19.8	166.7	959	203.7	277.8	277.8	203.7
20171015	12	39.9	-17	157.4	959	222.2	333.4	333.4	259.3
20171015	18	43.1	-14.3	148.2	959	240.8	407.4	407.4	333.4
20171016	0	47.6	-13.4	138.9	958	259.3	444.5	444.5	388.9
20171016	6	50	-12.1	129.6	957	277.8	444.5	444.5	388.9
20171016	11	51.9	-10.4	129.6	957	277.8	444.5	444.5	388.9
20171016	12	52.3	-10	120.4	959	314.8	444.5	444.5	388.9
20171016	18	55.3	-8.3	111.1	969	370.4	444.5	444.5	388.9
20171017	0	57.3	-6.1	92.6	977	444.5	666.7	444.5	388.9
20171017	6	58.7	-2.9	83.3	987	444.5	666.7	444.5	388.9
20171017	12	59.3	1.5	74.1	994	222.2	500.0	444.5	277.8
20171017	18	60.1	5.3	74.1	997	0.0	388.9	388.9	222.2

5.7. References

- Ardhuin, F. et al. (2011) 'Ocean wave sources of seismic noise', Journal of Geophysical Research. Wiley-Blackwell, 116(C9), p. C09004. doi: 10.1029/2011JC006952.
- Bromirski, P. D. and Kossin, J. P. (2008) 'Increasing hurricane wave power along the U.S. Atlantic and Gulf coasts', *Journal of Geophysical Research: Oceans*, 113(7), pp. 1–10. doi: 10.1029/2007JC004706.
- Capon, J. (1970) 'Applications of detection and estimation theory to large array seismology', *Proceedings of the IEEE*, 58(5), pp. 760–770. doi: 10.1109/PROC.1970.7730.
- Dziewonski, A. M. and Anderson, D. L. (1981) 'Preliminary reference Earth model',

 Physics of the Earth and Planetary Interiors, 25(4), pp. 297–356. doi: 10.1016/0031-9201(81)90046-7.
- Ebeling, C. W. and Stein, S. (2011) 'Seismological identification and characterization of a large hurricane', *Bulletin of the Seismological Society of America*, 101(1), pp. 399–403. doi: 10.1785/0120100175.
- Farra, V. *et al.* (2016) 'Ray-theoretical modeling of secondary microseism *P* waves', *Geophysical Journal International*. Oxford University Press, 206(3), pp. 1730–1739.

 doi: 10.1093/gji/ggw242.
- Gualtieri, L. *et al.* (2018) 'The persistent signature of tropical cyclones in ambient seismic noise', *Earth and Planetary Science Letters*. Elsevier B.V., 484, pp. 287–294. doi: 10.1016/j.epsl.2017.12.026.
- Hasselmann, K. (1963) 'A statistical analysis of the generation of microseisms', *Rev. of Geophys.*, 1(2), pp. 177–210.

- Kennett, B. L. N. and Engdahl, E. R. (1991) 'Traveltimes for global earthquake location and phase identification', *Geophysical Journal International*. Wiley/Blackwell (10.1111), 105(2), pp. 429–465. doi: 10.1111/j.1365-246X.1991.tb06724.x.
- Kobayashi, N. and Nishida, K. (1998) 'Continuous excitation of planetary free oscillations by atmospheric disturbances', *Nature*, 395(6700), pp. 357–360. doi: 10.1038/26427.
- Longuet-Higgins, M. S. (1950) 'A Theory of the Origin of Microseisms', *Philosophical Transactions of the Royal Society A: Mathematical, Physical and Engineering Sciences*, 243(857), pp. 1–35. doi: 10.1098/rsta.1950.0012.
- Schmidt, R. O. (1979) 'Multiple emiter location and signal parameter estimation', *Proceedings RADC Spectral Estimation Workshop*, 34(3), pp. 276–280. doi: 10.1109/TAP.1986.1143830.
- Tanimoto, T. and Lamontagne, A. (2014) 'Temporal and spatial evolution of an on-land hurricane observed by seismic data', *Geophysical Research Letters*. Wiley-Blackwell, 41(21), pp. 7532–7538. doi: 10.1002/2014GL061934.
- Tanimoto, T. and Um, J. (1999) 'Cause of continuous oscillations of the Earth', *Journal of Geophysical Research: Solid Earth*. Wiley-Blackwell, 104(B12), pp. 28723–28739. doi: 10.1029/1999JB900252.
- Tanimoto, T. and Valovcin, A. (2015) 'Stochastic excitation of seismic waves by a hurricane', *Journal of Geophysical Research : Solid Earth*, 120, pp. 7713–7728. doi: 10.1002/2015JB012177.Received.
- Tanimoto, T. and Valovcin, A. (2016) 'Existence of the threshold pressure for seismic excitation by atmospheric disturbances', *Geophysical Research Letters*. Wiley-Blackwell, 43

Zhang, J., Gerstoft, P. and Bromirski, P. D. (2010) 'Pelagic and coastal sources of P-wave microseisms: Generation under tropical cyclones', *Geophysical Research Letters*, 37(15), pp. 1–6. doi: 10.1029/2010GL044288.